Comenius University in Bratislava
Faculty of Mathematics, Physics and Informatics
Department of Applied Mathematics and Statistics

Convection in multicomponent systems

Dissertation thesis

2019

Mgr. Martin Hurban

Univerzita Komenského v Bratislave
Fakulta matematiky, fyziky a informatiky
Katedra aplikovanej matematiky a štatistiky

Konvekcia v multizložkových systémoch

Dizertačná práca

Študijný program:	Aplikovaná matematika
Študijný odbor:	1114 Aplikovaná matematika
Školiace pracovisko:	Katedra aplikovanej matematiky a štatistiky
Vedúci práce:	doc. Peter Guba, Ph.D.

2019

Mgr. Martin Hurban

Comenius University in Bratislava
Faculty of Mathematics, Physics and Informatics

THESIS ASSIGNMENT

Name and Surname:	Mgr. Martin Hurban
Study programme:	Applied Mathematics (Single degree study, Ph.D. III. deg., full time form)
Field of Study:	Applied Mathematics
Type of Thesis:	Dissertation thesis
Language of Thesis:	English
Secondary language:	Slovak

Title: Convection in multicomponent systems

Annotation: The dissertation is focused on the formulation, asymptotic reduction and analysis of two mathematical models for solidification of multi-component mixtures. The first model describes a two-dimensional steady-state phase transformation in binary (two-component) systems from the laterally-moving rigid boundary. The second model describes a vertical directional solidification in ternary (three-component) systems.

Tutor:	doc. RNDr. Peter Guba, PhD.
Department:	FMFI.KAMŠ - Department of Applied Mathematics and Statistics
Head of department:	prof. RNDr. Marek Fila, DrSc.

Assigned: 29.04.2015

Approved: 29.04.2015 prof. RNDr. Marek Fila, DrSc.
Guarantor of Study Programme

.....
Student

.....
Tutor

Univerzita Komenského v Bratislave
Fakulta matematiky, fyziky a informatiky

ZADANIE ZÁVEREČNEJ PRÁCE

Meno a priezvisko študenta: Mgr. Martin Hurban
Študijný program: aplikovaná matematika (Jednoodborové štúdium, doktorandské III. st., denná forma)
Študijný odbor: aplikovaná matematika
Typ záverečnej práce: dizertačná
Jazyk záverečnej práce: anglický
Sekundárny jazyk: slovenský

Názov: Convection in multicomponent systems
Konvekcia v multizložkových systémoch

Anotácia: Dizertačná práca je zameraná na formuláciu, asymptotickú redukciu a analýzu dvoch matematických modelov pre tuhnutie viaczložkových zmesí. Prvý model popisuje dvojrozmernú stacionárnu fázovú premenu v binárnych (dvojzložkových) systémoch s laterálne posúvanou pevnou hranicou. Druhý model popisuje vertikálne smerové tuhnutie v ternárnych (trojzložkových) systémoch.

Školiteľ: doc. RNDr. Peter Guba, PhD.
Katedra: FMFI.KAMŠ - Katedra aplikovanej matematiky a štatistiky
Vedúci katedry: prof. RNDr. Marek Fila, DrSc.

Spôsob sprístupnenia elektronickej verzie práce:
bez obmedzenia

Dátum zadania: 29.04.2015

Dátum schválenia: 29.04.2015 prof. RNDr. Marek Fila, DrSc.
garant študijného programu

.....
študent

.....
školiteľ

I would like to express my sincere gratitude to my supervisor Doc. Mgr. Peter Guba, PhD. for his kind support, guidance and many inspiring discussions during the work on this dissertation. I would also like to express my sincere gratitude to my wife Mária Hurbanová for ongoing support during my PhD. study.

Abstract

In this thesis, two problems involving solidification have been studied. The first is the solidification of a binary alloy pulled horizontally at a prescribed, constant rate. The second is the solidification of a ternary alloy in the vertical directional solidification setting.

In the binary alloy case, a configuration in which the solid, liquid and two-phase (solid–liquid) regions are separated by the stationary two-dimensional interfaces is considered. The self-similar solutions of the governing boundary-layer equations are obtained, and their parametric dependence analysed asymptotically. The effect of the boundary-layer flow on the physical characteristics is determined. It is found that the horizontal pulling and the resulting flow in the liquid enhance the formation of the two-phase region.

In the ternary alloy case, we identify a steady non-convecting state of during the primary solidification of ternary alloys. A model, which includes the effects thermal and solutal diffusion, segregation effects and finite speed of background solidification is considered. Combinations of various types of boundary conditions have been introduced, namely F–C, C–F and F–F, where C and F refer to the solute concentration and solutal flux fixed at the top or bottom boundary of the system. In the regime of the same Lewis numbers and segregation coefficients of solutes, explicit solution using hypergeometric functions was identified. In the limit of large Lewis and the limit of near constant concentration profile of one solute asymptotic solutions were presented. The behaviour of the concentration profiles was analysed with respect to a static stability scenario, i.e. distribution of a mass within liquid.

Key words: solidification of ternary alloys, solidification of binary alloys, mushy layers, hypergeometric functions, self-similar solutions, static stability, asymptotic approximations

AMS classification: 80A22, 76M45, 35C20

Abstrakt

V tejto práci sú študované dva problémy, ktoré sa týkajú tuhnutia viaczložkových zmesí. Prvým je tuhnutie binárnej zmesi posúvanej horizontálnym smerom predpísanou (konštantnou) rýchlosťou. Druhým je tuhnutie ternárnej zmesi v konfigurácii vertikálneho smerového tuhnutia.

V binárnom prípade je uvažovaná situácia, pri ktorej tuhá, kvapalná aj dvojfázová zóna sú oddelené dvojrozmerným stacionárnym interfejsom. Boli získané podobnostné riešenia rovníc pre problém s hraničnou vrstvou. Následne bola skúmaná ich parametrická závislosť pomocou asymptotických metód. Určili sme vplyv toku v hraničnej vrstve na koncentračnú štruktúru tuhnúceho systému. Ukázalo sa, že horizontálny ťah a následne vznikajúci tok podporujú tvorbu dvojfázovej zóny.

V ternárnom prípade sme študovali primárne tuhnutie ternárneho systému v ustálenom stave bez gravitačnej konvekcie. Sformulovaný model zahŕňa difúziu tepla a prímesí, segregačné efekty a konečnú rýchlosť tuhnutia systému. Pre tento problém sme uvažovali niekoľko rôznych typov okrajových podmienok, predpisujúcich difúzny tok prímesí a koncentrácie prímesí na okrajoch systému. Pre prípad rovnakých Lewisových čísel a segregačných koeficientov prímesí sme získali explicitné riešenia vyjadrené pomocou hypergeometrických funkcií. V limite veľkých Lewisových čísel a konštatného koncentračného profilu jednej z prímesí sme získali rovnomerné asymptotické riešenia. Pomocou získaných koncentračných profilov sme analyzovali statickú stabilitu ternárneho systému.

Kľúčové slová: tuhnutie ternárneho systému, tuhnutie binárneho systému, dendritická zóna, hypergeometrické funkcie, samopodobné riešenie, statická stabilita, asymptotické aproximácie

AMS klasifikácia: 80A22, 76M45, 35C20

Contents

1 Introduction

Phase change is a phenomenon which occurs on different scales and in various fields. In nature, the processes involving solidification are present in the Earth's core [14], the shelf ice formation [31] or the sediment formation from magma [3], for a recent review, see [8]. A reverse process of solidification (melting and dissolution) can be observed as thawing of permafrost [15]. Apart from nature, there are direct applications in industry such as casting deformity prediction in metallurgy [12] and the modelling of cell cryopreservation in biology [10]. The solidification problems can be formulated within the framework of partial differential equations with a moving boundary of infinitesimally small thickness [13].

During solidification of a pure material, the solid–liquid interface may become thermally supercooled, which enables nucleation as heat is removed from the interfacial regions by convection or conduction (or both). In the case of solidifying a mixture of two or more components, the solidification interface may be exposed to constitutional supercooling, which is caused by segregation of solute into the liquid region. Rejected solute will lower the melting point in the boundary layer of the liquid, thus widening the freezing range of the alloy. This effect (see e. g. [30]) causes the solidifying interface to become morphologically unstable, giving rise to the formation of dendrites. Regions containing liquid and solid phases with dendritic structure are called mushy regions (see [39] or [8]).

1.1 Fixed plate cooling and solidification

Experimental study [21] concerning cooling and solidification of binary alloy from cooled plate conducted on aqueous solution of $NaNO_3$ describes a mixed phase of solid and melt, mushy layer, where the planar interface is morphologically unstable. results are found to be in good agreement with the observed behaviour in [21] of aqueous $NaNO_3$ solutions. A model [37] is in good agreement with the observed behaviour explaining the evolution of a binary mixture from a fixed cooled boundary. The model allows self–similar solutions with both interfaces following the square root law. The numerical results shows that the structure of mushy layer varies considerably with the change of physical parameters of the solidifying system, namely cooling temperature

and initial concentration of solute.

A model for diffusive solidification of a ternary alloy from a cooled boundary was presented by [5]. The model consists of a liquid layer, a primary mushy layer and a secondary mushy layer in accordance with the experimental study on the ternary system mixture H_2O–KNO_3–$NaNO_3$ in [2]. The model includes the effects of thermal and solutal diffusion. Throughout the primary mushy layer the thermodynamic equilibrium is maintained by imposing a linear liquidus constraint between temperature and concentration fields. leaving on additional degree of freedom. The experimental study of [34] on the same ternary system investigated convective scenario in which the secondary mushy layer was both thermally and compositionally stably stratified and the convection originated in the primary mush and the liquid layer due to statically unstable density stratification.

1.2 Lateral directional solidification

A setup related to experimental continuous spin casting processes was analysed in [29] and [26]. The two-dimensional boundary layer flow and solidification of a binary alloy over a horizontally moving plate maintained at constant temperature was analysed. A novel feature that distinguishes this setting from the fixed-plate setups is the occurrence of a non-planar interface between the solid and liquid regions.

The model presented in [27] (the original contribution of the author of this thesis) includes liquid, mushy and solid layers and identifies two-dimensional steady self-similar solutions for the system. The effects of boundary flow on the position of the interfaces and solidification speed were quantified. An asymptotic analysis of the parametric dependence of the characteristics of the solidifying system was performed. A comparison to the case of solidification from a cooled boundary analysed in [37] showed that the formation of a mushy layer in the present setup was more prominent. A generalized model containing two different mushy zones, dispersed and packing, was analysed in [33].

1.3 Vertical directional solidification

Directional solidification of binary mixtures is extensively described in [13]. A model which enables analysis of convective instabilities was developed in [4] by separating

mushy layer from the liquid region above and the solid beneath by fixing its thickness. It has been proved that convective instability in the mushy layer is generally subcritically unstable.

The study of nonlinear development of oscillatory convective instability in the two-dimensional mushy layers was performed in [17], [18]. They found that for both travelling and standing waves oscillatory mode could be supercritically stable, depending on the sensitivity of permeability of the mushy layer. Weakly nonlinear interactions between steady and oscillatory convection were analysed by [18] revealing a rich topology of convective transitions.

In [6] the directional solidification of ternary mixtures was studied and characterisation of convective regimes in terms of two Rayleigh numbers, corresponding to primary and secondary mushy layers, was provided. The convection in the primary mushy layer was found to generally induce a flow (comparable in magnitude) in the liquid layer, but only a weak flow in the secondary layer. On the other hand, convection in the secondary mush would induce flow in the primary mush and the liquid layer if primary layer was not sufficiently stably stratified.

In the presence of multiple diffusive fields convection may arise even though fluid is statically stably stratified, i.e. the fluid density decreases with height. This phenomenon is called double-diffusive convection and originates due to a difference in diffusivities of various fields and is described in [35]. This feature is not present in binary mushy layer systems due to a coupling of thermal and solutal fields through the liquidus constraint. However, in ternary (or multicomponent) solidifying systems double diffusive effects may arise.

To identify the type of convective instability, a single primary mush model was studied in [7], [20]. Under a parametric reduction, namely zero speed of macroscopic solidification, zero Stefan number and by omitting solute segregation effects, linear stability problem associated to base state solution was analytically solved. In this case, even though fluid was statically stably stratified, an instability mode was present as the result of interactions between convection, solidification and diffusion processes within the primary mushy layer. Under the parametric reductions, described above this mode develops only when the diffusivities of the two solutes differ. The numerical results in [7] on the full model describe the situation when statically unexpected direct modes can

occur even in cases when the diffusivities of the two solutes are the same. Therefore, the exceptional direct mode found in their full numerical model must necessarily be distinct from the one described in reduced parametric setup. A special case of this model is a binary mixture solidification model described in [38].

In [19] the stability of a primary mushy layer during the directional solidification of a ternary alloy is analysed. They developed a primary mush model, which contains phase-change effects due to latent-heat release, solute rejection and background solidification, which were not considered in the analytically solved model from [7]. The model identifies novel convective instabilities, both direct and oscillatory, which are present under statically stable conditions. An asymptotic analysis was carried out with respect to small thickness of primary mush with small growth rates. A physical explanation for these instabilities was proposed, indicating that the instability mechanisms generally involve different rates of solute diffusion, different rates of solute rejection and different background solute distributions induced by the initial alloy composition.

In [22] we considered a number of parametric reductions under which the base state solution, with non-zero speed of macroscopic solidification and partial solute segregation, can by analytically expressed. The effect of different liquid and solid conductive properties has been observed to split mushy layer into two distinct zones the bottom one with large representation of solid phase and top one consisting of mainly melt. The most general case corresponded to the same diffusion properties of solutes and also solute rejection rates. Parametric conditions for the existence of base state solution were provided. A linear character of the static stability curves in the parametric space spanned by initial compositions was established.

In chapter §4, which is an extension of [23] (the original contribution of the author of this theses) we consider directional solidification of ternary mixtures, incorporating thermal and solutal diffusion, segregation effects and finite speed of the background solidification. Apart from the boundary conditions prescribing constant concentrations on the top and the bottom of the primary mush, we also consider a boundary condition setup with fixed concentration gradients at the bottom. We present analytical solutions for the steady non-convecting state, building on the results from [22], which consider the Lewis numbers and the segregation coefficients equal for both solutes.

The dissertation is organized as follows. In §2 we provide a general introduction

to alloy solidification and describe equations governing a mushy layer in binary alloys, with governing equations formulated in a general frame of reference. In §3 we describe solidification of binary alloy with horizontally moving substrate, based on [27]. In §4 we consider a model for the solidification of ternary alloys. In §5 the model is reduced to a primary mush model, following [7], [19], [22], [20] and [23], while considering novel boundary conditions, and then we provide asymptotic results for the ternary base state solution.

2 Solidification of multicomponent alloys

2.1 Phase diagram

A component is a chemically recognizable species. Each component or their combination can exhibit a number of different phases. A phase is a portion of a system that has uniform physical and chemical characteristics.

A multicomponent alloy is a thermodynamic system consisting of n components. For simplicity we will present conservation equations and phase diagram for the case $n = 2$, i.e. a binary alloy. We will refer to the components of binary system A and B, as solvent and solute respectively. A binary phase diagram represents the linkage between temperature and concentration of solute, which indicates the equilibrium phases present at a given pressure, temperature and concentration. All states, which system in thermodynamic equilibrium can exhibit are in the phase diagram. A typical binary system, as one sketched in figure 1, consist of phases formed by solids of component A, B and mixture of solid solutions of components A and B denoted α, β and $\alpha + \beta$ respectively; of phases where liquid and solid, composed either from A or B component, are both present denoted $\alpha + L$ and $\beta + L$ respectively; and of liquid phase L.

Curves depicted in a binary phase diagrams represent boundaries between different states which system can exhibit. Most important features of a phase diagram are:
Liquidus - The line separating liquid-phase field from the liquid-plus-solid phase
Solidus - The line separating the solid-phase field from liquid-plus-crystals phase field.
Solvus - The line separating the single-solid phase field from mixture of solid solutions phase field.
Eutectic point -The point on a phase diagram where the maximum number of allowable phases are in equilibrium. In this point the chemical composition and temperature corresponds to the lowest melting point of a mixture of components.
Eutectic isotherm - The horizontal solidus line at eutectic temperature T_E.

2.2 Governing equations for binary mushy layers

2.2.1 Cooling from a fixed boundary

Governing equations for solidification of a binary mixture are described in [39]. These equations are independent of the internal morphology of growing dendrites, thus being suitable for a wide range of solidifying systems. The justification for this continuum approach is the fact that the distance between the dendrites is small compared to the height of the mushy layer as can be seen in figure 2. The governing equations represent the local conservations for heat and solute. This approach assumes the homogeneous distribution and morphology of dendrites. The physical properties of the mush are functions of the local solid fraction $\phi(\boldsymbol{x}, t)$. The thermal properties of the mush are approximated by the average of properties of solid and liquid properties as

$$k_m = (1-\phi)\, k_l + \phi k_s, \tag{2.1a}$$

$$(\rho C_p)_m = (1-\phi)\, \rho_l C_{pl} + \phi \rho_s C_{ps}, \tag{2.1b}$$

where the subscripts l and s denotes the liquid and the solid phases, respectively, k represents thermal conductivity, ρ density and C_p specific heat.

Local conservation of heat and solute, denoting the solute concentration by C, the temperature by T take the form

$$(\rho C_p)_m \frac{\partial T}{\partial t} = \boldsymbol{\nabla\cdot}\left(k_m \boldsymbol{\nabla} T\right) + \rho_s L \frac{\partial \phi}{\partial t}\ , \tag{2.2a}$$

$$(1-\phi)\frac{\partial C}{\partial t} = \boldsymbol{\nabla\cdot}\left(D(\phi)\,\boldsymbol{\nabla} C\right) + (C - C_s)\frac{\partial \phi}{\partial t}\ , \tag{2.2b}$$

where $D(\phi) = D(1-\phi)$ is the solutal diffusivity of the two-phase mush, D is the liquid solute diffusivity and L is the latent heat. The last term on the right-hand side of heat equation, $\rho_s L \partial\phi/\partial t$, represents the release of latent heat. The last term on the right-hand side of solute equation, $(C - C_s)\,\partial\phi/\partial t$, represents the release of solute during solidification.

2.2.2 Governing equations in a general frame of reference

In [32] the governing equations fora binary mush in the general frame of reference are presented. The formulation involves the interface velocity $\boldsymbol{w}$, the velocity of the dendrites $\boldsymbol{v}$ and the fluid velocity $\boldsymbol{u}$. The solid velocity is equal to the velocity of a

point embedded in the dendrites. The fluid velocity is an average over the fluid portion of a representative region. The total flux vector is defined as $\boldsymbol{q} = \chi \boldsymbol{u} + \phi \boldsymbol{v}$, where ϕ and $\chi = 1 - \phi$ are the local solid and liquid volume fractions in the mush.

The material derivatives with respect to velocities $\boldsymbol{v}$, $\boldsymbol{u}$ and $\boldsymbol{q}$ are denoted as D^s, D^l, D, respectively. In the general frame of reference, the governing equations take the form

$$(\rho C_p)_m \frac{\mathrm{D}T}{\mathrm{D}t} = \boldsymbol{\nabla\cdot} \left(k_m \boldsymbol{\nabla} T\right) + \rho_s L \frac{\mathrm{D}^s \phi}{\mathrm{D}t}, \tag{2.3a}$$

$$\frac{\mathrm{D}C}{\mathrm{D}t} - \phi \frac{\mathrm{D}^s C}{\mathrm{D}t} = \boldsymbol{\nabla\cdot} \left(D\left(\phi\right) \boldsymbol{\nabla} C\right) + \left(C - C_s\right) \frac{\mathrm{D}^s \phi}{\mathrm{D}t}, \tag{2.3b}$$

$$T = T_M + \Gamma C, \tag{2.3c}$$

$$\boldsymbol{q} - \boldsymbol{v} = -\frac{\Pi\left(\phi\right)}{\mu} \left(\boldsymbol{\nabla} p + \rho g \hat{\boldsymbol{k}}\right), \tag{2.3d}$$

$$\boldsymbol{\nabla\cdot q} = 0, \tag{2.3e}$$

where $\Pi\left(\phi\right)$ is the permeability of the mush, which is a prescribed function of ϕ, μ is the dynamic viscosity, p is pressure, T_M is the melting temperature of component A and Γ is liquidus slope for component B. Equation (2.3c) represents a linear approximation of liquidus. This approximation is appropriate for many systems, including aquaeous solutions Equation (2.3d) governs velocity field, its name is Darcy equation, and describes the flow of a fluid through a porous medium.

When $\boldsymbol{v} = \boldsymbol{0}$ equations (2.3a, 2.3b) reduce to (2.2a, 2.2b) representing the case of cooling from a fixed boundary.

When $\boldsymbol{v} = -V\hat{\boldsymbol{k}}$ the case of directional solidification with the pulling speed V is obtained.

When $\boldsymbol{v} = -U_0\hat{\boldsymbol{i}}$, the case of the solidification over the horizontally moving substrate is obtained, related to the continuous spin casting processes studied for example in [29] and [26]. §3, which builds on [27], considers this setup.

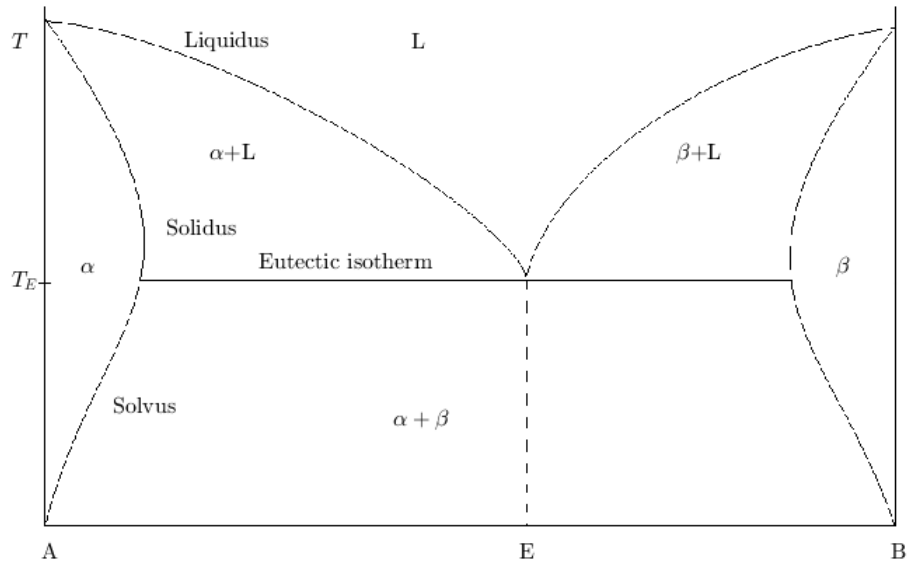

Figure 1: Binary phase diagram. This plot represents a binary phase diagram, where the vertical axis represents temperature and the horizontal axis represents the concentration of B component starting at zero in the left corner (phase A) and ending in the right corner (phase B). Regions separated by The liquidus, solidus, solvus and eutectic isotherm curves are denoted as L (liquid region), α (region containing A component rich solid α), α+L (region containing A component rich solid α and liquid), $\alpha + \beta$ (region containing solid formed from mixture of components A and B); and analogous regions for B component.

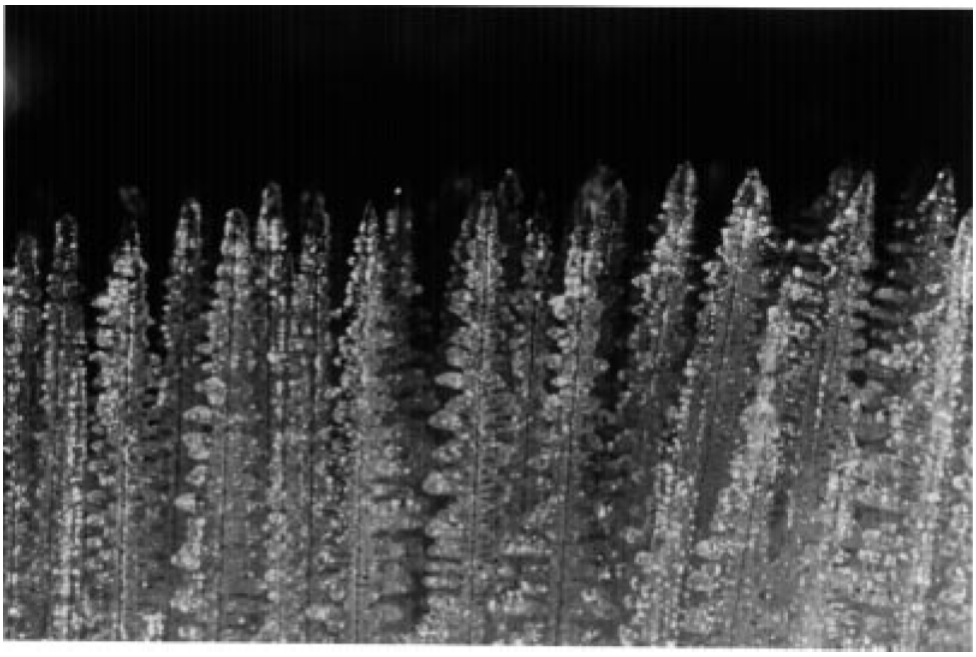

Figure 2: A binary mushy layer. This photograph, taken from [39], depicts the individual dendrites growing from the aqueous solution of NH_4Cl. The typical spacing between the dendrites shown is about 0.5 mm, while the depth of the mushy layer is a few centimeters.

3 Solidification and flow of a binary alloy over a moving substrate

This chapter is based on our paper [27].

3.1 Model formulation

The region $x^* > 0$, $z^* > 0$ is filled with a binary alloy with the temperature and solute concentration T^*_∞ and C^*_∞ as $z^* \to \infty$, respectively. The solidification occurs from the cooled substrate $z^* = 0$, which moves horizontally at a constant speed $U^*_0 > 0$. The substrate is maintained the temperature $T^*_L(C^*_0)$, which by liquidus constraint corresponds to a concentration C^*_0. We assume that $T^*_L(C^*_0)$ is above the eutectic temperature T^*_E and below $T^*_L(C^*_\infty)$. We consider a situation where the binary-alloy mushy region forms between solid and liquid regions. We denote positions of the solid–mush and the mush–liquid interfaces as $z^* = a^*(x^*)$ and $z^* = b^*(x^*)$, respectively. We denote the local volume fraction of solid phase as ϕ. Note that even though interfaces are stationary, the solid phase moves together with the substrate. The situation described above is illustrated in figure 3.

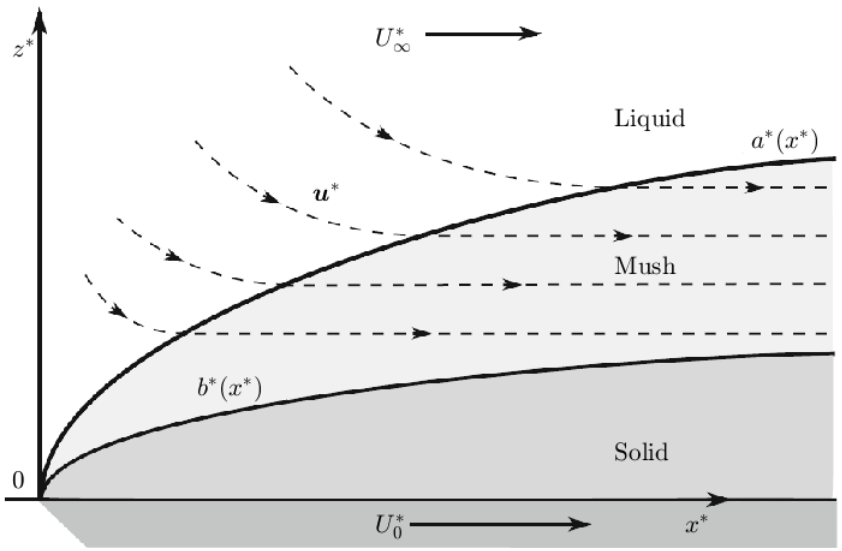

Figure 3: A sketch for the geometry of the solidification of a binary alloy over a horizontally moving substrate.

The governing equations for temperature, concentration and solid fraction fields in mushy layer are based on local conservation laws of heat and solute derived in [32]. In general, the velocity of solid dendrites, interstitial fluid and propagation rate of interfaces are distinct. The pressure in mushy layer is purely hydrostatic and there is no flow of interstitial fluid relative to the solid dendrites. We denote the flow velocity as $\boldsymbol{u}^* = (u^*, w^*)$ in the liquid and mushy regions, and the velocity of the solid phase as $\boldsymbol{v}^* = U_0^* \hat{\boldsymbol{i}}$, where $\hat{\boldsymbol{i}}$ is unit vector in horizontal direction. In the mush, the velocity field is $\boldsymbol{u}^* = \boldsymbol{v}^*$. A simple binary phase diagram used, is depicted in figure 4. We assume that there is no mass diffusion in the solid and that the solid is free of solute. Then the liquidus constraint in the takes the form

$$T_L^*(C^*) = T_L^*(C_0^*) - \Gamma^*(C^* - C_0^*). \tag{3.1}$$

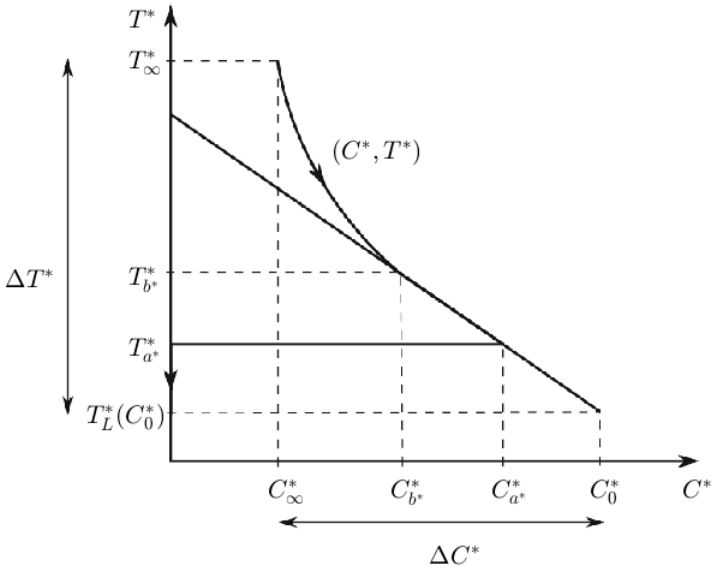

Figure 4: Idealized binary phase diagram for a system with a mushy region, used in this chapter. A typical solidification path (solid line with arrows) is depicted in C^* vs. T^* plane.

In the far boundary

$$T^* = T^*_\infty,\ C^* = C^*_\infty,\ u^* = U^*_\infty \text{ as } z^* \to \infty, \tag{3.2}$$

where T^*_∞, C^*_∞ and U^*_∞ are the prescribed constants. In the liquid, the dimensional governing equations are

$$(\boldsymbol{u}^*\boldsymbol{\cdot}\boldsymbol{\nabla}^*)\,\boldsymbol{u}^* = -\boldsymbol{\nabla}^* p^* - \rho^* g^* \hat{\boldsymbol{k}} + \mu^* \boldsymbol{\nabla}^{*2}\boldsymbol{u}^*, \tag{3.3a}$$

$$\boldsymbol{u}^*\boldsymbol{\cdot}\boldsymbol{\nabla}^*\, T^* = \kappa_l^* \boldsymbol{\nabla}^{*2} T^*, \tag{3.3b}$$

$$\boldsymbol{u}^*\boldsymbol{\cdot}\boldsymbol{\nabla}^*\, C^* = D^* \boldsymbol{\nabla}^{*2} C^*, \tag{3.3c}$$

$$\boldsymbol{\nabla}^*\boldsymbol{\cdot}\boldsymbol{u}^* = 0, \tag{3.3d}$$

where (3.3a,3.3d) are incompressible Navier–Stokes equations, and (3.3b) and (3.3c) are advection–diffusion equations governing temperature and concentration, respectively.

At the mush–liquid interface at $z^* = b^*(x^*)$

$$U_0^* L_v^* \frac{db^*}{dx^*}\phi_{b^{*-}} = \bar{k}^*(\phi)\left.\frac{\partial T^*}{\partial z^*}\right|_{b^{*-}} - k_l^*\left.\frac{\partial T^*}{\partial z^*}\right|_{b^{*+}}, \tag{3.4a}$$

$$U_0^* \frac{db^*}{dx^*}\phi_{b^{*-}} = D^*\left.\frac{\partial C^*}{\partial z^*}\right|_{b^{*+}} - (1-\phi_{b^{*-}})\left.\frac{\partial C^*}{\partial z^*}\right|_{b^{*-}}, \tag{3.4b}$$

$$\left[\frac{\partial T^*}{\partial x^*} + \frac{db^*}{dx^*}\frac{\partial T^*}{\partial z^*}\right]\Bigg|_{b^{*+}} = \Gamma^*\left[\frac{\partial C^*}{\partial x^*} + \frac{db^*}{dx^*}\frac{\partial C^*}{\partial z^*}\right]\Bigg|_{b^{*+}}, \tag{3.4c}$$

$$T^* = T_L^*(C_0^*) - \Gamma^*(C^* - C_0^*),\; u^* = U_0^*,\; w^* = 0, \tag{3.4d}$$

where (3.4a), (3.4b) and (3.4c) represents heat conservation, solute conservation and marginal equilibrium condition, respectively. The marginal equilibrium condition was introduced by [37], stating that liquid ahead of the mush–liquid interface is not constitutionally supercooled.

Governing equations in the mushy region $a^*(x^*) < z^* < b^*(x^*)$ are

$$\bar{c}^*(\phi) U_0^* \frac{\partial T^*}{\partial x^*} = \boldsymbol{\nabla^*}\boldsymbol{\cdot}\left[\bar{k}^*(\phi)\boldsymbol{\nabla^*} T^*\right] + U_0^* L_v^* \frac{\partial \phi}{\partial x^*}, \tag{3.5a}$$

$$U_0^* \frac{\partial}{\partial x^*}\left[\phi C^*\right] = \boldsymbol{\nabla^*}\boldsymbol{\cdot}\left(D^*(1-\phi)\,\boldsymbol{\nabla^*} C^*\right), \tag{3.5b}$$

$$T^* = T_L^*(C_0^*) - \Gamma^*(C^* - C_0^*), \tag{3.5c}$$

where (3.5a), (3.5b) are advection–diffusion equations for temperature and concentration respectively and (3.5c) represents liquidus constraint. The solid fraction ϕ throughout mushy layer is unknown. The state of thermodynamic equilibrium is maintained by liquidus constraint (3.5c). Note that governing equations for velocity profile are not presented, because solution of form $\boldsymbol{u^*} = \boldsymbol{v^*}$ is expected.

At the mush–solid interface positioned at $z^* = a^*(x^*)$ are satisfied

$$U_0^* \frac{da^*}{dx^*}(1-\phi_{a^{*+}})\, C^*|_{a^{*+}} = D^*(1-\phi_{a^{*-}})\, \left.\frac{\partial C^*}{\partial z^*}\right|_{a^{*-}}, \tag{3.6a}$$

$$U_0^* L_v^* \frac{da^*}{dx^*}(1-\phi_{a^{*+}}) = k_s^* \left.\frac{\partial T^*}{\partial z^*}\right|_{a^{*-}} - \bar{k}^*(\phi) \left.\frac{\partial T^*}{\partial z^*}\right|_{a^{*+}}, \tag{3.6b}$$

$$T^* = T_L^*(C_0^*) - \Gamma^*(C^*|_{a^{*+}} - C_0^*). \tag{3.6c}$$

These equations as at the liquid–mush interface, represent local conservation laws and liquidus constraint.

In solid phase $0 < z^* < a^*(x^*)$

$$c_s^* U_0^* \frac{\partial T^*}{\partial x^*} = k_s^* \nabla^{*2} T^*, \tag{3.7}$$

the temperature field is governed by diffusion only, while substrate temperature is fixed at

$$T^* = T_L^*(C_0^*). \tag{3.8}$$

3.2 Non-dimensionalisation

In this chapter we consider scaling in which lengths will be scaled by a factor κ^*/U_0^*, and velocities by U_0^*. The dimensionless temperature and concentration are defined as

$$T = \frac{T^* - T_L^*(C_0^*)}{\Delta T^*} \qquad \text{and} \qquad C = \frac{C_0^* - C^*}{\Delta C^*} \tag{3.9}$$

respectively, where $\Delta T^* = T_\infty^* - T_L^*(C_0^*)$ and $\Delta C^* = C_0^* - C_\infty^*$. We define non-dimensional positions of interfaces as

$$a(x) = \frac{a^*(\kappa^* x/U_0^*)}{\kappa^*/U_0^*} \qquad \text{and} \qquad b(x) = \frac{b^*(\kappa^* x/U_0^*)}{\kappa^*/U_0^*}. \tag{3.10}$$

The dimensionless numbers characterizing process of solidification are the Lewis number Le, the Stefan number S, the concentration ratio $\mathcal{C}$ and the dimensionless liquidus slope Γ defined respectively, by

$$Le = \frac{\kappa^*}{D^*}, \quad S = \frac{L_v^*}{c^* \Delta T^*}, \quad \mathcal{C} = \frac{C_0^*}{\Delta C^*}, \quad \Gamma = \frac{\Gamma^* \Delta C^*}{\Delta T^*}. \tag{3.11}$$

Note that range of $\mathcal{C}$ is $(1, \infty)$ and range of Γ is $(0, 1)$. It is good to keep in mind, that limit case $\Gamma = 1$ corresponds to situation when far field values (C_∞^* and T_∞^*) satisfy the liquidus constraint.

The dimensionless numbers in liquid are the Prandtl Pr number and the velocity ratio $\mathcal{U}$

$$Pr = \frac{\mu^*}{\kappa^*} \qquad \text{and} \qquad \mathcal{U} = \frac{U_\infty^*}{U_0^*}. \tag{3.12}$$

We consider the limit

$$\xi = \frac{z}{2\sqrt{x}} = O(1) \qquad \text{as} \qquad x \to \infty. \tag{3.13}$$

The effects, of this limit can be accounted for by applying the transformation $(x, z) \to \left(l\tilde{x}, l^{1/2}\tilde{z}\right)$ considering the leading order balance, and then neglecting the pressure gradient in the casting direction. Note that by (3.3a), the pressure is hydrostatic. After resolving the limit, we return to the original coordinates (x, z). The resulting system of boundary-layer equations is as follows. In the far boundary:

$$T = 1,\, C = 1,\, u = \mathcal{U} \qquad \text{as} \qquad z \to \infty. \tag{3.14}$$

In the liquid phase ($z > b$):

$$u\frac{\partial u}{\partial x} + w\frac{\partial u}{\partial z} = Pr\frac{\partial^2 u}{\partial z^2}, \tag{3.15a}$$

$$u\frac{\partial T}{\partial x} + w\frac{\partial T}{\partial z} = \frac{\partial^2 T}{\partial z^2}, \tag{3.15b}$$

$$u\frac{\partial C}{\partial x} + w\frac{\partial C}{\partial z} = \frac{1}{Le}\frac{\partial^2 C}{\partial z^2}, \tag{3.15c}$$

$$\frac{\partial u}{\partial x} + \frac{\partial w}{\partial z} = 0. \tag{3.15d}$$

At mush–liquid interface ($z = b$):

$$S\frac{db}{dx}\phi_{b^-} = \left[\frac{\partial T}{\partial z}\right]_{b^+}^{b^-}, \tag{3.16a}$$

$$\frac{db}{dx}\left(\mathcal{C} - C\right)\phi_{b^-} = \frac{1}{Le}\left[(1-\phi)\frac{\partial C}{\partial z}\right]_{b^-}^{b^+}, \tag{3.16b}$$

$$\left[\frac{\partial T}{\partial x} + \frac{db}{dx}\,\frac{\partial T}{\partial z}\right]\Bigg|_{b^+} = \Gamma\left[\frac{\partial C}{\partial x} + \frac{db}{dx}\,s\frac{\partial C}{\partial z}\right]\Bigg|_{b^+}, \tag{3.16c}$$

$$T = \Gamma C,\, u = 1,\, w = 0. \tag{3.16d}$$

In the mush ($a < z < b$):

$$\frac{\partial T}{\partial x} = \frac{\partial^2 T}{\partial z^2} + S\frac{\partial \phi}{\partial x}, \tag{3.17a}$$

$$\frac{\partial}{\partial x}\left[(1-\phi)\left(C - \mathcal{C}\right)\right] = \frac{1}{Le}\frac{\partial}{\partial z}\left[(1-\phi)\,\frac{\partial C}{\partial z}\right], \tag{3.17b}$$

$$T = \Gamma C. \tag{3.17c}$$

At mush–solid Interface ($z = a$):

$$S\frac{da}{dx}\left(1-\phi_{a^+}\right) = \left[\frac{\partial T}{\partial z}\right]_{a^+}^{a^-}, \tag{3.18a}$$

$$\frac{da}{dx}\left(\mathcal{C}-C\right)\left(1-\phi_{a^+}\right) = \frac{1}{Le}(1-\phi)\left.\frac{\partial C}{\partial z}\right|_{a^+}, \tag{3.18b}$$

$$T|_{a^+} = \Gamma\, C|_{a^+}\,. \tag{3.18c}$$

In the solid phase ($0 < z < a$):

$$\frac{\partial T}{\partial x} = \frac{\partial^2 T}{\partial z^2}. \tag{3.19}$$

At the bottom,

$$T = 0 \qquad \text{at} \qquad z = 0. \tag{3.20}$$

3.3 Self-similar reduction

The following assumptions allows us to make a self-similar transformation, as in [29]:

- All material properties are the same for liquid and solid phases: $c_s^* = c_l^*$, $k_s^* = k_l^*$, $\kappa^* \equiv k_s^*/c_s^* = k_l^*/c_l^*$ and $c^* = c_s^* = c_l^*$.
- No pressure gradient in the casting direction ($\partial p^*/\partial x^* = 0$). This is valid for film flows with the free stream velocity $U_\infty^* \gg (g^* l^*)^{1/2}$, where g^* is the gravity acceleration and l^* is the height of free surface.
- The ratio between the velocities of substrate and free stream $\mathcal{U} = U_\infty^*/U_0^*$ satisfies $Pr \ll \mathcal{U} \ll Pr^{-1}$. This assumption is easily satisfied by the materials such as metals, where Pr typically has values from 0.1 to 0.01.

Under these conditions equation (3.15a) in the liquid defines a viscous boundary layer problem for fluid velocity in the liquid phase as in [29] and [26]. Noting, that the velocity field in the liquid is decoupled from other fields, we can express $\boldsymbol{u}$ in term of asymptotic expansion for small Pr. The asymptotic form can be found by the method of matched asymptotic expansions. Velocity field can be described using the stream function ψ defined by

$$u = \frac{\partial \psi}{\partial z}, \quad w = -\frac{\partial \psi}{\partial x}. \tag{3.21}$$

We seek a self-similar solution of the form:

$$\psi(x,z) = 2x^{1/2} f(\xi), \text{ where} \qquad \xi = \frac{z}{2\sqrt{x}} = O(1) \qquad \text{as} \qquad Pr \to 0, \tag{3.22}$$

with the positions of dimensionless interfaces given as

$$a(x) = 2\lambda_a x^{1/2} \qquad \text{and} \qquad b(x) = 2\lambda_b x^{1/2}, \tag{3.23}$$

where λ_a and λ_b are constants yet to be determined and f satisfies the boundary value problem described in [29] and [26]:

$$Prf''' + 2ff'' = 0 \tag{3.24a}$$

$$f = \lambda_b \qquad \text{at} \qquad \xi = \lambda_b \tag{3.24b}$$

$$f' \to \mathcal{U} \qquad \text{as} \qquad \xi \to \infty, \tag{3.24c}$$

where $f' = \mathrm{d}f/\mathrm{d}\xi$. Uniformly asymptotic solution of the boundary layer problem (3.24) is:

$$f \sim \lambda_b (1-\mathcal{U}) + \mathcal{U}\xi + Pr\frac{1-\mathcal{U}}{2\lambda_b}\left[1 - \exp\left(-2\lambda_b \frac{\xi - \lambda_b}{Pr}\right)\right]. \tag{3.25}$$

Asymptotic formula (3.25) holds, while the following condition is satisfied

$$\frac{Pr}{\lambda_b} \ll \lambda_b. \tag{3.26}$$

Components of the velocity field in the liquid are

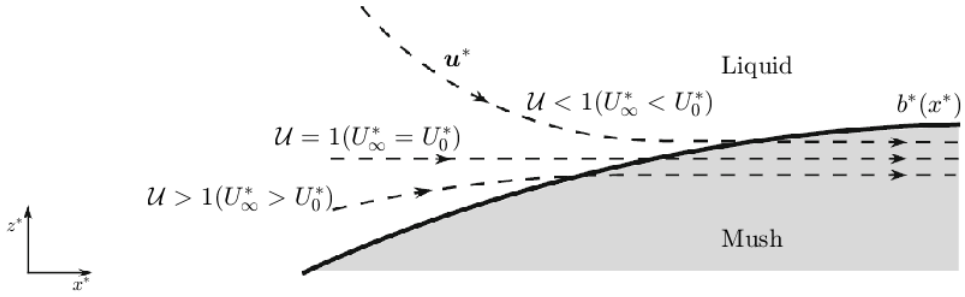

Figure 5: Sketch of representative streamlines for qualitatively different values of $\mathcal{U}$. In the mushy region, the velocity field is equal to the velocity of the solid dendrites embedded within the substrate.

$$u \sim 1 + (1-\mathcal{U})\left[\exp\left(-2\lambda_b \frac{\xi-\lambda_b}{Pr}\right) - 1\right], \tag{3.27a}$$

$$w \sim -\frac{1-\mathcal{U}}{x^{1/2}}\left[\lambda_b + \frac{Pr}{2\lambda_b} - \left(\xi + \frac{Pr}{2\lambda_b}\right)\exp\left(-2\lambda_b \frac{\xi-\lambda_b}{Pr}\right)\right]. \tag{3.27b}$$

as $Pr \to 0$. In figure 5 are depicted situations with $w > 0$ ($w < 0$) when $\mathcal{U} > 1$ ($\mathcal{U} < 1$). The results when the mushy layer is absent are described in [26]. Note that for $\mathcal{U} = 1$, there is no flow relative to the solid phase, and therefore when space variable x is replaced by the time variable, the problem is formally equivalent to the solidification of a binary alloy with planar solid–mush and mush–liquid interfaces analysed in [37].

A boundary layer problem for temperature distribution in the liquid phase can be obtained as in [26] after applying self-similar transform (3.22) for (3.15b)

$$T'' = -2fT', \tag{3.28a}$$

$$T = T(b) \equiv T_b \qquad \text{at} \qquad \xi = \lambda_b, \tag{3.28b}$$

$$T \to 1 \qquad \text{as} \qquad \xi \to \infty. \tag{3.28c}$$

The solution of (3.28) takes the form:

$$T(\xi) \sim 1 + (T_b - 1)\frac{\operatorname{erfc}\left[\mathcal{U}^{1/2}(\xi-\lambda_b) + \mathcal{U}^{-1/2}\Lambda(\lambda_b)\right]}{\operatorname{erfc}\left[\mathcal{U}^{-1/2}\Lambda(\lambda_b)\right]}, \text{ for } \xi > \lambda_b, \tag{3.29}$$

where

$$\operatorname{erfc} = 1 - \operatorname{erf}(\xi), \quad \operatorname{erf}(\xi) = \frac{2}{\sqrt{\pi}}\int_0^\xi \mathrm{e}^{-s^2}\mathrm{d}s \tag{3.30}$$

and

$$\Lambda(\lambda_b) = \lambda_b + Pr\frac{1-\mathcal{U}}{2\lambda_b}. \tag{3.31}$$

Note that $\Lambda(\lambda_b) \sim \lambda_b + O(Pr)$ as $Pr \to 0$. Temperature distribution in solid phase follows differential equation

$$T'' = -2\xi T'. \tag{3.32}$$

Twice integrating we obtain

$$T = T_a\frac{\operatorname{erf}(\xi)}{\operatorname{erf}(\lambda_a)}, \tag{3.33}$$

where T_a is constant, which will be determined by condition on temperature gradient at solid–mush interface. Using relation (3.33) temperature gradient on the solid–mush interface can be evaluated as

$$T'_{a^-} = \frac{2\lambda_a T_a}{G(\lambda_a)}, \tag{3.34}$$

where $G(\lambda) = \sqrt{\pi}\lambda e^{\lambda^2}\mathrm{erf}(\lambda)$. Concentration in the liquid phase after applying self-similar transform follows a differential equation

$$C'' = -2Lef C', \tag{3.35a}$$

$$C = C_b \qquad \text{at} \qquad \xi = \lambda_b, \tag{3.35b}$$

$$C \to 1 \qquad \text{as} \qquad \xi \to \infty. \tag{3.35c}$$

Solution of (3.35) is

$$C(\xi) \sim 1 + (C_b - 1)\frac{\mathrm{erfc}\left[(\mathcal{U}Le)^{1/2}(\xi - \lambda_b) + (\mathcal{U}/Le)^{-1/2}\Lambda(\lambda_b)\right]}{\mathrm{erfc}\left[(\mathcal{U}/Le)^{-1/2}\Lambda(\lambda_b)\right]}, \text{ for } \xi > \lambda_b. \tag{3.36}$$

In the mush region after self-similar transformation equations are cast into the form

$$-\frac{\phi'}{1-\phi} = \frac{2Le\xi C' + C''}{2Le\xi(\mathcal{C} - C) - C'}, \tag{3.37}$$

$$C'' + 2\xi C' = 2\frac{S}{\Gamma}\xi\phi'. \tag{3.38}$$

Equation (3.37) can be integrated as in [16]:

$$\phi = 1 - (1 - \phi_{b^-})\exp\left(-\int_\xi^{\lambda_b} \frac{2Les C' + C''}{2Les(\mathcal{C} - C) - C'}\right)\mathrm{d}s. \tag{3.39}$$

Conservation of heat and solute at the mush–solid interface is expressed

$$\left[2S\lambda_a(1 - \phi_{a^+}) + \Gamma C'_{a^+}\right]G(\lambda_a) = 2\Gamma\lambda_a C_a, \tag{3.40a}$$

$$\left[2\lambda_a(\mathcal{C} - C_{a^+})\right](1 - \phi_{a^+}) = 0. \tag{3.40b}$$

The conservation of heat and solute at the liquid–mush interface is expressed as

$$2S\lambda_b\phi_{b^-} = \Gamma(C'_{b^-} - C'_{b^+}), \tag{3.41a}$$

$$2Le\lambda_b(\mathcal{C} - C_b)\phi_{b^-} = C'_{b^+} - (1 - \phi_{b^+})C'_{b^-}. \tag{3.41b}$$

Condition (3.41a) was derived using self-similar version of the marginal equilibrium condition

$$T'_{b^+} = \Gamma C'_{b^+}. \tag{3.42}$$

Integrating (3.37), and using (3.40b) gives

$$\int_{\lambda_a}^{\xi}(\mathcal{C} - C)(1 - \phi)\,\mathrm{d}s = \frac{1}{2}\left[2\lambda_b(\mathcal{C} - C) - \frac{1}{Le}C'\right](1 - \phi) \ \ ,\lambda_a < \xi < \lambda_b. \tag{3.43}$$

Evaluation of integral in the mushy layer gives

$$\int_{\lambda_a}^{\lambda_b} (\mathcal{C} - C)\,(1-\phi)\,\mathrm{d}s = \frac{1}{2}\left[2\lambda_b\,(\mathcal{C} - C_b) - \frac{1}{Le}C'_{b^-}\right](1-\phi_{b^-})\,, \tag{3.44}$$

where the value of the integral represent dimensionless amount of solute contained in mushy layer.

For general value of S can be shown that concentration gradient is continuous across interface $C'_{b^+} = C'_{b^-}$ and that $\phi_{b^-} = 0$. To prove that, we manipulate (3.41b) to

$$\phi_{b^-} = Le\,(C'_{b^+} - C'_{b^-})\,/\,[2\lambda_b Le\,(\mathcal{C} - C_b) + C'_{b^-}]\,, \tag{3.45}$$

denominator is positive due to (3.44), and nominator is negative because of (3.41a), under these conditions $\phi_{b^-} = 0$ is only viable option. We also use (3.41b) and (3.37) integrated from λ_a to λ_b to show that $2Le\lambda_a\,(\mathcal{C} - C_{b^+}) - C'_{b^+} = 0$.

3.4 Asymptotic results with latent heat rejection neglected

When Stefan number is set zero, the solution for the temperature, and the concentration in the mushy region is analogous to the solution of the temperature in the solid phase

$$T = T_{a^+}\frac{\operatorname{erf}(\xi)}{\operatorname{erf}(\lambda_a)}, \tag{3.46a}$$

$$C = C_{a^+}\frac{\operatorname{erf}(\xi)}{\operatorname{erf}(\lambda_a)}. \tag{3.46b}$$

Equations (3.41a, 3.41b) represent system of linear equations, when solved we obtain

$$C_{a^+} = \frac{Le\mathcal{C}G\,(\lambda_a)}{1 + LeG\,(\lambda_a)}, \tag{3.47a}$$

$$C'_{a^+} = \frac{2Le\mathcal{C}\lambda_a}{1 + LeG\,(\lambda_a)}. \tag{3.47b}$$

Evaluating (3.46b) at $\xi = \lambda_b$, and using (3.47a) we gain algebraic equation exhibiting only solidification rates constants λ_a and λ_b as unknowns

$$LeG\,(\lambda_a)\left[C_b - \mathcal{C}\frac{\operatorname{erf}(\lambda_b)}{\operatorname{erf}(\lambda_a)}\right] + C_b = 0. \tag{3.48}$$

Using the condition of marginal equilibrium (3.42) and the continuity of concentration gradient, we establish continuity of temperature gradient across the liquid–mush interface $T'_{b^+} = T'_{b^-}$. Equation for growth constant λ_b can be obtained by substituting T' and C' evaluated at $\xi = \lambda_b$ from (3.29) and (3.36) respectively into continuity

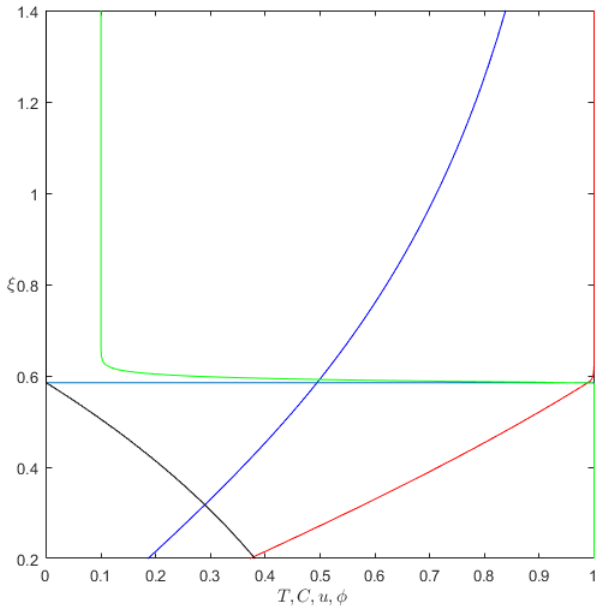

Figure 6: Profiles of temperature (blue), concentration (red), solid fraction (yellow) and x component of the velocity (green) in both liquid and mushy region. Black line that separates liquid region at the top and mushy region at the bottom is position of λ_b liquid–mush interface. For computation in liquid region equations: (3.29), (3.36), (3.27a) were used, position of the liquid–mush interface was computed from (3.48) and (3.49) and for temperature and concentration profiles in the mushy region (3.46), (3.46b) were used. Solid fraction profile was obtained by numerical integration of (3.54). Parameters were set to $C = 2$, $Le = 100$, $\Gamma = 0.5$, $Pr = 0.01$ and $\mathcal{U} = 1/10$, while values on vertical axis satisfy $\xi = O(1)$.

constraints:

$$\frac{\lambda_b}{Le} F\left[\frac{\Lambda(\lambda_b)}{\sqrt{\mathcal{U}/Le}}\right] - \Gamma\lambda_b F\left[\frac{\Lambda(\lambda_b)}{\sqrt{\mathcal{U}}}\right] + (1-\Gamma)\,\Lambda(\lambda_b)\,G(\lambda_b) = 0, \tag{3.49}$$

where

$$F(\lambda) = \sqrt{\pi}\lambda \mathrm{e}^{\lambda^2}\mathrm{erfc}(\lambda). \tag{3.50}$$

Values of temperature and concentration on the mush–liquid interface

$$T_b = 1 - \frac{\lambda_b F\left[\Lambda(\lambda_b)/\sqrt{\mathcal{U}}\right]}{\lambda_b F\left[\Lambda(\lambda_b)/\sqrt{\mathcal{U}}\right] + \Lambda(\lambda_b)\,G(\lambda_b)}, \tag{3.51a}$$

$$C_b = 1 - \frac{\lambda_b F\left[\Lambda(\lambda_b)/\sqrt{\mathcal{U}/Le}\right]}{\lambda_b F\left[\Lambda(\lambda_b)/\sqrt{\mathcal{U}/Le}\right] + Le\Lambda(\lambda_b)\,G(\lambda_b)}. \tag{3.51b}$$

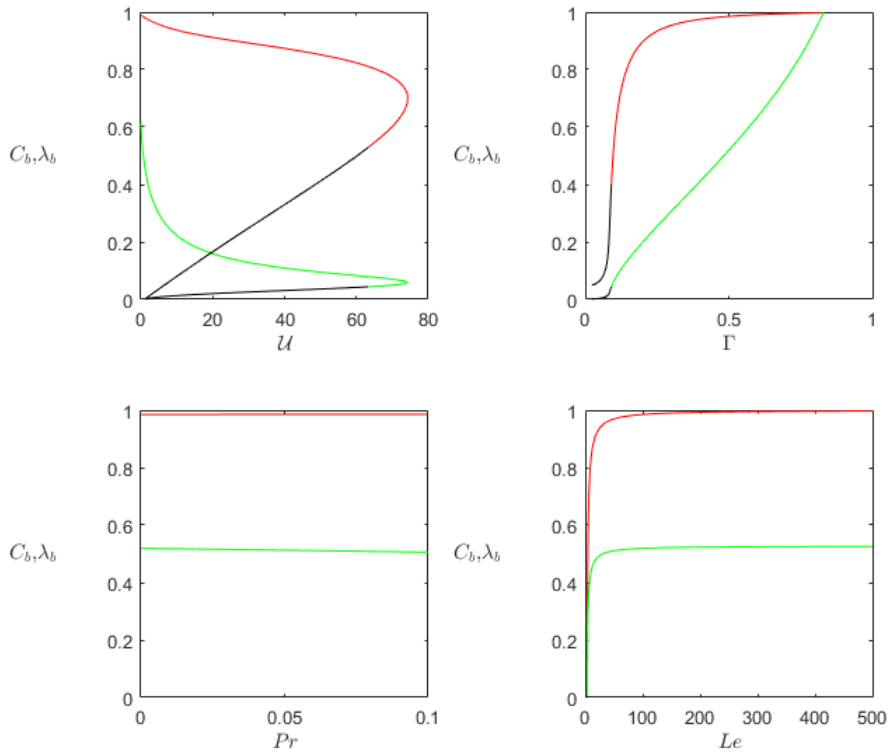

Figure 7: The concentration C_b at the mush–liquid interface, and the position of the mush–liquid interface λ_b as functions of U, Γ, Pr and Le. The plotted values of C_b (red) were computed using (3.51b) and λ_b (green) were calculated from (3.49). Note that for $Le \gtrapprox 100$, C_b and λ_b are almost independent of Le. Parameters used were $\mathcal{U} = 0.5$, $Le = 100$, $\Gamma = 0.5$ and $Pr = 10^{-3}$.

On figure 7 is depicted dependence of both λ_b and C_b on the important non-dimensional parameters evaluated using (3.51b) and (3.49) respectively. Notable is the independence of concentration and mushy layer thickness on Pr, the near linear dependence of mushy layer thickness versus Γ and transition to the small diffusivity limit as $Le \to \infty$.

We present numerical solutions of (3.49) on figure 8. Solutions corresponding to the root $\Lambda(\lambda_b) = 0$ are not presented, because they does not satisfy condition (3.26) i.e. are not asymptotic. Note, that number if solutions of (3.49) depends on values of $\mathcal{U}$. The three intervals $\mathcal{U} \in \langle 0; 1\rangle$, $\mathcal{U} \in \langle 1; \mathcal{U}_{max}\rangle$ and $\mathcal{U} \in \langle \mathcal{U}_{max}; \infty\rangle$ corresponds to one solution, two solutions and no solution scenario respectively. This can be compared to the results obtained in [28], where λ_b existed for all values of $\mathcal{U}$. On figure (9) we observe two branches of λ_b and corresponding values of λ_a are computed for each branch using equation [3.48]. Dashed pair of λ_b and λ_a is for all values of $\mathcal{U}$ physically admissible

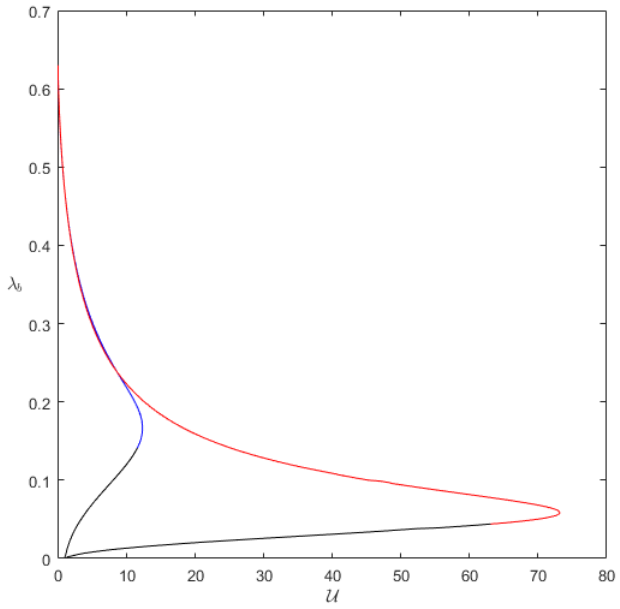

Figure 8: The position of the mush–liquid interface λ_b, as function of the velocity ratio $\mathcal{U}$ computed from (3.49). The red curve correspods to $Pr = 10^{-3}$ and the blue curve corresponds to $Pr = 10^{-2}$. The black portions correspond to the case when criterion $Pr/\lambda_b^2 > 0.5$. The values of other parameters used are $Le = 100$ and $\Gamma = 0.5$.

scenario i.e. $\lambda_a < \lambda_b$. Pair drawn with solid line is physically admissible only for values of $\mathcal{U} > \mathcal{U}_{min} > 1$, where $\mathcal{U}_{min}$ depends on the condition (3.26) and in the plotted case $\mathcal{U}_{min} \sim 8$.

On figure 10 dependence of $\mathcal{U}_{max}$ and associated values of λ_b on Prandtl number is observed. Considering the first order approximation $\lambda_{bmax} \sim \lambda_0 Pr^{1/2}$ and $\mathcal{U}_{max} \sim \mathcal{U}_0 Pr^{-1}$, where $\mathcal{U}_0 = O(1)$ and $\lambda_0 = O(1)$ into (3.49) we gain

$$F\left(\frac{-\mathcal{U}_0^{1/2}}{2Le\lambda_0}\right) - Le\Gamma F\left(\frac{-\mathcal{U}_0^{1/2}}{2\lambda_0}\right) = Le\,(1-\Gamma)\,\mathcal{U}_0\lambda_0. \tag{3.52}$$

Dependence of leading order terms λ_0 and $\mathcal{U}_0$ on parameters Γ and Le can be assessed by considering equation (3.49) as implicit function of $\mathcal{U}\,(\lambda_b)$ and calculating $\frac{\mathrm{d}\mathcal{U}}{\mathrm{d}\lambda_b}$. Solution for λ_0 and $\mathcal{U}_0$ then can be obtained numerically from

$$F'\left(\frac{-\mathcal{U}_0^{1/2}}{2Le\lambda_0}\right) = Le^{1/2}\Gamma F'\left(\frac{-\mathcal{U}_0^{1/2}}{2\lambda_0}\right). \tag{3.53}$$

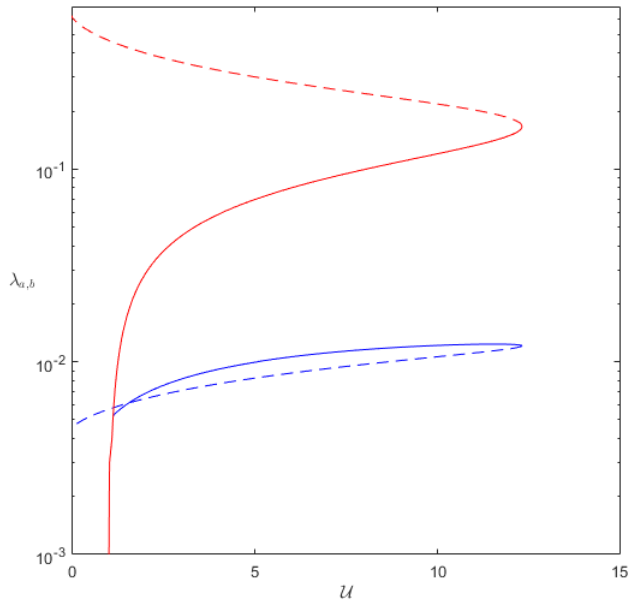

Figure 9: Red colour depicts two branches of λ_b, blue colour is used for λ_a computed numerically from (3.49) and (3.48) respectively. Corresponding branches shares line type. The values of used parameters are $Pr = 10^{-2}$, $Le = 100$, $\Gamma = 0.5$ and $\mathcal{C} = 2$. Note that for y-axis logarithmic scale is used.

The solid fraction integral (3.39) takes the form

$$\phi(\xi) = 1 - \exp\left(- \int_{\xi}^{\lambda_b} \frac{2s\,(Le-1)}{Le\pi^{1/2} s\ \mathrm{e}^{s^2}\left[\left(LeG(\lambda_a)+1\right)/\left(LeG(\lambda_a)\right)\mathrm{erf}(\lambda_a) - \mathrm{erf}(s)\right] - 1} \mathrm{d}s \right). \tag{3.54}$$

3.4.1 Small solutal diffusivity limit

The results in this section were obtained using

$$\mathrm{erf}(x) \sim 2\pi^{-1/2}\mathrm{e}^{-x^2}\left[x + O(x^3)\right] \text{ for } x \ll 1, \tag{3.55}$$

$$\mathrm{erf}(x) \sim \pi^{-1/2}\mathrm{e}^{-x^2}\left[1/x + O(1/x^3)\right] \text{ for } x \gg 1. \tag{3.56}$$

In the limit $Le \to \infty$ a concentration boundary layer of thickness $O(Le^{-1/2})$ forms ahead of the mush–liquid interface. Since $F(s) \sim 1$ and $G(s) \sim s\mathrm{e}^{s^2}$ as $s \to \infty$, the only admissible solution of (3.49) is of the order of unity. Furthermore from (3.51b) we can deduce $C_b \to 1$ as $Le \to \infty$. From (3.48) we have $\lambda_a \to 0$ as $Le \to \infty$, otherwise $\lambda_a > \lambda_b$, which is not admissible. The solution of (3.48) is

$$\lambda_a = \frac{1/Le}{\pi^{1/2}\mathcal{C}\mathrm{erf}(\lambda_b)} + O\left(Le^{-2}\right) \qquad \text{as} \qquad Le \to \infty. \tag{3.57}$$

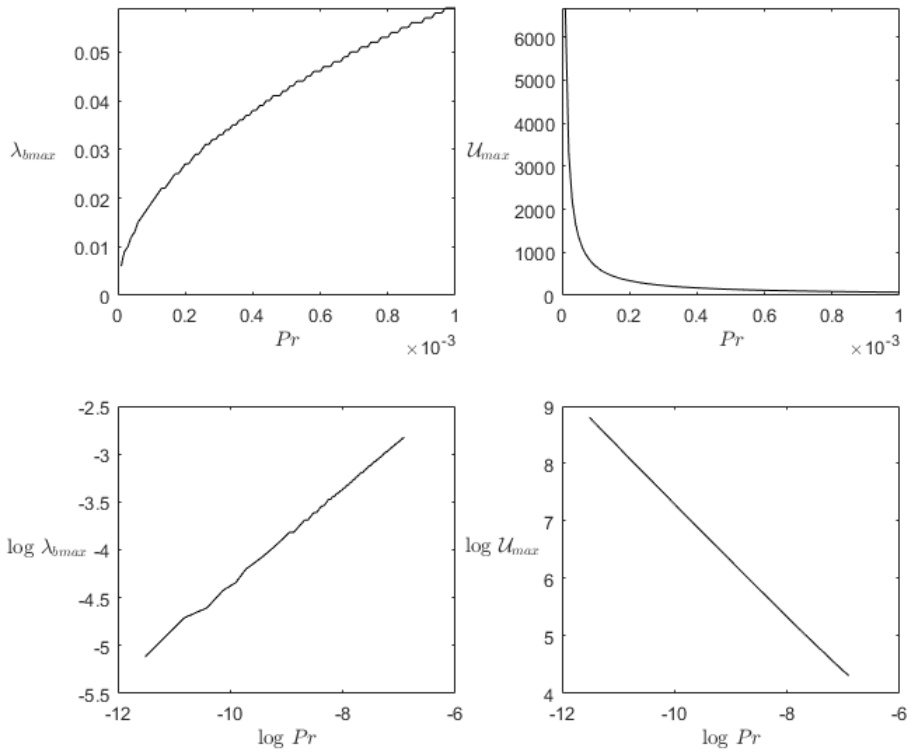

Figure 10: The top plots show $\mathcal{U}_{max}$ and λ_{bmax} as function of Pr. The bottom plots shows the same dependence shown in logarithmic scale. The slopes at the bottom show $\lambda_{bmax} \sim \lambda_0 Pr^{1/2}$ and $\mathcal{U}_{max} \sim \mathcal{U}_0 Pr^{-1}$, where $\mathcal{U}_0 = O(1)$ and $\lambda_0 = O(1)$. Other parameters were set to $Le = 100$ and $\Gamma = 0.5$.

Observe that λ_b, in (3.49), does not depend on the concentration ratio $\mathcal{C}$, so that the thickness of the solid decreases with $\mathcal{C}$. Using (3.57) we can derive concentration and its gradient at the bottom of mushy layer

$$C_a \sim \frac{2\mathcal{C}}{\pi \mathcal{C}^2 \mathrm{erf}^2\left(\lambda_b\right) Le + 2} \tag{3.58}$$

and

$$C_a' \sim \frac{2\pi^{1/2} \mathcal{C}^2 \mathrm{erf}\left(\lambda_b\right)}{\pi \mathcal{C}^2 \mathrm{erf}^2\left(\lambda_b\right) Le + 2}. \tag{3.59}$$

As the limit of $Pr \to 0$ is regular we consider behaviour of (3.49), when $Pr = 0$ so that

$$F\left[\frac{\lambda_b}{\left(\mathcal{U}/Le\right)^{1/2}}\right] - \Gamma F\left[\frac{\lambda_b}{\mathcal{U}^{1/2}}\right] + Le\left(1-\Gamma\right) G\left(\lambda_b\right) = 0. \tag{3.60}$$

Considering a limit $\mathcal{U} \to 0$ for (3.60) a solution can be approximated using:

$$G\left(\lambda_b\right) = \frac{\Gamma}{1-\Gamma}. \tag{3.61}$$

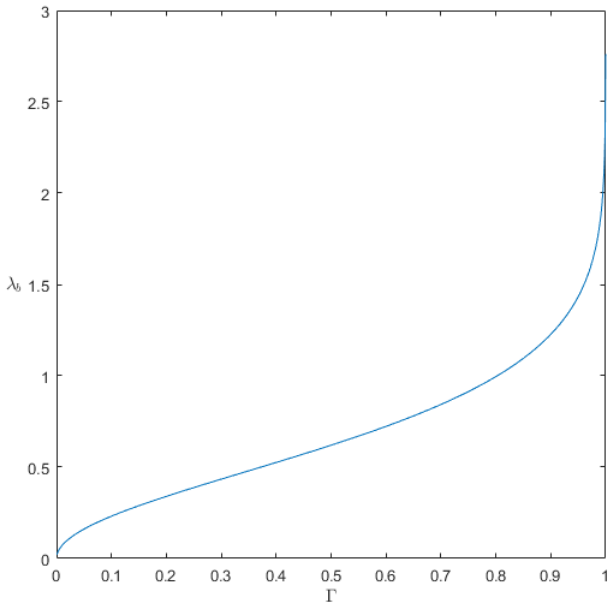

Figure 11: Leading order solution (3.60) computed numerically using (3.61). Note the singularity in λ_b as $\Gamma \to 1^-$.

We note that the dimensionless parameter Γ, which is proportional to the ratio of the compositional and thermal differences across the system satisfy $\Gamma = \left[T_L^*\left(C_\infty^*\right) - T_L^*\left(C_0^*\right)\right]/\Delta T^*$ and that the right-hand side of (3.61) can be expressed as a ratio of the driving temperature differences, i.e. $\left[T_L^*\left(C_\infty^*\right) - T_L^*\left(C_0^*\right)\right] / \left[T_\infty^* - T_L^*\left(C_\infty^*\right)\right]$. The range of G is $(0, \infty)$, and since G is increasing there exists a unique solution for every $\Gamma \in (0, 1)$. Dependence of λ_b on Γ is depicted on figure 11, presented values are numerically computed from (3.61).

3.4.2 Results for for $\mathcal{U} = 0$

Even though limit $\mathcal{U} \to 0$ is regular it is interesting to further investigate the case. Situation $\mathcal{U} = 0$ corresponds to the case, when far field velocity U_∞^* is being set to zero. The growth constants for interfaces λ_a and λ_b are independent of U_0^* and hence we can observe that dimensional position of interfaces

$$a^*\left(x^*\right) = 2\lambda_a \left(\kappa^* x^* / U_0^*\right)^{1/2}, \tag{3.62a}$$

$$b^*\left(x^*\right) = 2\lambda_b \left(\kappa^* x^* / U_0^*\right)^{1/2} \tag{3.62b}$$

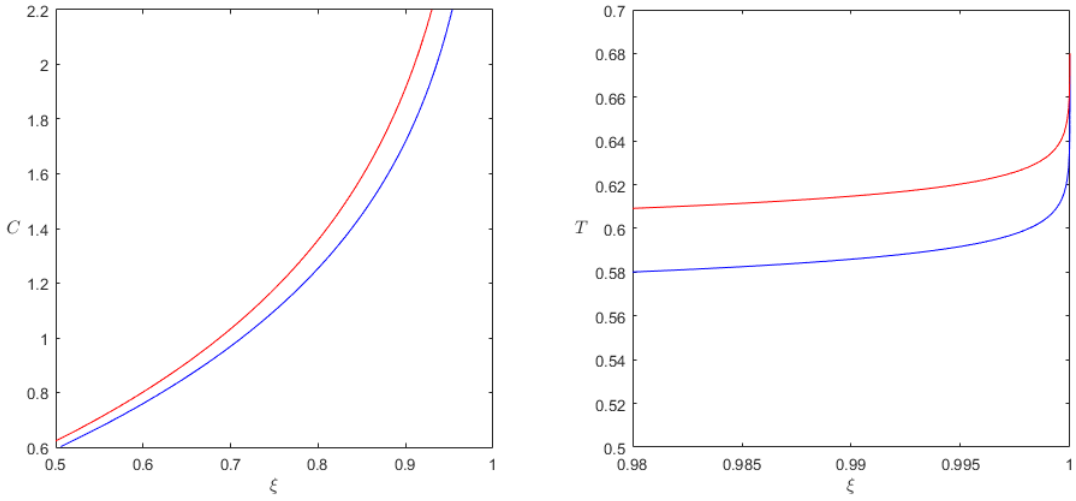

Figure 12: Plots of temperature - (a) and of concentration (b) in the liquid phase as function of ξ on the vertical axis. For $\mathcal{U} = 1/10$, marked with blue, the computation was carried out using equations (3.29) and (3.36). For $\mathcal{U} = 0$, marked red, equations (3.63a) and (3.63b) were used. Other values of parameters are $Pr = 10^{-2}$, $Le = 100$ and $\Gamma = 0.5$.

is proportional to the $(U_0^*)^{-1/2}$. Asymptotic expansion (3.25) holds for $\mathcal{U} = 0$ and therefore the temperature and the concentration in liquid phase can be expressed as

$$T \sim 1 - Le\frac{1-\Gamma}{Le-1}\exp\left[-\frac{2\lambda_b^2 + Pr}{\lambda_b}(\xi - \lambda_b)\right], \tag{3.63a}$$

$$C \sim 1 - \frac{1-\Gamma}{(Le-1)\,\Gamma}\exp\left[-Le\frac{2\lambda_b^2 + Pr}{\lambda_b}(\xi - \lambda_b)\right]. \tag{3.63b}$$

In figure 12 we show typical profiles of the temperature and concentration fields, given by (3.63a,3.63b); shown are also the profiles corresponding to positive values of $\mathcal{U}$. Equation (3.48) is unchanged, while equation for the growth constant λ_b satisfies algebraic equation

$$G(\lambda_b)\left(1 + \frac{Pr}{2\lambda_b^2}\right) = \frac{\Gamma - 1/Le}{1-\Gamma}. \tag{3.64}$$

Positive solution of (3.64) exists only if $\Gamma Le > 1$. By computing derivation of implicitly defined function (3.64) it can be seen, that position of the mush–liquid interface λ_b increases with Γ and Le and is decreasing function of Pr. There are no local extremes present in the range of asymptotically admissible values of parameters.

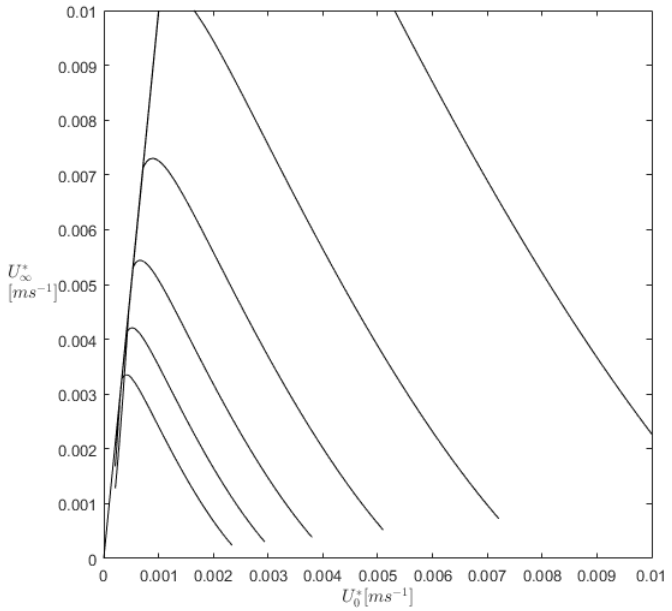

Figure 13: Sequence of equally spaced contour levels of dimensional position (in m) of the mush–liquid interface $b^*(x^*)$. For $x^* = 1m$, $\kappa^* = 5 \times 10^{-6} m^2 s^{-1}$, as in [26]. The range of $\mathcal{U}$ in the plot is $0 \leq \mathcal{U} \leq 10$, while horizontal axis corresponds to $\mathcal{U} = 0$. Note that the non-monotonicity of b^* in the section corresponding to $\mathcal{U} \sim 10$. Other parameters are $Pr = 10^{-2}$, $Le = 100$, $\Gamma = 0.5$.

Considering limits $Pr \to 0$ and $Le \to \infty$ equation (3.64) simplifies to (3.61), which was obtained before.

We can use (3.63b) and (3.44) to calculate the total amount of solute within mushy region as

$$\int_{\lambda_a}^{\lambda_b} (\mathcal{C} - C)(1 - \phi)\, \mathrm{d}s = \lambda_b (\mathcal{C} - 1) - \frac{Pr\,(1 - \Gamma)}{2\lambda_b \Gamma\,(Le - 1)}. \tag{3.65}$$

From (3.65) we can observe that the total amount of solute in the mushy layer is dominantly determined by $\lambda_b (\mathcal{C} - 1)$, while other term being of order $O(Pr/Le)$ as $Le \to \infty$ and $Pr \to 0$. This holds for Γ not too close to 1.

In figure 13 we plot the contours of the dimensional position of the mush–liquid interface, given in (3.62b), for general values of $\mathcal{U}$, in terms of U_0 and U_∞. An interesting feature is the non-monotonicity of b^* as a function of U_0 in the region close to the line $\mathcal{U} = 10$.

In figure 14 we plot the growth constants λ_a and λ_b as functions of Γ, calculated from equations (3.48) and (3.49) together with those corresponding to the mushy region

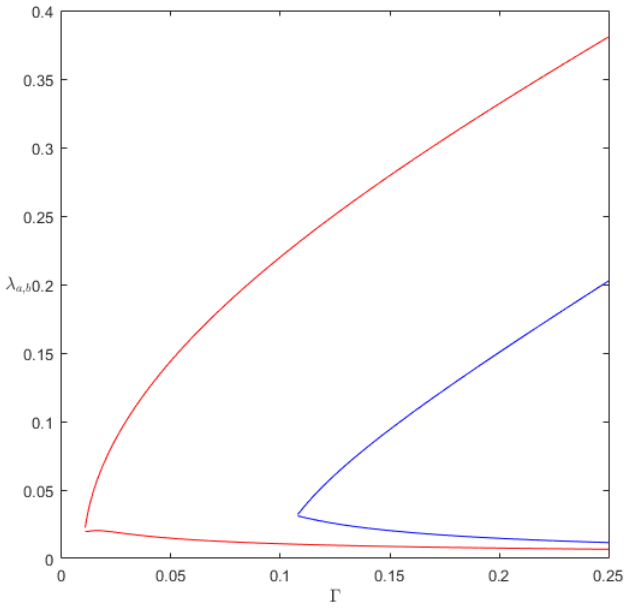

Figure 14: Growth constants λ_a (dashed) and λ_b (solid) are represented as function of Γ. The red pair (case $\mathcal{U} = 0$) was calculated from equations (3.48) and (3.49) and for comparison the blue pair (case $\mathcal{U} = 1$) was calculated from (3.48) and (3.64) and correspond to problem studied by [37]. Other values of parameters are $Pr = 10^{-3}$, $Le = 100$ and $\Gamma = 0.5$.

without horizontal pulling, calculated from (3.48) and (3.64), which correspond to the problem studied by [37]. Note that there exist a value $\Gamma = \Gamma_{min}$ such that $\lambda_a = \lambda_b$. Physically realistic solutions exists only for $\Gamma > \Gamma_{min}$. As Γ approaches 1 behaviour is similar to one observed in figure 11.

In figure 15 we show Γ_{min} as a function of $\mathcal{U}$, the values of Γ_{min} are found to attain their maximum values at $\mathcal{U} = 1$. Thus, the horizontal pulling and the resulting flow in the liquid enhance the formation of a mushy region. in another words: when the system is pulled horizontally, the range of Γ for which the mush exists is larger than that for the system without pulling.

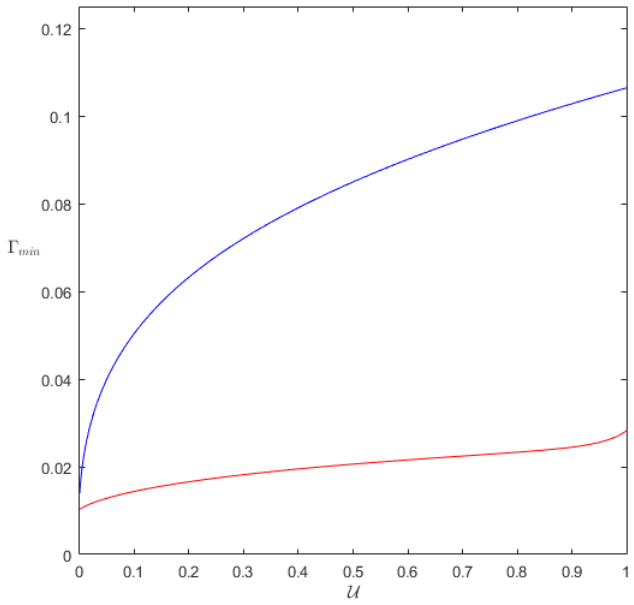

Figure 15: Minimal value of Γ for which mushy region exists, Γ_{min}, as function of $\mathcal{U}$. The plot shows two qualitatively different asymptotic regimes: blue curve corresponds to $Pr \ll 1/Le$ with values $Pr = 10^{-3}$ and $Le = 100$; red curve corresponds to $Pr \gg 1/Le$ with values $Pr = 10^{-2}$ and $Le = 1000$. Note that Γ_{min} attains finite values at $\mathcal{U} = 0$. In all computations $\mathcal{C} = 2$ was used.

4 Directional solidification of ternary alloy

4.1 Ternary phase diagram

The path of an alloy element during solidification with no convection is sketched in figure 16. The concentrations of three components 1, 2 and 3 are denoted by C_1^*, C_2^* and C_3^*, respectively. The concentrations satisfy $C_1^* + C_2^* + C_3^* = 1$. T_M^* represents the melting temperature of the pure component 3; E_{13} is a binary eutectic point for the binary system 1–3, T_E^{13*} and C_{1E}^{13*} are the binary eutectic temperature and concentration for the system 1–3. The cotectic curves intersect at the ternary eutectic point E, with the eutectic temperature T_E^* and the concentrations C_{1E}^*, C_{2E}^* and C_{3E}^*. The phase

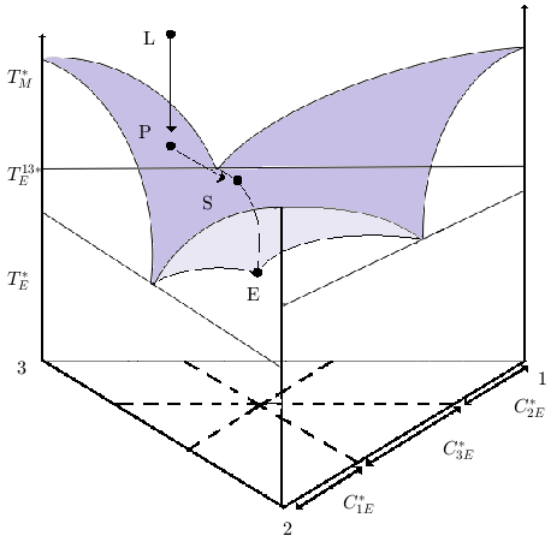

Figure 16: Ternary phase diagram. The base of diagram is the Gibbs triangle, corners 1, 2 and 3 correspond to the respective pure components. Shaded planes represent liquidus surfaces. In the region, above the liquidus surfaces is the liquid phase. At the intersection of two liquidus planes is a cotectic curve. The cotectic curves intersect at the ternary eutectic point E. A sketch of a solidification path L $\rightarrow$ P $\rightarrow$ S $\rightarrow$ E is shown.

diagram can be used for tracking the concentration of cooling melt in a thermodynamic equilibrium. The solidification path depicted in figure 16 starts at point L which lies above the liquidus surface; at this point there is only melt in the liquid phase present. The path continues to the point P , which lies on the liquidus surface and corresponds

to a liquid layer–primary mush interface. In equilibrium the primary solidification of the mushy layer corresponds to the solidification path on the liquidus surface (see for example [7], [19] and [20]).

The phase diagram for the three-component alloys is usually represented in forms of the Gibbs triangle, in which each corner corresponds to a pure component (see e. g. [36]). The solidification process is typically associated with a single corner of the Gibbs triangle. The component in this corner is denoted as 3 while the solutes 1 and 2. Each side of the triangle represents a binary diagram for the respective component pair, for example side 1–2 represents the binary diagram for the binary system with components 1 and 2. Ternary diagrams for metal alloy can be very complex, exhibiting many intermetallic phases. As an example we show in figure 17 the ternary diagram of Pb–Sb–Sn alloy from [24], [25], which includes intermetallic phases, a peritectic point and a eutectic point.

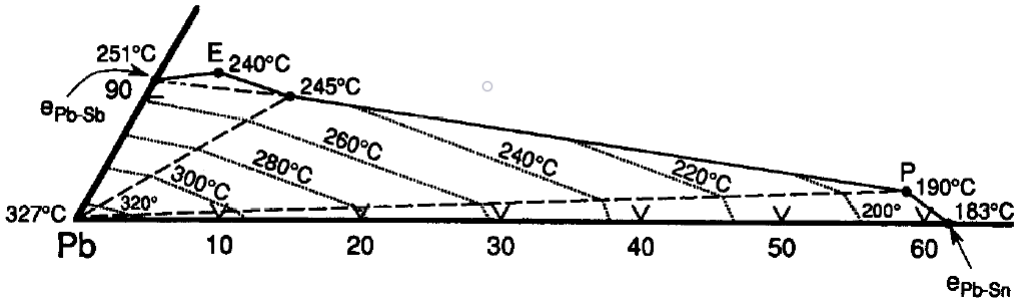

Figure 17: The linearized liquidus surface of the lead rich-corner of Pb–Sb–Sn diagram (taken from [24]). The ternary Pb–Sb–Sn diagram is divided into two sections by the pseudobinary Pb–SbSn system, where SbSn is an intermetallic compound. The Pb–SbSn system has a eutectic point $e_{\text{Pb–SbSn}}$ at 245°C. The partial system Pb–Sb–SbSn has a ternary eutectic point (E) at 240°C. The partial system Pb–Sn–SbSn, has an invariant point, a ternary peritectic (P) at 190°C.

Ternary phase diagrams for aquaeous mixtures are generally much simpler (see e. g. [2]). First, there are no solid solutions (the solvus lines are vertical). Second, all liquidus surfaces are planar.

The thermodynamic equilibrium constraint within the mush associated with the

primary solidification (the primary mush) can be expressed as

$$T_L^*\left(C_1^*, C_2^*\right) = T_M^* + m_1^* C_1^* + m_2^* C_2^*, \tag{4.1}$$

where m_1^* and m_2^* are the liquidus slopes relating the change in temperature to the changes in solute compositions. Concentration of the component 3 can be computed from $C_3^* = 1 - C_1^* - C_2^*$.

A linearized ternary diagram with the liquidus surface and the solidus surface is sketched in figure 18.

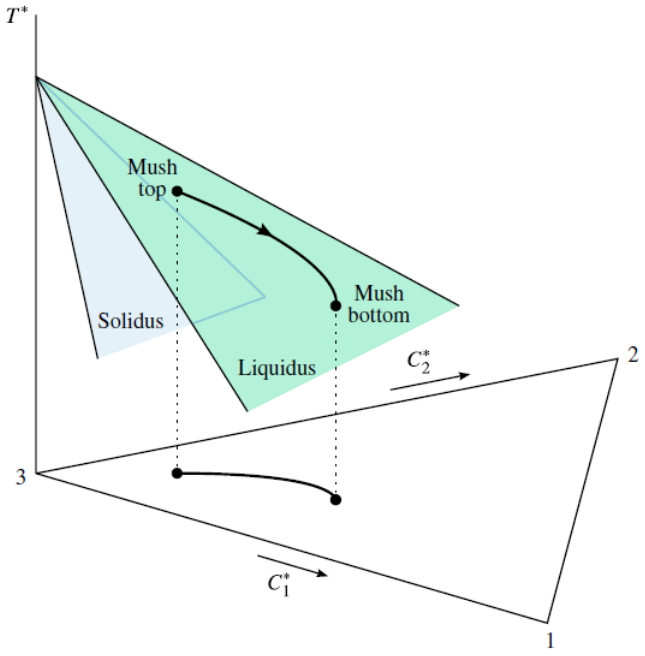

Figure 18: A schematic of ternary phase diagram for primary mush from [19]. The liquidus surface and the solidus surface associated with the corner 3 are depicted. A typical solidification path and its projection onto the Gibbs triange are shown.

4.2 Primary solidification

The theoretical formulations of mathematical modelling of ternary alloy systems have been recently reviewed in [8].

In the primary mushy layer the solidification of a single alloy component 3 occurs. Equations describing the processes in the primary mush are valid in region $H_S^* < z^* < H_P^*$ as sketched in figure 19.

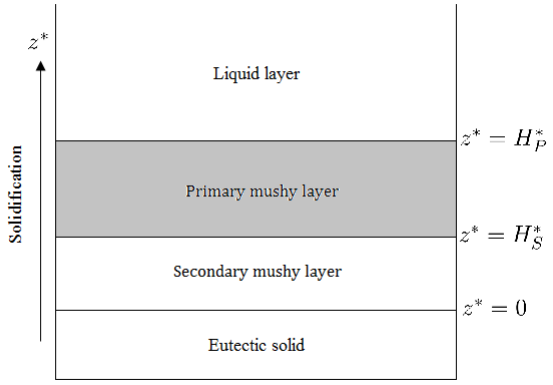

Figure 19: Sketch of the geometry for ternary solidification occurring away from cotectic lines. At the top is a semi-infinite liquid layer, underneath separated by a first planar interface is the primary mushy layer, in this layer the thermodynamical equilibrium is maintained and dendrites formed of component 3 evolve. The second interface separates the primary and the secondary mush. In the secondary mush temperature and composition are constrained to cotectic curve and crystals of cotectic concentration of components 3 and 1 are formed. The bottom layer is a eutectic solid which in which no phase transition occurs.

The mushy layer is bounded by two interfaces, moving in time at a constant speed V^* and having a constant distance H^*. We denote T^* as temperature, C_1^*, C_2^* as concentrations of two solutes, ϕ as a solid fraction, p^* as pressure and $\boldsymbol{u^*}$ as Darcy velocity. Governing equations in this coordinate system are

$$\bar{c}^*(\phi)\left(\frac{\partial T^*}{\partial t^*} - V^*\frac{\partial T^*}{\partial z^*} + \boldsymbol{u^*}\cdot\boldsymbol{\nabla^*}T^*\right) = \boldsymbol{\nabla^*}\cdot\left(\bar{k}^*(\phi)\,\boldsymbol{\nabla^*}T^*\right) + L_v^*\left(\frac{\partial \phi}{\partial t^*} - V^*\frac{\partial \phi}{\partial z^*}\right), \tag{4.2a}$$

$$(1-\phi)\left(\frac{\partial C_j^*}{\partial t^*} - V\frac{\partial C_j^*}{\partial z^*}\right) + \boldsymbol{u^*}\cdot\boldsymbol{\nabla^*}C_j^* = \boldsymbol{\nabla^*}\cdot\left(D_j^*(1-\phi)\,\boldsymbol{\nabla^*}C_j^*\right) + (1-k_j)\,C_j^*\left(\frac{\partial \phi}{\partial t^*} - V^*\frac{\partial \phi}{\partial z^*}\right),$$

$$\text{for } j = 1, 2, \tag{4.2b}$$

$$T^* = T_M^* + m_1^* C_1^* + m_2^* C_2^*, \tag{4.2c}$$

$$\boldsymbol{u^*} = -\frac{\Pi^*(\phi)}{\mu^*}\left(\boldsymbol{\nabla^*}p^* + \rho^* g^* \hat{\boldsymbol{k}}\right), \tag{4.2d}$$

$$\boldsymbol{\nabla^*}\cdot\boldsymbol{u^*} = 0. \tag{4.2e}$$

where $\bar{c}^*(\phi) = c_s^*\phi + (1-\phi)\,c_l^*$ is the effective specific heat of the mushy layer with c_s^* and c_l^* being the constant specific heat in the solid and liquid phases; $\bar{k}^*(\phi) = k_s^*\phi + (1-\phi)\,k_l^*$ is the effective thermal conductivity with k_l^* and k_s^* being thermal conductivity of liquid and solid phase respectively; L_v^* is the latent heat; D_j^* is constant

solutal diffusivity in the liquid for species j (diffusion of solute in the solid is neglected); k_j are segregation coefficients and m_j^* are liquidus slopes; $\Pi^*(\phi)$ is the permeability of mushy layer; T_M^* represents melting temperature of pure 3-rd component; μ^* is dynamic viscosity; g^* is gravity acceleration; ρ^* is fluid density.

During this process thermodynamic equilibrium in alloy is maintained, by the liquidus constraint (4.2c). A motion of interdendritic fluid is modeled via Darcy's porous media equation (4.2d). Permeability of media is function only of ϕ – fraction of fluid in particular volume, however this fraction varies across mushy layer. In work [7] for simple model with analytical solution constant permeability $\Pi^*(\phi) = 1$ was considered; more generally was permeability considered in [19] as a Taylor expansion of $\Pi^*(\phi) = \Pi_0^*(1-\phi)^{-p}$. Equations governing concentration (4.2b) are reflecting effects of solute segregation via terms $(1-k_j)\,C_j^*\left(\frac{\partial\phi}{\partial t^*} - V^*\frac{\partial\phi}{\partial z^*}\right)$.

The fluid density is assumed to satisfy

$$\rho^* = \rho_0^*\left[1 - \alpha^*(T^* - T_M^*) - \alpha_1^* C_1^* - \alpha_2^* C_2^*\right], \tag{4.3}$$

where α^* and α_j^* $(j = 1, 2)$ are thermal and solutal expansion coefficients and ρ_0^* is the density of 3-rd component at its melting temperature T_M^*.

5 Steady non-convecting states in ternary alloy solidification

Reduction to a single primary mush requires the specification of alternative boundary conditions. We will analyse 4 sets of boundary conditions (BCs):

$$\begin{aligned}
\text{C–C}: &\quad C_j^* = C_{jtop}^*, \phi = \phi_0 \text{ at } z^* = H^*; \quad C_j = C_{jbot}^* \text{ at } z^* = 0,\\
\text{F–C}: &\quad C_j^* = C_{jtop}^*, \phi = \phi_0 \text{ at } z^* = H^*; \quad \frac{\partial C_j^*}{\partial z^*} = G_{jbot}^* \text{ at } z^* = 0,\\
\text{C–F}: &\quad \frac{\partial C_j^*}{\partial z^*} = G_{jtop}^*, \phi = \phi_0 \text{ at } z^* = H^*; \quad C_j^* = C_{jbot}^* \text{ at } z^* = 0,\\
\text{F–F}: &\quad \frac{\partial C_j^*}{\partial z^*} = G_{jtop}^*, \phi = \phi_0 \text{ at } z^* = H^*; \quad C_j^* = C_{jbot}^*, \frac{\partial C_j^*}{\partial z^*} = G_{jbot}^* \text{ at } z^* = 0,
\end{aligned}$$

for $j = 1, 2$.

5.1 Non-dimensionalisation

For all boundary condition types (C–C, F–C, C–F, F–F) we obtain the same system of dimensionless governing equations. The mentiond cases differ by definitions of dimensionless parameters and the boundary conditions. We will employ non-dimensionalisation as in [7] in which lengths will be scaled by factor H^* – height of mushy layer, time scaled by H^{*2}/κ_l^*, where $\kappa_l^* = k_l^*/c_l^*$ is thermal diffusivity and velocity by κ_l^*/H^*. We define dimensionless pressure as:

$$p = \frac{\Pi_0^*}{\kappa_l^* \mu^*} \left(p^* + \rho_{top}^* g^* z^* \right). \tag{5.1}$$

Then governing equations have the form:

$$\bar{c}\left(\phi\right)\left(\frac{\partial T}{\partial t} - V\frac{\partial T}{\partial z} + \boldsymbol{u}\cdot\boldsymbol{\nabla}T\right) = \boldsymbol{\nabla}\cdot\left(\bar{k}\left(\phi\right)\boldsymbol{\nabla}T\right) + S\left(\frac{\partial \phi}{\partial t} - V\frac{\partial \phi}{\partial z}\right), \tag{5.2a}$$

$$\left(1-\phi\right)\left(\frac{\partial C_j}{\partial t} - V\frac{\partial C_j}{\partial z}\right) + \boldsymbol{u}\cdot\boldsymbol{\nabla}C_j = Le_j\boldsymbol{\nabla}\cdot\left[\left(1-\phi\right)\boldsymbol{\nabla}C_j\right] + \left(1-k_j\right)C_j\left(\frac{\partial \phi}{\partial t} - V\frac{\partial \phi}{\partial z}\right), \quad \text{for } j = 1, 2, \tag{5.2b}$$

$$T = m_1 C_1 + m_2 C_2, \tag{5.2c}$$

$$\boldsymbol{u} = -\Pi\left(\phi\right)\left(\boldsymbol{\nabla}p + \Delta\rho\hat{\boldsymbol{k}}\right), \tag{5.2d}$$

$$\boldsymbol{\nabla}\cdot\boldsymbol{u} = 0, \tag{5.2e}$$

where $\bar{c}(\phi) = (c_s^*/c_l^*)\,\phi + 1 - \phi$, $\bar{k}(\phi) = (k_s^*/k_l^*)\,\phi + 1 - \phi$, $\Pi(\phi) = \Pi^*(\phi)/\Pi_0^*$ and $\Delta\rho$ connects density of fluid with temperature and concentration fields

$$\Delta\rho = -RaT - Ra_1 C_1 - Ra_2 C_2. \tag{5.3}$$

Due to linear liquidus constraint we can quantify the buoyant effects through the two effective Rayleigh numbers $Ra_T = Ra + \frac{1}{m_2} Ra_2$ and $Ra_C = Ra_1 - \frac{m_1}{m_2} Ra_2$. Note a coupling $Ra_T + Ra_C = Ra + Ra_1 + Ra_2$.

In the following section we will discuss the effect of type of boundary conditions on definition of dimensionless parameters. Four different cases of concentration boundary conditions are presented. These combine fixed concentrations and fixed solutal fluxes denoted by C and F respectively:

5.1.1 Boundary conditions: Type C–C

Boundary conditions as in [7] and [22]:

$$T^* = T^*_{top},\ C_1^* = C^*_{1top},\ C_2^* = C^*_{2top},\ \phi = \phi_0,\ \boldsymbol{u^*} \cdot \hat{\boldsymbol{k}} = 0 \text{ at } z^* = H^*,$$

$$T^* = T^*_{bot},\ C_1^* = C^*_{1bot},\ C_2^* = C^*_{2bot},\ \boldsymbol{u^*} \cdot \hat{\boldsymbol{k}} = 0 \text{ at } z^* = 0^*.$$

Choice of such conditions, by liquidus constraint (4.2c) implies two couplings:

$$T^*_{top} = T^*_M + m_1^* C^*_{1top} + m_2^* C^*_{2top}, \quad T^*_{bot} = T^*_M + m_1^* C^*_{1bot} + m_2^* C^*_{2bot}.$$

We define non-dimensional temperature and concentrations as follows

$$T = \frac{T^* - T^*_M}{T^*_{top} - T^*_{bot}}, \quad C_j = \frac{C_j^*}{C^*_{jtop} - C^*_{jbot}}. \tag{5.4}$$

We can observe that $T^*_M = T^*_{top} - m_1^* C^*_{1top} - m_2^* C^*_{2top}$ and that the liquidus slopes m_1^*, m_2^* are negative. Therefore $T^*_M > T^*_{top}$ and non-dimesional temperature $T < 0$.
A set of dimensionless parameters is

$$V = \frac{V^* H^*}{\kappa_l^*}, \quad S = \frac{L_v^*}{c_l^* \left(T^*_{top} - T^*_{bot}\right)}, \quad Le_j = \frac{\kappa_l^*}{D_j^*},$$
$$Ra = \frac{\alpha^* \left(T^*_{top} - T^*_{bot}\right) g^* \Pi_0^* H^*}{\kappa_l^* \mu^*}, \quad Ra_j = \frac{\alpha_j^* \left(C^*_{jtop} - C^*_{jbot}\right) g^* \Pi_0^* H^*}{\kappa_l^* \mu^*}, \quad m_j = \frac{m_j^* \left(C^*_{jtop} - C^*_{jbot}\right)}{\left(T^*_{top} - T^*_{bot}\right)}.$$

Previous definitions lead to the dimensionless boundary conditions

$$T = T_{bot} + 1,\ C_1 = C_{1bot} + 1,\ C_2 = C_{2bot} + 1,\ \phi = \phi_0,\ \boldsymbol{u} \cdot \hat{\boldsymbol{k}} = 0 \text{ at } z = 1$$

$$\text{and } T = T_{bot},\, C_1 = C_{1bot},\, C_2 = C_{2bot},\, \boldsymbol{u}\cdot\hat{\boldsymbol{k}} = 0 \text{ at } z = 0$$

and the coupling $T_{bot} = m_1 C_{1bot} + m_2 C_{2bot}$, where $C_{jbot} = \frac{C^*_{jbot}}{C^*_{jtop} - C^*_{jbot}}$, $C_{jtop} = \frac{C^*_{jtop}}{C^*_{jtop} - C^*_{jbot}}$ and $T_{bot} = \frac{T^*_{bot} - T^*_M}{T^*_{top} - T^*_{bot}}$. Note that $T_{bot} \in (-\infty; -1)$.

5.1.2 Boundary conditions: Type F–C

Boundary conditions:

$$T^* = T^*_{top},\, C^*_1 = C^*_{1top},\, C^*_2 = C^*_{2top},\, \phi = \phi_0,\, \boldsymbol{u^*}\cdot\hat{\boldsymbol{k}} = 0 \text{ at } z^* = H^*,$$

$$\frac{\partial C^*_1}{\partial z^*} = G^*_{1bot},\, \frac{\partial C^*_2}{\partial z^*} = G^*_{2bot},\, \boldsymbol{u^*}\cdot\hat{\boldsymbol{k}} = 0 \text{ at } z^* = 0^*,$$

with restriction on the gradients $m^*_1 G^*_{1bot} + m^*_2 G^*_{2bot} > 0$. This choice of BC's implies a coupling:

$$T^*_{top} = T^*_M + m^*_1 C^*_{1top} + m^*_2 C^*_{2top}.$$

We define dimensionless temperature and concentrations as

$$T = \frac{T^* - T^*_M}{\left(m^*_1 G^*_{1bot} + m^*_2 G^*_{2bot}\right) H^*},\, C_j = \frac{C^*_j}{G^*_{jbot} H^*}, \tag{5.5}$$

where T exhibits only negative values, but C_j exhibits same sign as prescribed value of G^*_{jbot}. A set of dimensionless parameters:

$$V = \frac{V^* H^*}{\kappa^*_l}, \quad S = \frac{L^*_v}{c^*_l \left(m^*_1 G^*_{1bot} + m^*_2 G^*_{2bot}\right) H^*}, \quad Le_j = \frac{\kappa^*_l}{D^*_j}, \tag{5.6}$$

$$Ra = \frac{\alpha^* \left(m^*_1 G^*_{1bot} + m^*_2 G^*_{2bot}\right) g^* \Pi^*_0 H^{*2}}{\kappa^*_l \mu^*}, \quad Ra_j = \frac{\alpha^*_j G^*_{jbot} g^* \Pi^*_0 H^{*2}}{\kappa^*_l \mu^*}, \quad m_j = \frac{m^*_j G^*_{jbot}}{m^*_1 G^*_{1bot} + m^*_2 G^*_{2bot}}. \tag{5.7}$$

Dimensionless boundary conditions are

$$T = T_{top},\, C_1 = C_{1top},\, C_2 = C_{2top},\, \phi = \phi_0,\, \boldsymbol{u}\cdot\hat{\boldsymbol{k}} = 0 \text{ at } z = 1$$

$$\text{and } \frac{\partial C_1}{\partial z} = 1,\, \frac{\partial C_2}{\partial z} = 1,\, \boldsymbol{u}\cdot\hat{\boldsymbol{k}} = 0 \text{ at } z = 0$$

and the coupling $T_{top} = m_1 C_{1top} + m_2 C_{2top}$, where $C_{jtop} = \frac{C^*_{jtop}}{G^*_{jbot} H^*}$ and $T_{top} = \frac{T^*_{top} - T^*_M}{\left(m^*_1 G^*_{1bot} + m^*_2 G^*_{2bot}\right) H^*}$. Note that $T_{top} \in (-\infty; 0)$.

5.1.3 Boundary conditions: Type C–F

Boundary conditions:

$$\frac{\partial C_1^*}{\partial z^*} = G_{1top}^*,\ \frac{\partial C_2^*}{\partial z^*} = G_{2top}^*,\ \phi = \phi_0,\ \boldsymbol{u^*} \cdot \hat{\boldsymbol{k}} = 0 \text{ at } z^* = H^* \text{ and}$$

$$T^* = T_{bot}^*,\ C_1^* = C_{1bot}^*,\ C_2^* = C_{2bot}^*,\ \boldsymbol{u^*} \cdot \hat{\boldsymbol{k}} = 0 \text{ at } z^* = 0^*,$$

with restriction on the gradients $m_1^* G_{1top}^* + m_2^* G_{2top}^* > 0$. This choice of BC's implies a coupling:

$$T_{bot}^* = T_M^* + m_1^* C_{1bot}^* + m_2^* C_{2bot}^*.$$

We define dimensionless temperature and concentrations as

$$T = \frac{T^* - T_M^*}{\left(m_1^* G_{1top}^* + m_2^* G_{2top}^*\right) H^*},\ C_j = \frac{C_j^*}{G_{jtop}^* H^*}, \tag{5.8}$$

where T exhibits only negative values, but C_j exhibits same sign as prescribed value of G_{jtop}^*. A set of dimensionless parameters:

$$V = \frac{V^* H^*}{\kappa_l^*},\quad S = \frac{L_v^*}{c_l^* \left(m_1^* G_{1top}^* + m_2^* G_{2top}^*\right) H^*},\quad Le_j = \frac{\kappa_l^*}{D_j^*}, \tag{5.9}$$

$$Ra = \frac{\alpha^* \left(m_1^* G_{1top}^* + m_2^* G_{2top}^*\right) g^* \Pi_0^* H^{*2}}{\kappa_l^* \mu^*},\quad Ra_j = \frac{\alpha_j^* G_{jtop}^* g^* \Pi_0^* H^{*2}}{\kappa_l^* \mu^*},\quad m_j = \frac{m_j^* G_{jtop}^*}{m_1^* G_{1top}^* + m_2^* G_{2top}^*}. \tag{5.10}$$

Dimensionless boundary conditions are

$$\frac{\partial C_1}{\partial z} = 1,\ \frac{\partial C_2}{\partial z} = 1,\ \phi = \phi_0,\ \boldsymbol{u} \cdot \hat{\boldsymbol{k}} = 0 \text{ at } z = 1$$

$$\text{and } T = T_{bot},\ C_1 = C_{1bot},\ C_2 = C_{2bot},\ \boldsymbol{u} \cdot \hat{\boldsymbol{k}} = 0 \text{ at } z = 0$$

and the coupling $T_{bot} = m_1 C_{1bot} + m_2 C_{2bot}$, where $C_{jbot} = \frac{C_{jbot}^*}{G_{jtop}^* H^*}$ and $T_{bot} = \frac{T_{bot}^* - T_M^*}{\left(m_1^* G_{1top}^* + m_2^* G_{2top}^*\right) H^*}$. Note that $T_{bot} \in (-\infty; 0)$.

5.1.4 Boundary conditions: Type F–F

Boundary conditions:

$$\frac{\partial C_1^*}{\partial z^*} = G_{1top}^*,\ \frac{\partial C_2^*}{\partial z^*} = G_{2top}^*,\ \phi = \phi_0,\ \boldsymbol{u^*} \cdot \hat{\boldsymbol{k}} = 0 \text{ at } z^* = H^*$$

$$\text{and } C_1^* = C_{1bot}^*,\ C_2^* = C_{2bot}^*,\ \frac{\partial C_1^*}{\partial z^*} = G_{1bot}^*,\ \frac{\partial C_2^*}{\partial z^*} = G_{2bot}^*,\ \boldsymbol{u^*} \cdot \hat{\boldsymbol{k}} = 0 \text{ at } z^* = 0^*,$$

with restrictions on the gradients

$$m_1^* G_{1top}^* + m_2^* G_{2top}^* > 0 \text{ and } m_1^* G_{1bot}^* + m_2^* G_{2bot}^* > 0. \tag{5.11}$$

Note that overdetermined system will generate extra coupling. We define dimensionless temperature and concentrations as

$$T = \frac{T^* - T_M^*}{\left(m_1^* G_{1bot}^* + m_2^* G_{2bot}^*\right) H^*}, \; C_j = \frac{C_j^*}{G_{jbot}^* H^*}, \tag{5.12}$$

where T exhibits only negative values, but C_j exhibits same sign as prescribed value of G_{jbot}^*. A set of dimensionless parameters:

$$V = \frac{V^* H^*}{\kappa_l^*}, \quad S = \frac{L_v^*}{c_l^* \left(m_1^* G_{1bot}^* + m_2^* G_{2bot}^*\right) H^*}, \quad Le_j = \frac{\kappa_l^*}{D_j^*}, \tag{5.13}$$

$$Ra = \frac{\alpha^* \left(m_1^* G_{1bot}^* + m_2^* G_{2bot}^*\right) g^* \Pi_0^* H^{*2}}{\kappa_l^* \mu^*}, \quad Ra_j = \frac{\alpha_j^* G_{jbot}^* g^* \Pi_0^* H^{*2}}{\kappa_l^* \mu^*}, \quad m_j = \frac{m_j^* G_{jbot}^*}{m_1^* G_{1bot}^* + m_2^* G_{2bot}^*}. \tag{5.14}$$

Dimensionless boundary conditions are

$$\frac{\partial C_1}{\partial z} = G_1, \; \frac{\partial C_2}{\partial z} = G_2, \; \phi = \phi_0, \; \boldsymbol{u} \cdot \hat{\boldsymbol{k}} = 0 \text{ at } z = 1$$

$$\text{and } C_1 = C_{1bot}, \; C_2 = C_{2bot}, \; \frac{\partial C_1}{\partial z} = 1, \; \frac{\partial C_2}{\partial z} = 1, \; \boldsymbol{u} \cdot \hat{\boldsymbol{k}} = 0 \text{ at } z = 0,$$

where $G_j = \frac{G_{jtop}^*}{G_{jbot}^*}$ and $C_{jbot} = \frac{C_{jbot}^*}{G_{jbot}^* H^*}$. Moreover, substituting of m_j^* into constraints (5.11) we obtain single constraint $0 < m_1 G_1 + m_2 G_2$. Note that $T_{bot} \in (-\infty; 0)$.

5.2 Base state

We will denote a steady one-dimensional solution without convection as a base state solution. A system of equations corresponding to base state of (5.2) has the form:

$$-c(\bar{\phi}) V \frac{\mathrm{d}\bar{T}}{\mathrm{d}z} = \frac{\mathrm{d}}{\mathrm{d}z}\left[k\left(\bar{\phi}\right)\frac{\mathrm{d}\bar{T}}{\mathrm{d}z}\right] - VS\frac{\mathrm{d}\bar{\phi}}{\mathrm{d}z}, \tag{5.15a}$$

$$-V\left(1-\bar{\phi}\right)\frac{\mathrm{d}\bar{C}_j}{\mathrm{d}z} = \frac{1}{Le_j}\frac{\mathrm{d}}{\mathrm{d}z}\left[\left(1-\bar{\phi}\right)\frac{\mathrm{d}\bar{C}_j}{\mathrm{d}z}\right] - V\left(1-k_j\right)\bar{C}_j\frac{\mathrm{d}\bar{\phi}}{\mathrm{d}z}, \text{ for } j = 1, 2, \tag{5.15b}$$

$$\bar{T} = m_1 \bar{C}_1 + m_2 \bar{C}_2. \tag{5.15c}$$

The types of boundary conditions considered are:

$$\begin{aligned}
\text{C–C}: &\quad \bar{C}_j(0) = C_{jbot}, \bar{C}_j(1) = C_{jbot} + 1, \bar{\phi}(1) = \phi_0;\\
\text{F–C}: &\quad \frac{\mathrm{d}\bar{C}_j}{\mathrm{d}z}(0) = 1, \bar{C}_j(1) = C_{jtop}, \bar{\phi}(1) = \phi_0;\\
\text{C–F}: &\quad \bar{C}_j(0) = C_{jbot}, \frac{\mathrm{d}\bar{C}_j}{\mathrm{d}z}(1) = 1, \bar{\phi}(1) = \phi_0;\\
\text{F–F}: &\quad \bar{C}_j(0) = C_{jbot}{}^1, \frac{\mathrm{d}\bar{C}_j}{\mathrm{d}z}(0) = 1, \frac{\mathrm{d}\bar{C}_j}{\mathrm{d}z}(1) = G_j, \bar{\phi}(1) = \phi_0.
\end{aligned}$$

5.2.1 Numerical solutions

We compute solution of the system (5.15) as in [7] and [22] by shooting method. System (5.15) is transformed to system of first-order linear equations in variables $\bar{\phi}$, $\bar{C}_1$, $\bar{C}_2$, $\bar{Q}_1$ and $\bar{Q}_2$, where $\bar{Q}_j = \left(1-\bar{\phi}\right)\frac{\mathrm{d}\bar{C}_j}{\mathrm{d}z}$, for $j = 1, 2$:

$$\frac{\mathrm{d}\bar{\phi}}{\mathrm{d}z} = \frac{V\left[m_1 Le_1 \bar{Q}_1 + m_2 Le_2 \bar{Q}_2 - \left(c\left(\bar{\phi}\right)/k\left(\bar{\phi}\right)\right)\left(m_1\bar{Q}_1 + m_2\bar{Q}_2\right)\right]}{V\left[m_1 Le_1\left(1-k_1\right)\bar{C}_1 + m_2 Le_2\left(1-k_2\right)\bar{C}_2\right] - f}, \tag{5.16a}$$

$$\frac{\mathrm{d}\bar{Q}_1}{\mathrm{d}z} = -VLe_1\bar{Q}_1 + VLe_1\left(1-k_1\right)\bar{C}_1\frac{\mathrm{d}\bar{\phi}}{\mathrm{d}z}, \tag{5.16b}$$

$$\frac{\mathrm{d}\bar{Q}_2}{\mathrm{d}z} = -VLe_2\bar{Q}_2 + VLe_2\left(1-k_2\right)\bar{C}_2\frac{\mathrm{d}\bar{\phi}}{\mathrm{d}z}, \tag{5.16c}$$

$$\frac{\mathrm{d}\bar{C}_1}{\mathrm{d}z} = \frac{\bar{Q}_1}{1-\bar{\phi}}, \tag{5.16d}$$

$$\frac{\mathrm{d}\bar{C}_2}{\mathrm{d}z} = \frac{\bar{Q}_2}{1-\bar{\phi}}, \tag{5.16e}$$

where

$$f = -\frac{m_1\bar{Q}_1 + m_2\bar{Q}_2}{1-\bar{\phi}} + \frac{VS\left(1-\bar{\phi}\right)}{k\left(\bar{\phi}\right)} - \frac{1}{k\left(\bar{\phi}\right)}\frac{\mathrm{d}k}{\mathrm{d}\bar{\phi}}\left(m_1\bar{Q}_1 + m_2\bar{Q}_2\right).$$

For shooting from bottom, $z = 0$, transformation $z = 1 - \zeta$ was used. Depending on the boundary condition type the shooting method's setup will be:

C–C: shoot from $\bar{C}_j(1) = C_{jbot} + 1$, $\bar{\phi}(1) = \phi_0$, $\bar{Q}_j(1) = Q_{jtop}$ to solve $\bar{C}_j(0) = C_{jbot}$ for $j = 1, 2$.

F–C: shoot from $\bar{C}_j(1) = C_{jtop}$, $\bar{\phi}(1) = \phi_0$, $\bar{Q}_j(1) = Q_{jtop}$ to solve $1 - \bar{\phi}(0) - \bar{Q}_j(0) = 0$ for $j = 1, 2$.

For both BC types, values Q_{1top} and Q_{2top} are unknown quantities. Calculations were done using software Matlab. For integration of the system (5.16) we considered solvers `ode23s`, `ode45`, `ode113` and `ode23tb`. The most robust performance with respect to

non–dimensional parameters and solver settings was achieved using `ode45`. Computation of Q_{1top} and Q_{2top} is done by function `fsolve`. In figure 20 numerical solution is depicted, corresponding to the base state analysed in §5.3, with F–C type of boundary conditions applied.

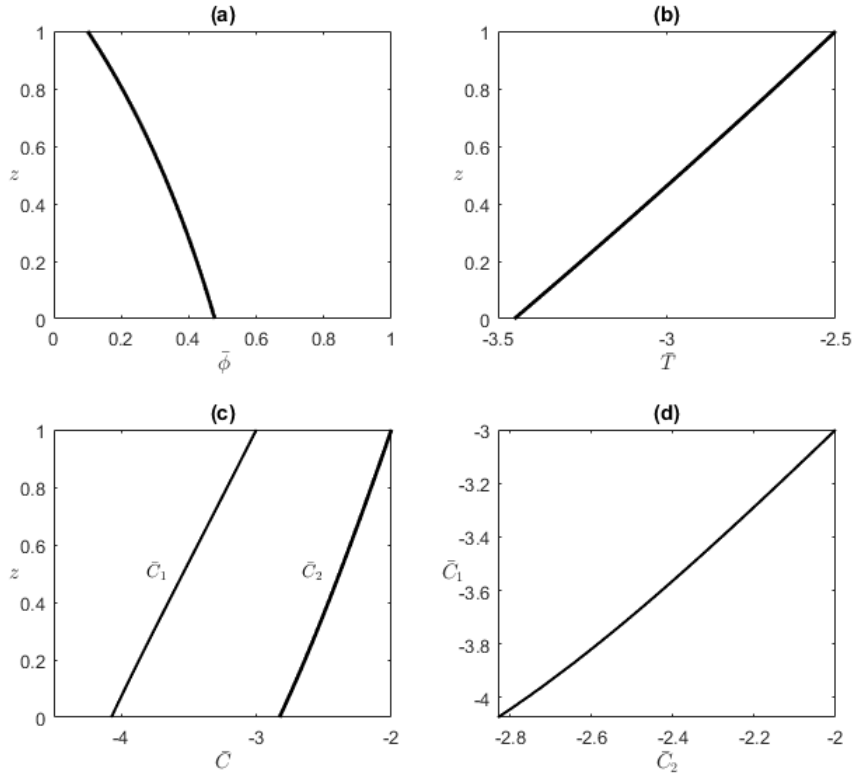

Figure 20: Plot of a numerical solution of a base state with F–C type of boundary conditions applied. Parameter values used here are $m_1 = 0.5$, $Le_1 = Le_2 = 25$, $k_1 = k_2 = 0.3$, $k_s/k_l = 1$, $c_s/c_l = 1$, $S = 0$, $V = 0.1$ and the concentration boundary conditions are $C_{1top} = -3$, $C_{2top} = -2$ and $\phi_0 = 0.1$.

5.3 Analytical solutions

In [22] we presented a number of parametric reductions allowing analytical solution of system (5.15). Here we will consider the case in which both statically–stably and statically unstably stratified concentration profiles are present, allowing further study of doubly-diffusing convection in statically–stable region presented in [7]. We will assume the same speed of solute rejection $k_1 = k_2 \equiv k$, the same Lewis number $Le_1 = Le_2 = Le$ for both solutes and zero Stefan number $S = 0$. We will also make assumption of the same material properties of the liquid and solid phases, namely thermal conductivity $k_s^* = k_l^*$ and specific heat $c_s^* = c_l^*$, resulting in $\bar{k}(\phi) = \bar{c}(\phi) = 1$. The most important features of presented solutions are finite speed of macroscopic solidification ($V \neq 0$) and presence of partial solute rejection effects ($k \neq 1$).

We will show the base state solution as a function of imposed boundary conditions (BCs).

Under mentioned reductions the base state equations (5.15) take the form:

$$-V\frac{\mathrm{d}\bar{T}}{\mathrm{d}z} = \frac{\mathrm{d}^2\bar{T}}{\mathrm{d}z^2}, \tag{5.17a}$$

$$-V\left(1-\bar{\phi}\right)\frac{\mathrm{d}\bar{C}_j}{\mathrm{d}z} = \frac{1}{Le}\frac{\mathrm{d}}{\mathrm{d}z}\left[\left(1-\bar{\phi}\right)\frac{\mathrm{d}\bar{C}_j}{\mathrm{d}z}\right] - V\left(1-k\right)\bar{C}_j\frac{\mathrm{d}\bar{\phi}}{\mathrm{d}z}, \text{ for } j = 1,2, \tag{5.17b}$$

$$\bar{T} = m_1\bar{C}_1 + m_2\bar{C}_2. \tag{5.17c}$$

Without assuming the type of BCs, we have the relationship between the solid fraction and the temperature:

$$-\frac{1}{1-\bar{\phi}}\frac{\mathrm{d}\bar{\phi}}{\mathrm{d}z} = \frac{V\left(1-Le\right)\mathrm{d}\bar{T}/\mathrm{d}z}{\mathrm{d}\bar{T}/\mathrm{d}z + VLe\left(1-k\right)\bar{T}}. \tag{5.18}$$

The solution of $\bar{T}$ depends on the choice of BCs type as follows:

$$\bar{T}(z) = \begin{cases} \frac{\delta-\mathrm{e}^{-Vz}}{1-\mathrm{e}^{-V}} & \text{C–C} \\ \frac{\delta-\mathrm{e}^{-Vz}}{V} & \text{F–C} \\ \frac{\delta-\mathrm{e}^{-Vz}}{V\mathrm{e}^{-V}} & \text{C–F} \\ \frac{\delta-\mathrm{e}^{-Vz}}{V} & \text{F–F}, \end{cases}$$

where the parameter $\delta = \frac{\mathrm{e}^{-V}\bar{T}(0)-\bar{T}(1)}{\bar{T}(1)-\bar{T}(0)}$, which depending on the type of BCs is equal to:

$$\delta = \begin{cases} 1 + T_{bot}\left(1 - \mathrm{e}^{-V}\right) & \text{C–C} \\ \mathrm{e}^{-V} + VT_{top} & \text{F–C} \\ 1 + \mathrm{e}^{-V}VT_{bot} & \text{C–F} \\ 1 + T_{bot}V & \text{F–F.} \end{cases}$$

In F–F case, controlling both gradients and concentrations at the bottom creates an overdetermined system. With the additional condition manifesting as a link between concentration gradients and solidification speed

$$V = -\ln\left(m_1 G_1 + m_2 G_2\right).$$

Physically admissible range of values for δ is $(-\infty; 1)$ in all cases, except the F–C type, when $\delta \in \left(-\infty; \mathrm{e}^{-V}\right)$.

The solid fraction satisfies

$$\frac{\mathrm{d}}{\mathrm{d}z}\ln\left(1-\bar{\phi}\right) = -\frac{1}{1-\bar{\phi}}\frac{\mathrm{d}\bar{\phi}}{\mathrm{d}z} = \frac{V\mathrm{e}^{-Vz}}{-Le(1-k)\delta/\left(Le-1\right) + \eta\mathrm{e}^{-Vz}}, \tag{5.19}$$

where the parameter $\eta = \frac{(1-k)-1/Le}{1-1/Le}$ can take both signs. As $Le \to \infty$, then $\eta \to 1-k$, which is positive. The concentrations profiles satisfy

$$\frac{\mathrm{d}^2\bar{C}_j}{\mathrm{d}z^2} + \left[\frac{\mathrm{d}}{\mathrm{d}z}\ln\left(1-\bar{\phi}\right) + LeV\right]\frac{\mathrm{d}\bar{C}_j}{\mathrm{d}z} + \left[VLe\left(1-k\right)\frac{\mathrm{d}}{\mathrm{d}z}\ln\left(1-\bar{\phi}\right)\right]\bar{C}_j = 0. \tag{5.20}$$

This equation can be transformed to a hypergeometric equation

$$\frac{\mathrm{d}^2\bar{C}_j}{\mathrm{d}\xi^2}\xi\left(1-\xi\right) + \frac{\mathrm{d}\bar{C}_j}{\mathrm{d}\xi}\left[c - \xi\left(1+a+b\right)\right] - ab\bar{C}_j = 0, \tag{5.21}$$

where $a = -1$, $b = -\frac{Le(1-k)}{\eta}$, $c = -\frac{1}{\eta}$ and

$$\xi\left(z\right) = 1 - \frac{\left(Le-1\right)\eta}{Le\left(1-k\right)\delta}\mathrm{e}^{-Vz}. \tag{5.22}$$

Note that (5.21) is a linear second-order differential equation with three regular singular points[2] $\xi = 0$, 1 and ∞ as defined in [1]. We consider the case when none of the numbers

[2]Consider equation of the form $P\left(x\right)y'' + Q\left(x\right)y' + R\left(x\right)y = 0$ and suppose that P, Q and R are polynomials, and $P\left(x_0\right) = 0$. Then x_0 is a regular singular point if $\lim_{x\to x_0}\left(x-x_0\right)\frac{Q(x)}{P(x)}$ and $\lim_{x\to x_0}\left(x-x_0\right)^2\frac{R(x)}{P(x)}$ are both finite.

c, $c-a-b$, $a-b$ is equal to the integer. Solution of equations (5.19) and (5.20), then have the form:

$$\bar{\phi}(z) = 1 - (1-\phi_0)\left(\xi(1)/\xi(z)\right)^{\frac{1}{\eta}}, \tag{5.23a}$$

$$\bar{C}_j(z) = \alpha_j w_{1(x)}(z) + \beta_j w_{2(x)}(z) \text{ for } j = 1, 2, \tag{5.23b}$$

where $w_{i(x)}$ refers to the i-th independent solution around $\xi = x$. Their form is determined by regime of ξ, defined by the values of V, Le, k and T_{bot} (or T_{top}).

For $\xi < 0$ the expansion around the regular singular point $\xi = 0$ can be used[3]

$$w_{1(0)} = {}_2F_1(a, b; c; \xi), \tag{5.24a}$$

$$w_{2(0)} = \xi^{1-c}{}_2F_1(a-c+1, b-c+1; 2-c; \xi). \tag{5.24b}$$

When $\xi \sim 1$ for all z, then the pair of independent solutions is defined as

$$w_{1(1)} = {}_2F_1(a, b; a+b+1-c; 1-\xi), \tag{5.25a}$$

$$w_{2(1)} = (1-\xi)^{c-a-b}{}_2F_1(c-b, c-a; c-a-b+1; 1-\xi). \tag{5.25b}$$

In the case of large $\xi(z)$, we have

$$w_{1(\infty)} = \xi^{-a}{}_2F_1\left(a, a-c+1; a-b+1; \xi^{-1}\right), \tag{5.26a}$$

$$w_{2(\infty)} = \xi^{-b}{}_2F_1\left(b, b-c+1; b-a+1; \xi^{-1}\right). \tag{5.26b}$$

The main building block of independent solutions of (5.21) is the hypergeometric series

$${}_2F_1(a, b; c; \xi) = \sum_{n=0}^{\infty} \frac{(a)_n (b)_n}{(c)_n} \frac{\xi^n}{n!}, \tag{5.27}$$

as defined in [1, p. 563], where $(a)_n = a(a+1)(a+2)\cdots(a+n-1)$ is the rising factorial. The rising factorial can be expressed as a ratio of Gamma functions $(a)_n = \Gamma(a+n)/\Gamma(a)$. The hypergeometric series is convergent for $|\xi| < 1$. Constants α_j and β_j (for $j = 1, 2$) can be expressed as the solutions to the system of algebraic equations depending on type of BCs. Note that the choice of BCs influences the general solution for the base state only through the parameter group δ. Applying BC of type CC, we obtain

$$\alpha_j = \frac{\frac{w_{2(x)}(1)}{w_{2(x)}(0)} C_{jbot} - (C_{jbot}+1)}{\frac{w_{2(x)}(1)}{w_{2(x)}(0)} w_{1(x)}(0) - w_{1(x)}(1)}, \; \beta_j = \frac{(C_{jbot}+1) - \frac{w_{1(x)}(1)}{w_{1(x)}(0)} C_{jbot}}{w_{2(x)}(1) - \frac{w_{1(x)}(1)}{w_{1(x)}(0)} w_{2(x)}(0)}, \tag{5.28}$$

[3]If $\xi < -1$, the hypergeometric series is not convergent and its analytical continuation along the negative real axis can be used.

for $j = 1, 2$. In FC case, we obtain

$$\alpha_j = \frac{\frac{w_{2(x)}(1)}{w'_{2(x)}(0)} - C_{jtop}}{\frac{w_{2(x)}(1)}{w'_{2(x)}(0)} - w_{1(x)}(1)}, \; \beta_j = \frac{C_{jtop} - \frac{w_{1(x)}(1)}{w'_{1(x)}(0)}}{w_{2(x)}(1) - \frac{w_{1(x)}(1)}{w'_{1(x)}(0)} w'_{2(x)}(0)}, \tag{5.29}$$

for $j = 1, 2$. The derivatives of $w_{2(x)}$ can be obtained using the formula from [1, p. 557]:

$$\frac{\mathrm{d}}{\mathrm{d}\xi} \xi^{c-1} {}_2F_1(a, b; c; \xi) = (c-1)\, \xi^{c-2} {}_2F_1(a, b; c-1; \xi). \tag{5.30}$$

The solution for $\bar{C}_j(z)$ takes the particularly simple forms when the segregation coefficient k attains some special values.

- $k = 1$, the solid fraction is increasing function of z. Closed form solution is presented in [22].
- $k = (Le - 1)/Le$, concentration profiles take a form of the extended confluent hypergeometric function, details are in [22].
- $k = 0$, qualitative characteristics of all fields remain intact, but concentration profiles can not be expressed as hypergeometric function because $c = -1$ is negative integer. Concentration profiles then take form of exponential function, details are in [22].

5.4 Asymptotic results for $Le \to \infty$

For example in binary case, the helium–water mixture has $Le \sim 23$, while the ethanol–water mixture has $Le \sim 170$.[4] Expanding (5.22) in the limit of large Le, we obtain:

$$\xi(z) = \left(1 - \frac{\mathrm{e}^{-Vz}}{\delta}\right) + \frac{\mathrm{e}^{-Vz}}{\delta(1-k)} \frac{1}{Le}, \tag{5.31}$$

where the second term cannot be omitted because the first term may became $O(1/Le)$ or smaller due to a combination of relatively small values of V, $1 - k$ and $T_{bot} \sim -1$ in C–C case or $T_{top} \sim 0$ in F–C case.

It is sufficient to consider only two cases $\xi < 0$ and $\xi > 1$, because the case $0 < \xi < 1$ corresponds to $T_{bot} > -1$. The values of V and T_{bot} (or T_{top}) define the regime of ξ and so determine the pair of independent solutions which should be used to construct solution. The summary is in table 1. Note that regime of $\xi \sim 1$ is not present within

[4]The values of mass diffusivity and thermal diffusivity are from [11], [9], respectively.

Table 1: Regimes of ξ with different pairs of independent solutions and parameter constraints in limit of large Le

Regime of ξ	Independent solutions	Type CC	Type FC
$\xi < 0$	$w_{1(0)}, w_{2(0)}$	$1 < -T_{bot} < \frac{1}{1-\mathrm{e}^{-V}}$	$\mathrm{e}^{-V} < -T_{top} < \mathrm{e}^{-V}/V$
$\xi > 1$	$w_{1(\infty)}, w_{2(\infty)}$	$\frac{1}{1-\mathrm{e}^{-V}} < -T_{bot}$	$\mathrm{e}^{-V}/V < -T_{top}$

limit of large Le only in limit $C_{1bot} \to -\infty$.

At first we will consider regime $\xi < 0$, the independent solutions are

$$w_{1(0)} = \left(1 - \frac{\mathrm{e}^{-Vz}}{\delta}\right)\left[1 - Le\,(1-k)\right], \tag{5.32a}$$

$$w_{2(0)} = \xi^{k/(1-k)}\,(1-\xi)^{Le}\,\frac{2-k}{\left(1 + Le\,(1-k)\right)^2}\left[1 + O\left(1/Le\right)\right]. \tag{5.32b}$$

The expression (5.32a) can be obtained from (5.24a) using the relation

$${}_2F_1\left(-m, b; c; \xi\right) = \sum_{n=0}^{m} \frac{(-m)_n\,(b)_n}{(c)_n}\frac{\xi^n}{n!}, \tag{5.33}$$

from [1, p. 561], where m is positive integer. Asymptotic expansion for (5.32b) can be derived using the Euler linear transformation formula from [1, p. 559]:

$${}_2F_1\left(a, b; c; \xi\right) = (1-\xi)^{(c-a-b)}\,{}_2F_1\left(c-a, c-b; c; \xi\right) \tag{5.34}$$

and then using the fact from [1, p. 565], that a real-valued hypergeometric function for fixed a, c, ξ, $(c \neq 0, -1, -2\ldots)$, $0 < |\xi| < 1$ and large $|b|$ satisfies

$${}_2F_1\left(a, b; c; \xi\right) = \left[\frac{\Gamma(c)}{\Gamma(c-a)}\,(-b\xi)^{-a} + \frac{\Gamma(c)}{\Gamma(a)}\mathrm{e}^{b\xi}\,(b\xi)^{a-c}\right]\left[1 + O\left(|b\xi|^{-1}\right)\right]. \tag{5.35}$$

Now we consider $\xi > 1$, the pair of independent solutions is

$$w_{1(\infty)} = \xi - \frac{1}{Le\,(1-k)}, \tag{5.36a}$$

$$w_{2(\infty)} = \xi^{\frac{k-2}{1-k}}\,(\xi-1)^{Le} + O(1/Le). \tag{5.36b}$$

The form (5.36a) can be obtained from (5.26a) using (5.33). The asymptotic expansion of second independent solution (5.36b) is obtained when transform (5.34) is applied to

(5.26b). Then is used asymptotic expansion for large Le defined by relation from [1, p. 565]:

$$ {}_2F_1\left(a,b;c;\xi\right)=\sum_{n=0}^{m}\frac{\left(a\right)_n\left(b\right)_n}{\left(c\right)_n}\frac{\xi^n}{n!}+O(|c|^{-m-1}), \tag{5.37} $$

where a, b, ξ are fixed and $|c|$ large. In the following sections we will use pairs (5.32a), (5.32b) and (5.36a), (5.36b) to construct asymptotic expansions for different boundary condition types.

5.4.1 C–C case

The leading-order asymptotic expansion of (5.23) for BCs (5.28) in the regime $\xi<0$, or equivalently $1<-T_{bot}<1/\left(1-\mathrm{e}^{-V}\right)$, takes the form

$$ \bar{\phi}\left(z\right)=1-\left(1-\phi_0\right)\left(\frac{\xi(z)}{\xi(1)}\right)^{\frac{-1}{1-k}}+O(1/Le), \tag{5.38a} $$

$$ \bar{C}_j\left(z\right)=\frac{\left[C_{jbot}\left(\vartheta\left(1\right)-1\right)-1\right]\bar{T}\left(z\right)+\left(T_{bot}-C_{jbot}\right)\vartheta\left(z\right)}{T_{bot}\left(\vartheta\left(1\right)-1\right)-1}+O(1/Le),\ \text{for } j=1,2, \tag{5.38b} $$

where

$$ \vartheta\left(z\right)=\left(\frac{\xi\left(z\right)}{\xi\left(0\right)}\right)^{k/(1-k)}\mathrm{e}^{-VLez}. \tag{5.39} $$

The function $\vartheta\left(z\right)$ is positive and monotonically decreasing for $z\in[0;1]$, and evaluates to $\vartheta\left(0\right)=1$ and $\vartheta\left(1\right)=O(\mathrm{e}^{-Le})$. Thus $\vartheta\left(1\right)$ is exponentially small as $Le\to\infty$. Note that the importance of the term $\left(\frac{\xi(z)}{\xi(0)}\right)^{k/(1-k)}$ grows when the term $\left(1-\frac{\mathrm{e}^{-Vz}}{\delta}\right)$ in (5.31) is not $O\left(1\right)$, otherwise $\vartheta\left(z\right)\sim\mathrm{e}^{-VLez}$. By neglecting exponentially small terms, we obtain:

$$ \bar{\phi}\left(z\right)=1-\left(1-\phi_0\right)\left(\frac{\xi(z)}{\xi(1)}\right)^{\frac{-1}{1-k}}+O(1/Le), \tag{5.40} $$

$$ \bar{C}_j\left(z\right)=\frac{C_{jbot}+1}{T_{bot}+1}\bar{T}\left(z\right)+\frac{C_{jbot}-T_{bot}}{T_{bot}+1}\vartheta\left(z\right)+O(1/Le),\ \text{for } j=1,2. \tag{5.41} $$

The formulae analogous to (5.41) in the regime $\xi>1$, or equivalently $-T_{bot}>1/\left(1-\mathrm{e}^{-V}\right)$, are

$$ \bar{C}_j\left(z\right)=C_{jbot}\frac{\xi\left(z\right)}{\xi\left(1\right)}+\vartheta\left(z\right)\left(\frac{\xi\left(z\right)}{\xi\left(0\right)}\right)^{\frac{-2}{1-k}}\left[C_{jbot}-\left(C_{jbot}+1\right)\frac{\xi\left(z\right)}{\xi\left(1\right)}\right]+O(1/Le)\ \text{for } j=1,2. \tag{5.42} $$

The formulae (5.41) and (5.42) are asymptotically equivalent if

$$\left(1-\mathrm{e}^{-V}\right)(1-k)=O(1) \text{ as } Le\to\infty.$$

The second term of (5.41) vanishes as $|C_{1bot}-C_{2bot}|$ is small, in that case the first term dictates concentration profiles to be proportional to $\bar{T}$ and hence monotonic. Therefore non-monotonicity of concentration profile can occur only when difference $|C_{1bot}-C_{2bot}|$ exceeds some threshold. This will be addressed in §5.7.

In figure 21 we compare the analytical solution with the leading-order solution (5.40). The good agreement is seen even for relatively low values of Le. Important property of (5.40) is that when $k=0$ it reduces to exact solution [22].

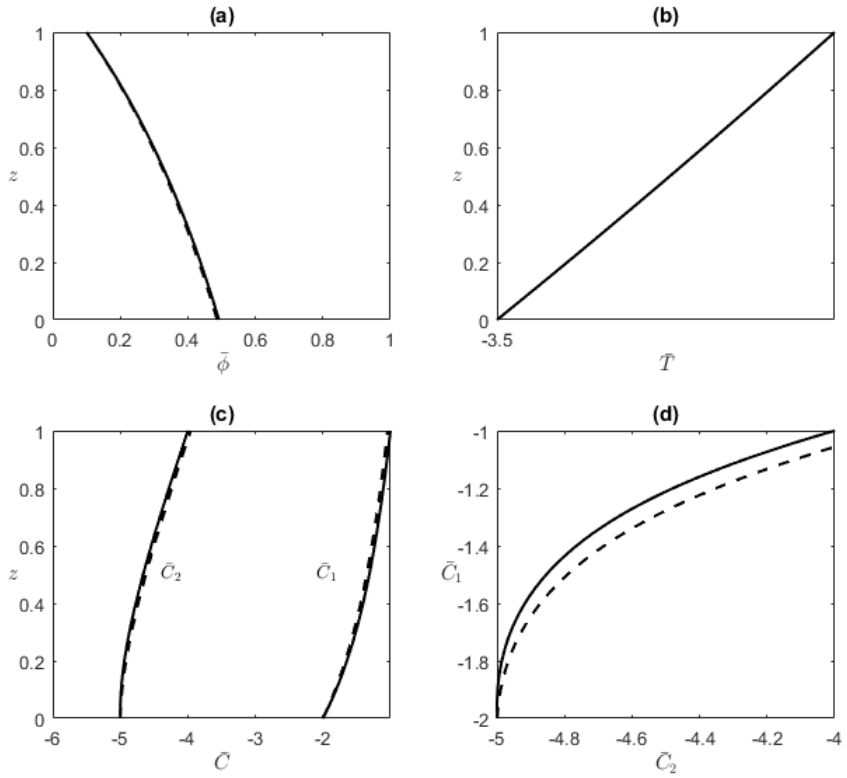

Figure 21: Comparison of the explicit solution calculated from (5.23) and (5.28) (solid) and the leading-order asymptotic solution (5.40) (dashed) in the regime of $\xi<0$. Parameter values used here are $m_1=m_2=0.5$, $Le_1=Le_2=25$, $k_1=k_2=0.3$, $k_s/k_l=1$, $c_s/c_l=1$, $S=0$, $V=0.1$. The BCs are $C_{1bot}=-2$, $C_{2bot}=-5$ and $\phi_0=0.1$.

When introducing the asymetry of BCs by employing large $|C_{1bot}|$ while C_{2bot} is

kept $O(1)$, the asymptotic expansion of (5.38) correct to $O(1/C_{1bot}^2)$ takes the form

$$\bar{\phi}(z) = \phi_0 + \frac{1}{m_1 C_{1bot}} \frac{(1-\phi_0)}{(1-k)} \frac{\mathrm{e}^{-V} - \mathrm{e}^{-Vz}}{1-\mathrm{e}^{-V}} + O(1/C_{1bot}^2), \tag{5.43a}$$

$$\bar{C}_1(z) = C_{1bot} + 1 - \mathrm{e}^{-VLez} + \frac{1}{m_1}\left[\frac{1-\mathrm{e}^{-Vz}}{1-\mathrm{e}^{-V}} - 1 + \mathrm{e}^{-VLez}\right]\frac{1}{C_{1bot}} + O(1/C_{1bot}^2), \tag{5.43b}$$

$$\bar{C}_2(z) = C_{2bot} + 1 - \mathrm{e}^{-VLez} + \left[\frac{C_{2bot}+1}{m_1}\left(\frac{1-\mathrm{e}^{-Vz}}{1-\mathrm{e}^{-V}} - 1 + \mathrm{e}^{-VLez}\right) - \frac{\mathrm{e}^{-VLez}}{m_1}\frac{k}{1-k}\frac{1-\mathrm{e}^{-Vz}}{1-\mathrm{e}^{-V}}\right]\frac{1}{C_{1bot}} + O(1/C_{1bot}^2). \tag{5.43c}$$

It can be observed, that boundary condition at $z = 0$ is satisfied exactly, while boundary condition at $z = 1$ is satisfied only up to exponentially small terms.

5.4.2 F–C case

The leading-order asymptotic expansion of (5.23) for BCs (5.29) valid for $\xi < 0$, or equivalently $\mathrm{e}^{-V} < -T_{top} < \frac{\mathrm{e}^{-V}}{V}$, has the form

$$\bar{\phi}(z) = 1 - (1-\phi_0)\left(\frac{\xi(z)}{\xi(1)}\right)^{\frac{-1}{1-k}} + O(1/Le), \tag{5.44}$$

$$\bar{C}_1(z) = \frac{\left\{\vartheta(1) + VC_{1top}\left[Le + \frac{k}{1-k}\frac{1-Le(1-k)}{Le(1-k)(\delta-1)+1}\right]\right\}\bar{T}(z) + (C_{1top} - T_{top})\,\vartheta(z)}{\vartheta(1) + VT_{top}\left[Le + \frac{k}{1-k}\frac{1-Le(1-k)}{Le(1-k)(\delta-1)+1}\right]}\left[1 + O(1/Le)\right] \tag{5.45}$$

for $j = 1, 2$. This can be further simplified by omitting the exponentially small terms yielding

$$\bar{\phi}(z) = 1 - (1-\phi_0)\left(\frac{\xi(z)}{\xi(1)}\right)^{\frac{-1}{1-k}} + O(1/Le), \tag{5.46a}$$

$$\bar{C}_j(z) = \frac{C_{1top}}{T_{top}}\bar{T}(z) + \frac{C_{jtop} - T_{top}}{T_{top}}\frac{1}{V\left(Le + \frac{k}{1-k}\frac{1}{1-\delta}\right)}\vartheta(z) + O(Le^3) \text{ for } j = 1, 2. \tag{5.46b}$$

For $\xi > 1$ or equivalently $-T_{top} > \frac{\mathrm{e}^{-V}}{V}$, the analogue of (5.46b) is

$$\bar{C}_j(z) = C_{jtop}\frac{\xi(z)}{\xi(1)} + \frac{1 - \left[C_{jtop}V + \mathrm{e}^{-V}\right]\frac{Le(1-k)-1}{Le(1-k)\delta} - 1}{V\left[\frac{k-2}{1-k} + Le\right]\frac{Le(1-k)-1}{Le(1-k)\delta} - VLe}\frac{\xi(0)}{\xi(1)}\vartheta(z)\left(\frac{\xi(z)}{\xi(0)}\right)^{\frac{-2}{1-k}} + O(Le^3) \text{ for } j = 1, 2. \tag{5.47}$$

Figure 22 is a representative plot showing the validity of asymptotic expansion (5.46) for relatively low $Le = 25$.

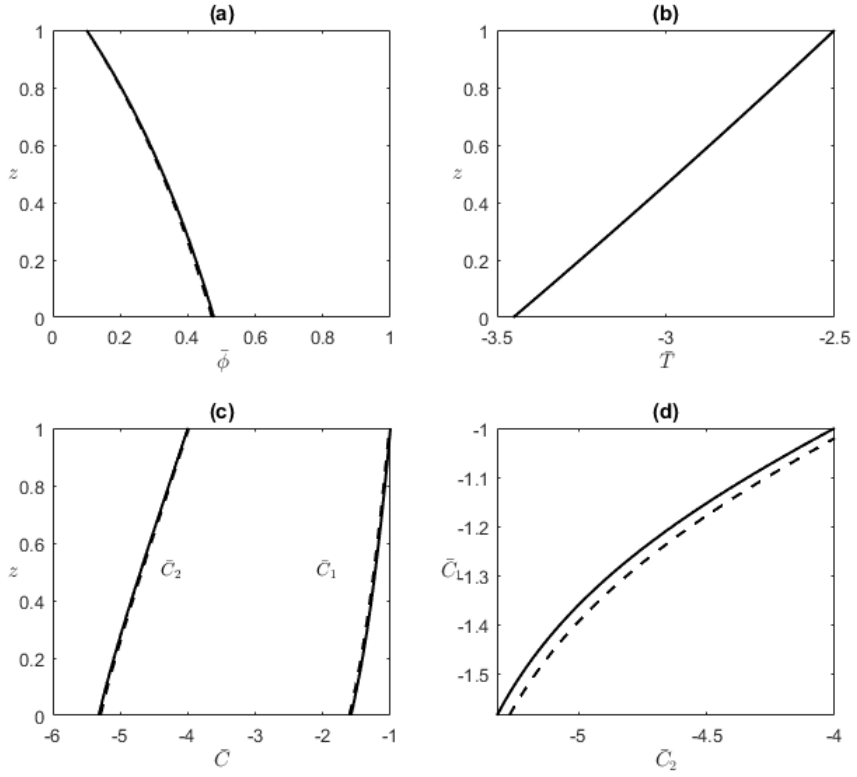

Figure 22: Comparison of the explicit solution calculated from (5.23) and (5.29) (solid) and the leading-order asymptotic solution (5.46) (dashed) in the regime of $\xi < 0$. Parameter values used here are $m_1 = m_2 = 0.5$, $Le_1 = Le_2 = 25$, $k_1 = k_2 = 0.3$, $k_s/k_l = 1$, $c_s/c_l = 1$, $S = 0$, $V = 0.1$. The BCs are $C_{1bot} = -2$, $C_{2bot} = -5$ and $\phi_0 = 0.1$.

5.5 Asymptotic results for $C_{1bot} \to -\infty$

In this section, we consider the limit $C_{1bot} \to -\infty$ with $C_{2bot} = O(1)$. By swapping the solutal indices the results for the limit $C_{2bot} \to -\infty$ with $C_{1bot} = O(1)$ can be obtained.

In [19] the limit of small solidification speeds $V \to 0$ was considered, subject to $S = \bar{S}/V^2$ and $C_{jbot} = \bar{C}_{jbot}/V^2$ with $\bar{S}$ and $\bar{C}_{jbot}$ both $O(1)$. It has been shown that in case when $Le_1 = Le_2 = Le$, single–solute–diffusive regime, the ratio of C_{1bot}/C_{2bot} plays a crucial role in determining the linear stability scenario which the system exhibits. In this limit, for relatively large Le the base state concentration profiles are qualitatively similar to our findings in this section. The main difference is in generally smaller parametric space exhibiting non-monotonic behaviour of concentration profiles.

For large values of C_{1bot}, the scaled coordinate is $\xi = 1 + O(1/C_{1bot})$, therefore we will employ two independent solutions (5.25a) and (5.25b) around regular singular

point $\xi = 1$ of (5.21). Asymptotic expansion of (5.25a) and (5.25b) in the limit of large $|C_{1bot}|$ correct to $O(1/C_{1bot}^2)$ takes the form

$$w_{1(1)}(z) = 1 - \frac{\mathrm{e}^{-Vz}}{\delta} = 1 - \frac{\mathrm{e}^{-Vz}}{m_1 C_{1bot}(1-\mathrm{e}^{-V})} + O(C_{1bot}^{-2}), \tag{5.48a}$$

$$w_{2(1)}(z) = \mathrm{e}^{-VLez}\left[1 - \frac{Le-1}{Le+1}\frac{k}{1-k}\frac{\mathrm{e}^{-Vz}}{1-\mathrm{e}^{-V}}\frac{1}{m_1 C_{1bot}} + O(C_{1bot}^{-2})\right]. \tag{5.48b}$$

where formulae (5.48a) and (5.48b) were obtained using (5.33) and series of hypergeometric function around zero ${}_2F_1(a,b,c,z) = 1 + \frac{abz}{c} + O(z^2)$ respectively.

For $\phi(z)$, $\bar{C}_1(z)$ and $\bar{C}_2(z)$ we have

$$\bar{\phi}(z) = \phi_0 + \frac{1}{m_1 C_{1bot}}\frac{(1-\phi_0)(Le-1)}{(1-k)\,Le}\frac{\mathrm{e}^{-V} - \mathrm{e}^{-Vz}}{1-\mathrm{e}^{-V}} + O(1/C_{1bot}^2), \tag{5.49a}$$

$$\bar{C}_1(z) = C_{1bot} - \frac{m_2}{m_1}\frac{1-\mathrm{e}^{-LeVz}}{1-\mathrm{e}^{-LeV}} + \frac{1}{m_1}\frac{1-\mathrm{e}^{-Vz}}{1-\mathrm{e}^{-V}} + O(1/C_{1bot}), \tag{5.49b}$$

$$\bar{C}_2(z) = C_{2bot} + \frac{1-\mathrm{e}^{-LeVz}}{1-\mathrm{e}^{-LeV}} + O(1/C_{1bot}). \tag{5.49c}$$

Figure 23 is a representative plot showing the validity of asymptotic expansion (5.49) even for relatively low value of $|C_{1bot}|$ and for $Le = 25$.

It is instructive to examine the behaviour of (5.49) when product $LeV = O(1)$, while $V \to 0$ and $Le \to \infty$. In leading-order, (5.49) reduces to:

$$\bar{\phi}(z) \sim \phi_0 + \frac{1}{m_1 C_{1bot}}\frac{(1-\phi_0)}{(1-k)}(z-1), \tag{5.50a}$$

$$\bar{C}_1(z) \sim C_{1bot} - \frac{m_2}{m_1}\left(1-\mathrm{e}^{-LeVz}\right) + \frac{z}{m_1}, \tag{5.50b}$$

$$\bar{C}_2(z) \sim C_{2bot} + 1 - \mathrm{e}^{-LeVz}. \tag{5.50c}$$

It can be observed that the solid fraction is constant at leading-order with the linear correction term at $O(1/C_{1bot})$. Concentration profile of solute j with smaller $|C_{jbot}|$ exhibits non-monotonic behaviour.

5.6 Monotonicity of solid fraction

The base-state solid fraction does not possess any local extrema. The physically admissible solution with $\mathrm{d}\phi/\mathrm{d}z < 0$ exists provided

$$\delta < \frac{(Le-1)\,\eta}{Le\,(1-k)\,\mathrm{e}^{Vz}}. \tag{5.51}$$

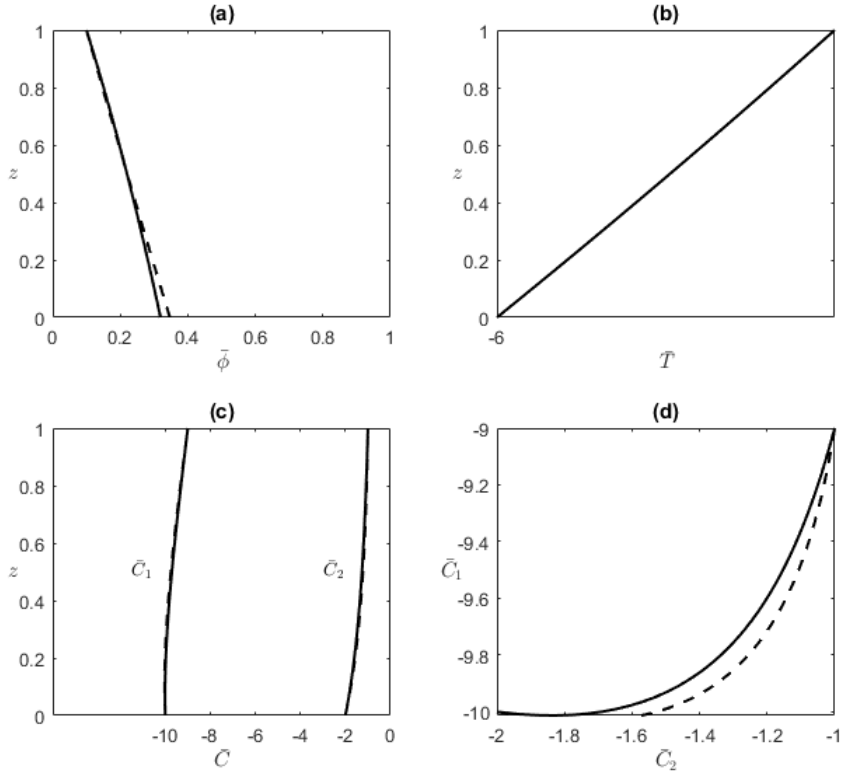

Figure 23: Comparison of explicit solution calculated from (5.23) with constants (5.28) (solid) and leading-order of asymptotic expansions (5.49a) (dashed) in the regime of $|C_{1bot}|$ large. Parameter values used here are $m_1 = m_2 = 0.5$, $Le_1 = Le_2 = 25$, $k_1 = k_2 = 0.3$, $k_s/k_l = 1$, $c_s/c_l = 1$, $S = 0$, $V = 0.1$. The BCs are $C_{1bot} = -10$, $C_{2bot} = -2$ and $\phi_0 = 0.1$.

We define point z_c at which ϕ is discontinuous and switches monotonicity:

$$z_c \equiv \frac{1}{V} \ln \left(\frac{Le\,(1-k)\,\delta}{(Le-1)\,\eta} \right).$$

If $\eta > 0$ we have three different scenarios:

(a) If $z_c > 1$ then $\bar{\phi}$ is decreasing.

(b) If $z_c \in [0; 1]$ then solution exhibits discontinuity at point z_c.

(c) z_c is not well defined or negative $\bar{\phi}$ is increasing.

In following section we illustrate this phenomena with the C–C boundary condition applied.

5.6.1 C–C case

Qualitatively representative behaviour of $\bar{\phi}$ in C–C case is depicted on the figure 24. In C–C case monotonicity of solid fraction is established when:

$$m_1 C_{1bot} + m_2 C_{2bot} < -\frac{1 + max\{Le\,(1-k)\,, 1\}\left(\mathrm{e}^V - 1\right)}{Le\,(1-k)\,(\mathrm{e}^V - 1)}. \tag{5.52}$$

The leading order of the expansion as $V \to 0$ reduces expression (5.52) to:

$$m_1 C_{1bot} + m_2 C_{2bot} < \begin{cases} -1 - \frac{1}{VLe(1-k)} & Le\,(1-k) > 1 \\ -\frac{1}{VLe(1-k)} & Le\,(1-k) < 1. \end{cases}$$

The main importance of these bounds is the identification of parameter regions, in which the base state solution is physically meaningful and the use of the model is appropriate. Generally the effects of single parameter on the size of appropriate parameter region can be characterized as follows:

- Increase in Le increases the area of well defined region.
- Increase in V increases the area of well defined region.
- Decrease in k increases the area of well defined region.
- Change in m_1 accounts for change of slope of region boundary.

5.7 Parametric dependence of region of static stability

The base state is statically stable stratified if density of fluid is decreasing function of z, therefore non-monotonic behaviour of concentration profile can induce statically unstable situation.

In C–C case the non-monotonic behaviour of concentration profiles is a function of BCs: C_{1bot} and C_{2bot}. Following calculations present extension of [22] allowing us to evaluate effect of non-zero segregation coefficient k. When considered BCs of type C–C in the limit $Le \to \infty$, using the asymptotic expansion formula (5.38) for the base state solution of $\bar{C}_1$ presented in §5.4.1 we have computed the boundaries of area within which both concentration profiles are monotone. Boundaries are determined using equations $\left.\frac{\mathrm{d}\bar{C}_j}{\mathrm{d}z}\right|_{z=0} = 0$ for $j = 1, 2$. This approach gives us two implicit functions

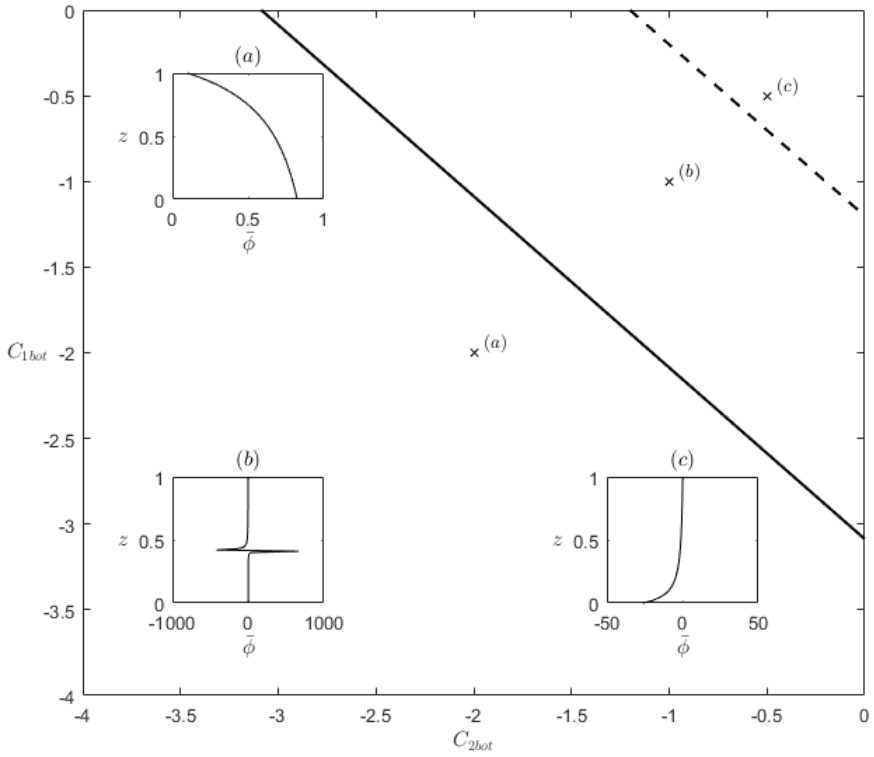

Figure 24: This plot shows three representative base state profiles of $\bar{\phi}$, in each of the three regions of C_{1bot} vs. C_{2bot} plane. By $\times$ is denoted position in C_{1bot}-versus-C_{2bot} plane in which they occur. The case with C–C type BCs is plotted. Parameter values used are $Le_1 = Le_2 = 25$, $k_1 = k_2 = 0.3$, $V = 0.1$, $m_1 = 0.5$, $\phi_0 = 0.1$ with values C_{1bot} and C_{2bot} as shown. In the region marked by (a) base state profile is well defined and decreasing function of z. In the regions marked by (b) and (c) base state is not defined due to negative values of $\bar{\phi}$.

of concentration BCs C_{1bot}, C_{2bot} defined by:

$$C_{1bot} = \frac{T_{bot}\Omega - 1}{1 + \Omega}, \quad C_{2bot} = \frac{T_{bot}\Omega - 1}{1 + \Omega}, \tag{5.53}$$

where $\Omega := \left(1 - \mathrm{e}^{-V}\right)\left[\frac{k(Le - 1/(1-k))}{Le(1-k)T_{bot}(1-\mathrm{e}^{-V})+1} - Le\right]$. By closer inspection of (5.53), we can see that it defines quadratic expression in variables C_{1bot} and C_{2bot}.

In figure 25, three qualitatively different scenarios are depicted:

(a) profile of $\bar{C}_2$ is non-monotonic; (b) both concentration profiles are monotonic and (c) profile of $\bar{C}_1$ is non-monotonic.

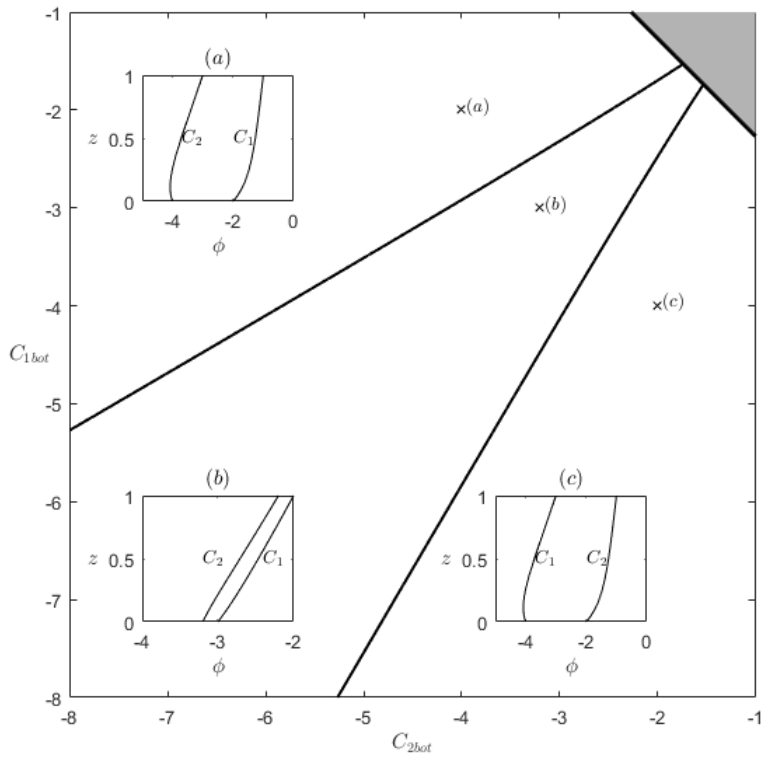

Figure 25: This plot shows classification of qualitatively different compositional profiles in dependence on concentration BC in the C_{2bot}-versus-C_{1bot} plane. Lines along which the profiles change their monotonic behaviour were determined using asymptotic result (5.53). In the grey region at the top right corner the model is not physically meaningful. Three qualitatively different scenarios are depicted with BC as shown. Parameters used were $Le = 50$, $k = 0.7$, $V = 0.1$, $\phi_0 = 0.1$ and $m_1 = 0.5$.

5.7.1 Limiting case $Le \to \infty$, $V \to 0$

We consider a limit of small pulling speeds V and large Lewis numbers defined by $Le = \frac{\bar{Le}}{V}$ with $\bar{Le} = O(1)$ as $V \to 0$. The assumption $1 - k = O(1)$ remains intact. Under these assumptions implicit curves (5.53) in variables C_{1bot} and C_{2bot}, can be transformed into the form:

$$C_{jbot}\left(T_{bot}\left(Le-1\right)+1-\frac{1}{Le\left(1-k\right)}\right)-\left(T_{bot}^2+2T_{bot}+\frac{1}{Le\left(1-k\right)}\right)=0 \text{ for } j=1,2. \tag{5.54}$$

Case when segregation coefficients are zero i.e. $(1 - k) = 1$ causing curves of monotonicity to be linear, was studied in [22]. Mentioned results can be obtained by setting

$k = 0$ in (5.54):

$$C_{1bot} = \frac{1 + m_2 \bar{Le} C_{2bot}}{m_2 \bar{Le} - 1}, \quad C_{1bot} = \frac{\left(m_1 \bar{Le} - 1\right) C_{2bot} - 1}{m_1 \bar{Le}}. \tag{5.55}$$

Due to the symmetry in Lewis numbers and segregation coefficients, we will consider only the branch corresponding to $\left.\frac{\mathrm{d}\bar{C_1}}{\mathrm{d}z}\right|_{z=0} = 0$. For general $k > 0$ a physically valid root of (5.54) is

$$C_{1bot} = \frac{1 - (1-k)\,\bar{Le}\left[M - m_2 C_{2bot}\left(1 - \bar{Le} M\right)\right] - \sqrt{1 - (1-k)\,\bar{Le} Q\left(m_2 C_{2bot}\right)}}{2\bar{Le}\,(1-k)\,m_1\left(m_2 \bar{Le} - 1\right)}, \tag{5.56}$$

where quadratic term is defined as

$$Q(x) = -(1-k)\,\bar{Le}\left(\bar{Le} - 1\right)^2 x^2 - 2\left\{1 + \bar{Le}\left[\left(\bar{Le} - 2\right)(1-k) - kM\right]\right\} x + 2 - \bar{Le}\left(1 - kM^2\right), \tag{5.57}$$

with $M = m_2 - m_1$. By computing oblique asymptote to $C_{1bot}(C_{2bot})$ in case when $C_{2bot} \to -\infty$ we have:

$$C_{1bot} = \frac{1 + m_2 \bar{Le} C_{2bot}}{m_2 \bar{Le} - 1} + \frac{k}{(1-k)\left(\bar{Le} - 1\right)\left(m_2 \bar{Le} - 1\right)}, \tag{5.58}$$

where the first term represents curve of monotonicity switch obtained with $k = 0$ and the second term represents a correction when $k > 0$. Note that, as $k \to 1$ approaches 1, the region of monotonicity increasingly changes it's size, but whether it is increases or decreases depends on a sign of $m_2 \bar{Le} - 1$. In figure 26 can be observed the effect of non-zero segregation coefficients on the monotonicity of concentration profiles. When Le is relatively low, sensitivity to change in segregation coefficient is significant. As $Le \to \infty$ effects of non-zero segregation coefficients diminish.

5.7.2 Position of local extrema

When function $\vartheta(z) \sim \mathrm{e}^{-VLez}$, position of the local extreme of the concentration profile can be computed using (5.40) and (5.46) for C–C and F–C boundary condition types respectively

$$z_{\mathrm{CC}} = \frac{1}{V\,(Le - 1)} \ln\left[\frac{C_{jbot} - T_{bot}}{C_{jbot} + 1} Le\left(1 - \mathrm{e}^{-V}\right)\right], \tag{5.59}$$

$$z_{\mathrm{FC}} = \frac{1}{V\,(Le - 1)} \ln\left[\frac{C_{jtop} - T_{top}}{C_{jtop}} \frac{Le\,(1-\delta)}{Le\,(1-\delta) + k/1 - k}\right]. \tag{5.60}$$

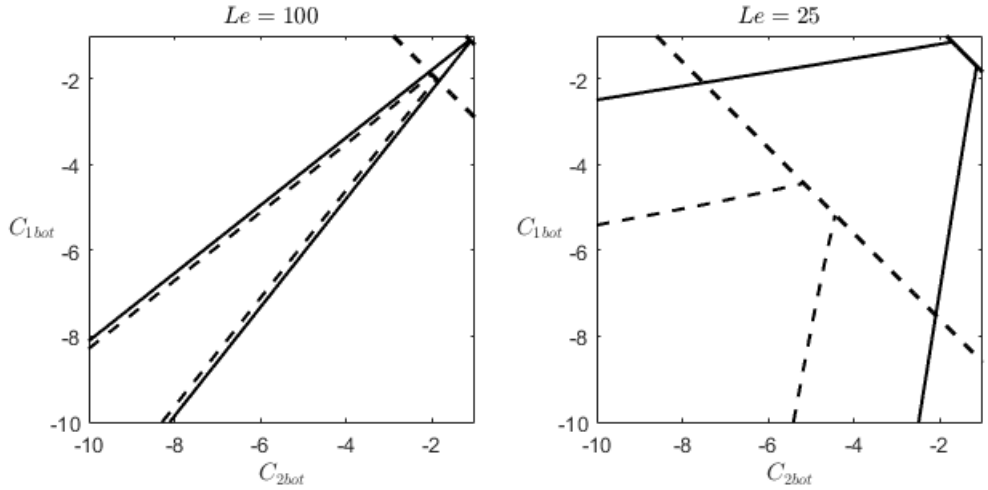

Figure 26: Plot depicting a shape of statically stable region for different values of Le and k. The solid line corresponds to $k = 0.1$ and dashed line corresponds to $k = 0.9$. Used values of other parameters are $V = 0.1$, $m_1 = 0.5$, $\phi_0 = 0.1$.

When $C_{1bot} \to \infty$ is considered the local extreme of the concentration profile computed from (5.49):

$$z_{\mathrm{CC}} = \frac{1}{V\,(Le-1)} \ln\left[m_2 Le \frac{\left(1-\mathrm{e}^{-V}\right)}{\left(1-\mathrm{e}^{-LeV}\right)} \right], \tag{5.61}$$

is the same as the one from limit $C_{1bot} \to \infty$ of expression (5.59). This representation defines parametric combination of Le, V and m_2 for which both concentration profiles are monotonic independent of the choice of BCs:

$$m_2 Le \left(1-\mathrm{e}^{-V}\right) \lesssim 1, \tag{5.62}$$

which holds for all values of k satisfying $1-k = O(1)$. Figure 27 shows parameter space Le–V divided into grey and white region by line $m_2 Le \left(1-\mathrm{e}^{-V}\right) = 1$. Insets in this figure show representative plots of boundary condition sets allowing non-monotonic concentration profiles, analogous to figure 26. In grey region case (a) shows a bounded set of BCs which allows non-monotonic concentration profile. Therefore when $C_{1bot} \to -\infty$ monotonic behaviour of concentration profiles is expected.

In white region case (b) shows that BCs are divided by a linear relation, as was observed only by numerical calculation in [7]. Therefore when $C_{1bot} \to -\infty$ non-monotonic behaviour of attributable concentration profile is expected.

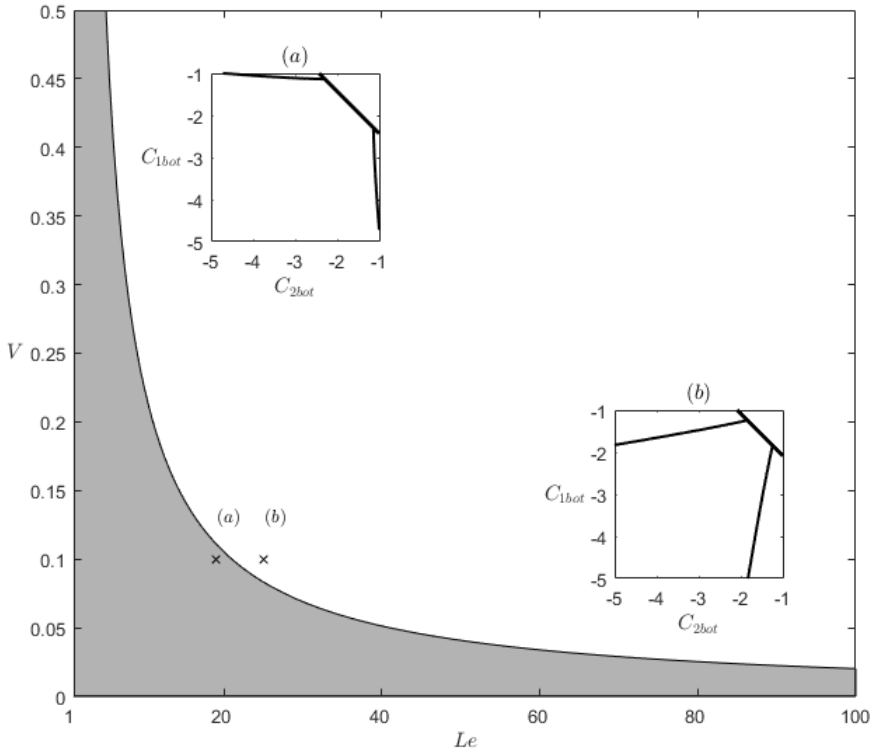

Figure 27: Plot of (5.62) in the parametric plane Le-versus-V. In the grey region both concentration profiles are always monotonic when for both solutes $C_{jbot} \to -\infty$, while in the white region there always exists boundary condition setup with both $C_{jbot} \to -\infty$ in which one of the concentration profiles is non-monotonic. Inset (a) shows case when set of BCs allowing non-monotonic concentration profile is bounded. On the inset (b) set of BCs allowing non-monotonic behaviour covers in both limiting cases $C_{1bot} \to -\infty$ while $C_{2bot} = O(1)$ and $C_{2bot} \to -\infty$ while $C_{1bot} = O(1)$. The results are shown for $m_1 = m_2 = 0.5$.

Conclusions

Explicit and asymptotic solutions are useful for identification of key aspects defining the process of solidification. In this thesis we introduce two problems involving solidification and provide explicit solutions in interesting parametric regimes. The first is the solidification of a binary alloy pulled horizontally, and the second is the solidification of a ternary alloy in vertically moving frame of reference.

In §2 we have introduced the main concepts of solidification of multicomponent solidification from continuous-mechanics perspective. The governing equations have been presented in the general frame of reference, which includes situations described in following chapters. §§3 and 5 expand the original results presented by the present author in papers [27] and [23] respectively.

In §3 we have described the solidification of a binary alloy over a horizontally moving substrate, with the most important parameters being the scaled far-field velocity $\mathcal{U}$ and the Prandtl number Pr. The results obtained can be compared to [26], where the mushy layer is absent, but the geometry of the problem is similar. The dimensional thickness of the solid phase was proportional to $U_\infty^{*1/2}/U_0^*$, provided $Pr \ll \mathcal{U}$, in contrast to the present case where the dimensional thickness is proportional to $1/U_0^{*1/2}$. This can be observed by examining the dimensional position of the mush–liquid interface in terms of U_0^* and U_∞^*, given by (3.62b) and plotted in figure 13 fora range of values of $\mathcal{U}$. An interesting feature is the non-monotonicity in the mush-liquid interface position as a function of U_0^*. Another difference from the problem without the mush is, that the effect the velocity ratio on the thermal and compositional boundary layer is, to leading order in small $\mathcal{U}$ negligible (see figure 12). In the problem without the mush thermal and compositional boundary layers ahead of the solid–liquid interface have the size of $O(\mathcal{U}^{-1/2})$. in figure 7 we show the dependence of λ_b and C_b on the non-dimensional parameters $Pr, \mathcal{U}$, Le and Γ evaluated from (3.51b) and (3.49) respectively. Notable is the independence of concentration and the mushy layer thickness on Pr, the fact that the mushy layer thickness is an increasing function of Γ and Le, and the transition of the interfacial concentration and interface position to the small diffusivity limit as $Le \to \infty$. For $\mathcal{U} = 0$, we have shown that λ_b is an increasing function of both Γ and Le. The integral relationships (3.44) and (3.65) that quantify the total amount of solute contained within the mushy region were presented. When Pr is small, the latter

one is proportional to $\mathcal{C}-1$, with the correction of $O(Pr/Le)$. The $O(Pr/Le)$ effect is weakened as the values of Γ approach unity. The dependence of growth constants λ_a and λ_b, calculated from(3.48) and (3.49) respectively, on Γ is plotted in figure 14. A comparison to [37] is done by considering the mush without horizontal pulling, calculated from (3.48) and (3.64), where $\mathcal{U}=1$. Note that in both cases there is a critical value $\Gamma=\Gamma_{min}$ for which $\lambda_a=\lambda_b$. For $\Gamma<\Gamma_{min}$ we have $\lambda_a>\lambda_b$, which is not physically admissible. In figure 15 we show Γ_{min} as a function of $\mathcal{U}$, the values of Γ_{min} are found to be increasing function of $\mathcal{U}$ and to attain their maximum values at $\mathcal{U}=1$. Thus, the horizontal pulling and the resulting flow in the liquid enhance the formation of a mushy region: when the system is pulled horizontally, the range of Γ for which the mush exists is larger than that for the system without pulling. The fact that there is a value of Γ below which the mushy region does not exist can be used, together with definition $\Gamma=\Gamma^*\Delta C^*/\Delta T^*$, to derive the bounds on C^*_∞ or T^*_∞. With ΔC^* fixed, we have an upper bound for the far-field temperature for which the mushy region exists: $T^*_\infty<T^*_L(C^*_0)+\Gamma^*\Delta C^*/\Gamma_{min}$. Analogously with ΔT^* fixed, there is an upper bound for far field concentration: $C^*_\infty<C^*_0-\Gamma_{min}\Delta T^*/\Gamma^*$. These bounds are found to be higher in the case of with horizontal pulling, than in the case without pulling, studied in [37].

The governing equations for the full model of directional solidification of ternary alloy is given in §4. The model consists of the liquid layer, primary mush and secondary mush in the frame of reference moving with constant vertical speed V^*.

In §5 we have analysed the model of solidification of primary mushy layer described in [7], [19] and [20], while considering a number of different types of boundary conditions. In this thesis we have introduced F–C, C–F and F–F types of boundary conditions, where C or F refer to the solute concentration or solutal flux fixes at the boundary. In [19], the case of small macroscopic speed of solidification V was considered. Here we have considered a finite V. We have been able to identify explicit solutions for the base state in terms of hypergeometric functions. In §5.4 we construct an asymptotic expansion of the base state solution in the limit of large Lewis number Le. The leading-order asymptotic expansions plotted in figures 21 and 22 show very good accuracy even for low values of Le. In §5.5 we considered the limit of large $|C_{1bot}|$ with C_{2bot} kept $O(1)$, causing the asymmetry in boundary conditions reflected in the

non-monotonicity of $\bar{C}_1$ profile. This result can be compared with the results in [19] where a limit of jointly large $|C_{1bot}|$ and $|C_{2bot}|$ was considered. A notable feature of the obtained expansions is that they preserve non-monotonic behaviour of concentration profiles. The non-monotonic behaviour of concentration profiles may lead to statically unstable stratification of interstitial fluid, causing the potential onset of convection originating in the layer. Depending on the solutal expansion coefficients, the results from §5.7 identify the critical curves of static stability in the parameter space of C_{1bot} vs. C_{2bot}. We show that the critical lines are in general non-linear and that in this case approach the oblique asymptote as $Le \to \infty$. In figure 25 our asymptotic results are compared to the numerical results of [7]. The grey region shows, where the model is not physically meaningful. Figure 26 shows the effect of segregation coefficients on the stability of the base state solution, noting that it is more pronounced at lower values of Le. Figure 27 reveals the existence of the parametric region in the space Le vs. V (shown grey), in which the non-monotonic concentration profiles are allowed in a bounded portion of the (C_{1bot}, C_{2bot}) plane.

References

[1] Abramowitz, M., Stegun, I. A., *Handbook of mathematical functions: with formulas, graphs, and mathematical tables*, vol. 55. (1964).

[2] Aitta, A., Huppert, H. E., Worster, M. G., *Diffusion-controlled solidification of a ternary melt from a cooled boundary*, J. Fluid Mech. **432** (2001), 201–217.

[3] Aharonov, E., Spiegelman, M., Kelemen, P., *Three-dimensional flow and reaction in porous media: Implications for the Earth's mantle and sedimentary basins*, J. Geophys. Res. Solid. Earth **102** (B7) (1997), 14821–14833.

[4] Amberg, G., Homsy, G.M., *Nonlinear analysis of buoyant convection in binary solidification with application to channel formation*, J. Fluid Mech. **252** (1993), 79–98.

[5] Anderson, D. M., *A model for diffusion-controlled solidification of ternary alloys in mushy layers*, J. Fluid Mech. **483** (2003), 165–197.

[6] Anderson, D. M., Schulze, T. P., *Linear and nonlinear convection in solidifying ternary alloys*, J. Fluid Mech. **545** (2005), 213–243.

[7] Anderson, D. M., McFadden, G. B., Coriell, S. R., Murray, B. T., *Convective instabilities during the solidification of an ideal ternary alloy in a mushy layer*, J. Fluid Mech. **647** (2010), 309–333.

[8] Anderson, D. M., Guba, P., *Convective phenomena in mushy layers*, under review.

[9] Blumm, J., Lindemann A., *Characterization of the thermophysical properties of molten polymers and liquids using the flash technique*, High Temp. High Press. **35** (36) (2003), 627–632.

[10] Carolsfeld, J., Godinho, H. P., Zaniboni Filho, E., Harvey, B.J., *Cryopreservation of sperm in Brazilian migratory fish conservation*, J. Fish Biol. **63** (2) (2003), 472–489.

[11] Cussler, E. L., *Diffusion: mass transfer in fluid systems* , (2009), Cambridge University Press.

[12] Dahle, A. K., StJohn, D. H., *Rheological behaviour of the mushy zone and its effect on the formation of casting defects during solidification*, Acta Mater. **47** (1) (1998), 31–41.

[13] Davis, S. H., *Theory of solidification*, (2001), Cambridge University Press.

[14] Fearn, D. R., *Hydromagnetic flow in planetary cores*, Rep. Prog. Phys., **61** (3) (1998), 175–235.

[15] Galdi, G. P., Payne, L. E., Proctor, M. R. E., Straughan, B., *Convection in thawing subsea permafrost*, Proc. R. Soc. Lond. A **414** (1846) (1987), 83–102.

[16] Gewecke, N. R., Schulze, T. P., *Solid–mush interface conditions for mushy layers*, J. Fluid Mech. **689** (2011), 357–375.

[17] Guba, P., Worster, M. G., *Nonlinear oscillatory convection in mushy layers*, J. Fluid Mech. **553** (2006), 419–443.

[18] Guba, P., Worster, M. G., *Interactions between steady and oscillatory convection in mushy layers*, J. Fluid Mech. **645** (2010), 411–434.

[19] Guba, P., Anderson, D. M., *Diffusive and phase change instabilities in a ternary mushy layer*, J. Fluid Mech. **760** (2014), 634–669.

[20] Guba, P., Anderson, D. M., *Pattern selection in ternary mushy layers*, J. Fluid Mech. **825** (2017), 853–886.

[21] Huppert, H. E., Worster, M. G., *Dynamic solidification of a binary melt*, Nature, **314** (6013) (1985), 703–707.

[22] Hurban, M., *Static stability of three-component systems*, Master's thesis (2015), Comenius University, Bratislava, Slovakia.

[23] Hurban, M., *Steady non-convection states in ternary alloy solidification*, under review, (2019).

[24] Krane, M. J. M., Incropera, F. P., *Solidification of ternary metal alloys-II. Prediction of convective phenomena and solidification behaviour of* Pb–Sb–Sn *alloys*, Int. J. Heat Mass Transf. **40** (16) (1997), 3837–3847.

[25] Krane, M. J. M., Incropera, F. P., Gaskell, D. R., *Solidification of ternary metal alloys-I. Model development*, Int. J. Heat Mass Transf. **40** (16) (1997), 3827–3835.

[26] Kyselica, J., Guba, P., *Forced flow and solidification over a moving substrate*, Appl. Math. Model. **40** (1) (2016), 31–40.

[27] Kyselica, J., Guba, P., Hurban, M., *Solidification and flow of a binary alloy over a moving substrate*, Transp. Porous Media, **121** (2) (2018), 419–435.

[28] Kyselica, J., Šimkanin, J., *Global conservation model for a mushy region over a moving substrate*, Phys. Earth Planet. Int., **276** (2017), 60–67.

[29] Löfgren, H. B., *Ideal solidification of a liquid-metal boundary layer flow over a conveying substrate*, J. Fluid Mech., **446** (2001), 121–131.

[30] Mullins, W., Sekerka R. F., *Stability of a planar interface during solidification of a dilute binary alloy*, J. Appl. Phys. **35** (2) (1964), 444–451.

[31] Ruddick, B., Gargett, A. E., *Oceanic double-diffusion: introduction*, Prog. Oceanogr. **56** (2003), 381–393.

[32] Schulze, T. P., Worster, M. G., *A time-dependent formulation of the mushy-zone free-boundary problem*, J. Fluid Mech. **541** (2005), 193–202.

[33] Tangthieng, C., Cheung, F. B., Shiah, S. W., *Behavior of the two-phase mushy zone during freeze coating on a continuous moving plate*, J. Heat Transfer, **124** (2002), 111-119.

[34] Thompson, A. F., Huppert, H. E., Worster, M. G., Aitta, A., *Solidification and compositional convection of a ternary alloy*, J. Fluid Mech. **497** (2003), 167–199.

[35] Turner, J. S., *Double-Diffusive Phenomena*, Annu. Rev. Fluid Mech. **6** (1) (1974), 37–54.

[36] West, D. R. E., *Ternary equilibrium diagrams*, (2012), Springer Science & Business Media.

[37] Worster, M. G., *Solidification of an alloy from a cooled boundary*, J. Fluid Mech. **167** (1986), 481–501.

[38] Worster, M. G., *The dynamics of mushy layers*, In Interactive Dynamics of Convection and Solidification (ed. S. H. Davis, H. E. Huppert, U. Muller & M. G. Worster), (1992), 113–138. Kluwer.

[39] Worster, M. G., *Convection in mushy layers*, Annu Rev Fluid Mech, **29** (1) (1997), 91–122.

Transp Porous Med
https://doi.org/10.1007/s11242-017-0971-4

Solidification and Flow of a Binary Alloy Over a Moving Substrate

J. Kyselica[1] · **P. Guba**[2,3] · **M. Hurban**[2]

Received: 9 June 2017 / Accepted: 14 November 2017

Abstract We study the solidification and flow of a binary alloy over a horizontally moving substrate. A situation in which the solid, liquid and mushy regions are separated by the stationary two-dimensional interfaces is considered. The self-similar solutions of the governing boundary layer equations are obtained, and their parametric dependence is analysed asymptotically. The effect of the boundary layer flow on the physical characteristics is determined. It is found that the horizontal pulling and the resulting flow in the liquid enhance the formation of the mushy region.

Keywords Binary-alloy solidification · Mushy region · Moving substrate · Boundary layer flow · Self-similar solutions

Mathematics Subject Classification 76M45 · 76R05 · 80A22

1 Introduction

During the solidification of multicomponent mixtures, such as water solutions or metal alloys, a two-phase, or mushy, region often forms as a result of the morphological instability of a planar phase interface (Worster 2000). During the growth of such an unstable interface, the protrusions of the solid into the liquid phase grow to form a dendritic matrix, which, when viewed from the macroscopic point of view, behaves as a reactive porous medium.

This work was supported by the Slovak Research Council (VEGA 1/0319/15 and 2/0115/16) and the Slovak Research and Development Agency (APVV–14–0378).

✉ J. Kyselica
kyselica@ig.cas.cz

1 Institute of Geophysics, The Czech Academy of Sciences, 141 31 Prague 4, Czech Republic

2 Department of Applied Mathematics and Statistics, Faculty of Mathematics, Physics and Informatics, Comenius University, 842 48 Bratislava 4, Slovakia

3 Earth Science Institute of the Slovak Academy of Sciences, 840 05 Bratislava 4, Slovakia

Published online: 23 November 2017

The local porosity of the mushy region can be space and time dependent as a result of the solidification and melting of the dendrites. Typically, the solid formed during solidification has the composition that is different from that of the original liquid, one of the components being released ahead of the solidifying interface. If the lighter component is released, convective motions usually take place within the mushy region, leading eventually to the formation of localized, narrow channels, called 'chimneys', through which cold, solute-enriched fluid flows to the liquid region ahead of the mush (Schulze and Worster 1999). As a result of chimney formation, structural defects can appear in the solidified metal alloys, an effect that is undesirable in order to produce high-quality materials (Fowler 1985). During solidification of sea ice, which also has the character of a mushy region, the brine channels, resulting from the chimney formation, have an important role in the ocean dynamics in polar regions (Worster and Jones 2015). Solidification of mushy regions is also of interest from the point of the structure of the Earth's inner core since it is believed that the boundary between the inner and the outer cores is dendritic (Deguen et al. 2007). However, the precise characteristics of the possible mushy region at the inner core boundary are still a subject of current investigation.

A model of diffusion-controlled growth of a mushy region during solidification of a binary alloy was studied by Worster (1986). The alloy solidified from the cooled bottom boundary, and the solid/mush and the mush/liquid interfaces were planar. The model was based on the local conservation of heat and solute, and the growth rates of the interfaces were controlled by the diffusive transport of solute away from the interfaces. A similar model, but with equal thermal properties of the solid and liquid phases, along with the negligible latent-heat release, was studied by Gewecke and Schulze (2011b). In the so-called directional solidification, unlike the diffusion-controlled solidification, the interfaces are stationary with respect to the laboratory frame of reference, while the solidifying system is pulled at a constant speed through a given temperature gradient (see, for example, Davis 2001).

An experimental configuration related to the continuous spin casting in material engineering (see the review by Steen and Karcher 1997) is that of a cooled, horizontal plate moving horizontally at a constant speed. The solidifying interfaces are stationary under the appropriate conditions; however, unlike in the directional solidification described above, the interfaces are not planar and there is a strong flow in the liquid phase. A steady boundary layer flow and solidification of a binary alloy over a moving substrate with a two-dimensional solid/liquid interface were analysed by Löfgren (2001) and later by Kyselica and Guba (2016). The sensitivity of the solidifying system upon the scalar far-field velocity was analysed. Tangthieng et al. (2002) and Tangthieng and Cheung (2003) considered the solidification over a horizontally pulled substrate with a mushy region divided into a packing region consisting of dendrites moving with the substrate and a dispersed region with dendrites free to move with the fluid.

In the present paper, we combine the approach used by Kyselica and Guba (2016) with that by Worster (1986) in order to formulate the problem studied by Tangthieng et al. (2002), so that the local liquid fraction is to be governed by the local solute conservation. This is in contrast to Tangthieng et al. (2002), who prescribed the relation between the local liquid fraction and temperature based on the lever rule. Moreover, unlike Tangthieng et al. (2002), we shall consider a simplified situation with the mushy region consisting only of the packing region. The main question that is to be answered is: How do the pulling of the substrate and the resulting flow influence the thickness of the mushy region? The present study provides analytical self-similar solutions to a solidification problem with non-planar interfaces and two-dimensional advection of heat and solute (see also Löfgren 2001; Kyselica and Guba 2016). We compare the results with a recent study by Kyselica and Šimkanin (2017) of the mushy region over a moving substrate based on the global solute conservation and the

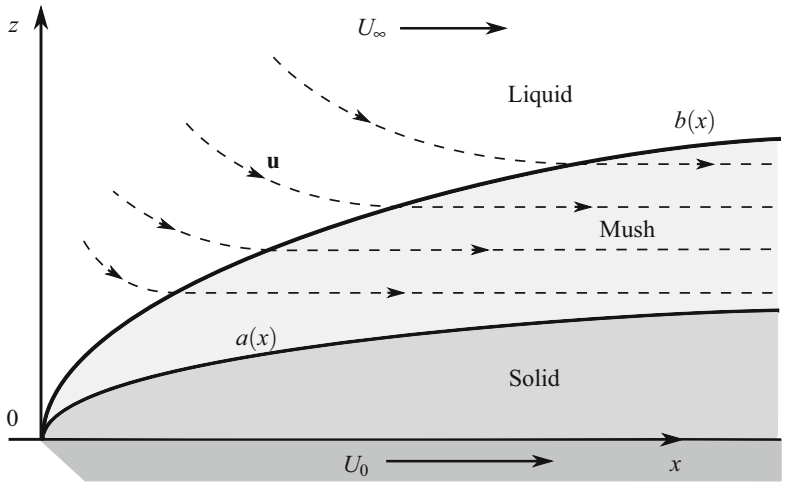

Fig. 1 A definition sketch for the problem of solidification of a binary alloy over a horizontally moving substrate. For description, see text

simplifying assumption of no solute diffusion in the liquid phase. Generally, the situations involving analytical solutions with the flow are rare. Another example is the study by Guba and Worster (2006) of a two-dimensional convection in a laterally solidifying mushy region.

The structure of the paper is as follows. In Sect. 2 we formulate the mathematical problem and derive a reduced system of governing boundary layer equations. In Sect. 3 we identify the self-similar solutions for the temperature, concentration and velocity fields in the liquid phase, for the temperature, concentration and local liquid fraction in the mushy region, and for the temperature field in the solid region. The growth constants defining the self-similar positions of the solid/mush and mush/liquid interfaces are analysed in Sect. 4 in the case when the ratio of the far-field horizontal velocity in the liquid phase to the speed of the moving substrate is finite, while the case when the velocity ratio is zero is discussed in Sect. 5. Finally, in Sect. 6 we give conclusions.

2 Mathematical Formulation

The region $x > 0$, $z > 0$ is filled with a binary alloy with far-field temperature and solute concentration T_∞ and C_∞ at $z \to \infty$, respectively. The solidification occurs at the cooled substrate $z = 0$, which moves horizontally at constant speed $U_0 > 0$, and its temperature is maintained at a value $T_L(C_0)$, where C_0 is a reference liquid concentration and $T_L(C_0)$ is a liquidus temperature defined below. We assume that $T_L(C_0)$ is above the eutectic temperature, T_E and below $T_L(C_\infty)$. We consider a situation where a mushy region forms between the solid and liquid regions, with the stationary solid/mush and mush/liquid interfaces located at $z = a(x)$ and $z = b(x)$, respectively. We denote the local volume fraction of the liquid phase in the mushy region by χ. Note that while the interfaces are stationary, the solid moves with the substrate, as do the solid dendrites in the mushy region. The situation described above is sketched in Fig. 1.

To model the temperature, concentration and liquid fraction fields in the mushy region, we use the governing equations based on the local conservation of heat and solute derived by Schulze and Worster (2005) for a mushy region in which the speed of solid dendrites, the velocity of the intersticial fluid and the rate at which interfaces propagate are, in general,

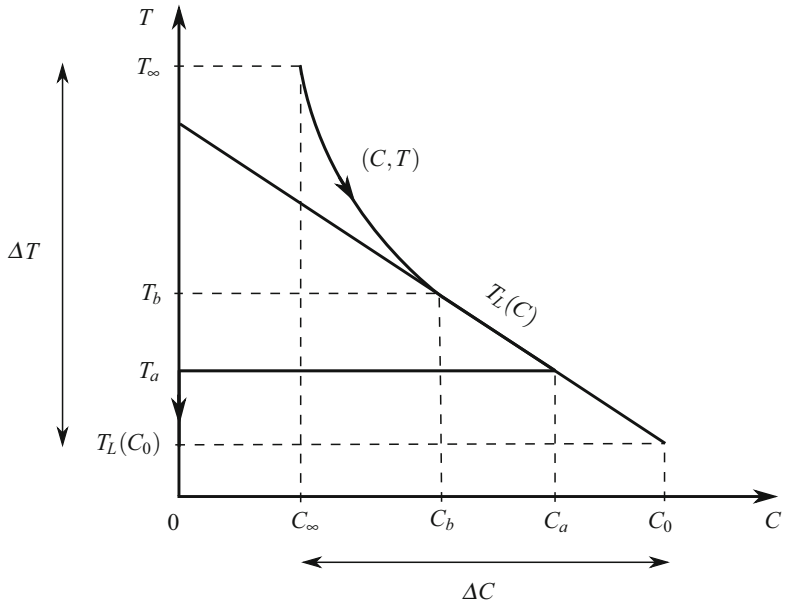

Fig. 2 Approximate binary phase diagram for a system with a mushy region, used in our paper. For the description of particular symbols, see text. Shown is also a typical trajectory (C, T) of a solidifying system (solid lines with arrows)

distinct. However, in the present situation, the interstitial flow is trivial relative to the dendrites, which is consistent with the Darcy equation in case the pressure field in the liquid portion of the mushy region is purely hydrostatic. Moreover, unlike Schulze and Worster (2005), we assume non-trivial solute diffusion in the liquid phase.

We denote $\mathbf{u} = (u, w)$ the flow velocity in the liquid and mushy regions, and the speed of material points embedded in the dendrites is $\mathbf{v} = U_0\hat{\mathbf{x}}$, where $\hat{\mathbf{x}}$ is the unit vector in the horizontal direction. According to the assumptions stated in the previous paragraph, the flow field in the mushy region is $\mathbf{u} \equiv \mathbf{v}$ so that the streamlines are parallel to the x-axis (see Fig. 1). In the mushy region, the temperature and concentration fields are coupled by the linear liquidus relationship

$$T = T_L(C) \equiv T_L(C_0) - \hat{\Gamma}(C - C_0), \tag{2.1}$$

where $\hat{\Gamma}$ is the constant, dimensional liquidus slope. A simple binary phase diagram used is depicted in Fig. 2. We assume that there is no mass diffusion in the solid and that the solid is free of solute.

We denote D the solutal diffusivity, κ the thermal diffusivity, L the latent heat per unit mass, ρ the density and ν the kinematic viscosity. The thermal properties of liquid and solid phases are set equal. We use U_0 as a velocity scale and κ/U_0 as a length scale. Since in the rest of the paper we will work only with the dimensionless formulation, we denote the dimensionless quantities by the same symbols as the dimensional ones. The dimensionless temperature and concentration are defined by

$$\theta = [T - T_L(C_0)]/\Delta T \quad \text{and} \quad \Theta = (C_0 - C)/\Delta C, \tag{2.2a,b}$$

respectively, with $\Delta T \equiv T_\infty - T_L(C_0)$ and $\Delta C \equiv C_0 - C_\infty$. Note that θ and Θ take values from the interval [0, 1]. In the mushy region,

$$\frac{\partial \theta}{\partial x} = \frac{\partial^2 \theta}{\partial x^2} + \frac{\partial^2 \theta}{\partial z^2} - \mathscr{S}\frac{\partial \chi}{\partial x}, \tag{2.3a}$$

$$(\Theta - \mathscr{C})\frac{\partial \chi}{\partial x} + \chi\frac{\partial \Theta}{\partial x} = \varepsilon\left[\frac{\partial}{\partial x}\left(\chi\frac{\partial \Theta}{\partial x}\right) + \frac{\partial}{\partial z}\left(\chi\frac{\partial \Theta}{\partial z}\right)\right], \tag{2.3b}$$

$$\theta = \theta_L(\Theta) \equiv \Gamma\Theta. \tag{2.3c}$$

The dimensionless numbers are the inverse Lewis number ε, the Stefan number $\mathscr{S}$, the concentration ratio $\mathscr{C}$ and the scaled liquidus slope Γ, defined, respectively, by

$$\varepsilon = D/\kappa, \quad \mathscr{S} = L/c_p\Delta T, \quad \mathscr{C} = C_0/\Delta C, \quad \Gamma = \hat{\Gamma}\Delta C/\Delta T, \tag{2.4a–d}$$

where c_p is the heat capacity. Note that the range of $\mathscr{C}$ is $(1, \infty)$ and that of Γ is $(0, 1)$. To see the latter, we first realize that $\hat{\Gamma} = [T_b - T_L(C_0)]/(C_0 - C_b)$ and that $[T_\infty - T_L(C_0)]/(C_0 - C_\infty) > [T_b - T_L(C_0)]/(C_0 - C_b)$, where the inequality follows directly from the phase diagram in Fig. 2. It is instructive to realize that the limiting case $\Gamma = 1$ corresponds to the situation in which the far-field values (C_∞, T_∞) lie on the liquidus.

The flow field in the liquid region is given by the incompressible Navier–Stokes equations and the temperature and concentration fields by the advection–diffusion equations. The temperature field in the solid phase obeys the advection–diffusion equation with the advection velocity being equal to $\mathbf{v}$.

We seek self-similar solutions with a self-similar variable ζ, defined by

$$\zeta = z/2x^{1/2}, \tag{2.5}$$

and with the dimensionless interfaces given as

$$a(x) = 2\lambda_a x^{1/2} \quad \text{and} \quad b(x) = 2\lambda_b x^{1/2}, \tag{2.6a,b}$$

where λ_a and λ_b are positive constants yet undetermined. In order to derive the boundary layer equations that allow self-similar solutions (see, for example, Löfgren 2001; Kyselica and Guba 2016), we consider the limit

$$x \to \infty, \quad \zeta = O(1), \tag{2.7}$$

so that $\mathbf{n}_a, \mathbf{n}_b \sim \hat{\mathbf{z}}$ to leading order, where $\mathbf{n}_a$ and $\mathbf{n}_b$ are the outward unit vectors normal to the respective interfaces and $\hat{\mathbf{z}}$ is the unit vector in vertical direction. The physical motivation for this limit is that the horizontal gradients of temperature and concentration are small relative to the gradients in vertical direction.

Below we state the resulting system of boundary layer equations along with corresponding boundary conditions.

Mushy region:

$$\frac{\partial \theta}{\partial x} = \frac{\partial^2 \theta}{\partial z^2} - \mathscr{S}\frac{\partial \chi}{\partial x}, \tag{2.8a}$$

$$(\Theta - \mathscr{C})\frac{\partial \chi}{\partial x} + \chi\frac{\partial \Theta}{\partial x} = \varepsilon\frac{\partial}{\partial z}\left(\chi\frac{\partial \Theta}{\partial z}\right), \tag{2.8b}$$

$$\theta = \Gamma\Theta. \tag{2.8c}$$

Liquid phase:

$$u\frac{\partial\theta}{\partial x}+w\frac{\partial\theta}{\partial z}=\frac{\partial^2\theta}{\partial z^2},\quad u\frac{\partial\Theta}{\partial x}+w\frac{\partial\Theta}{\partial z}=\varepsilon\frac{\partial^2\Theta}{\partial z^2},\tag{2.9a,b}$$

$$u\frac{\partial u}{\partial x}+w\frac{\partial u}{\partial z}=Pr\frac{\partial^2 u}{\partial z^2},\quad \frac{\partial u}{\partial x}+\frac{\partial w}{\partial z}=0.\tag{2.10a,b}$$

Solid phase:

$$\frac{\partial\theta}{\partial x}=\frac{\partial^2\theta}{\partial z^2}.\tag{2.11}$$

Mush/liquid interface:

$$\mathscr{S}(1-\chi_{b^-})\frac{\mathrm{d}b}{\mathrm{d}x}=\left.\frac{\partial\theta}{\partial z}\right|_{b^-}-\left.\frac{\partial\theta}{\partial z}\right|_{b^+},\tag{2.12a}$$

$$(\mathscr{C}-\Theta_b)(1-\chi_{b^-})\frac{\mathrm{d}b}{\mathrm{d}x}=\varepsilon\left(\left.\frac{\partial\Theta}{\partial z}\right|_{b^+}-\chi_{b^-}\left.\frac{\partial\Theta}{\partial z}\right|_{b^-}\right).\tag{2.12b}$$

Solid/mush interface:

$$\mathscr{S}\chi_{a^+}\frac{\mathrm{d}a}{\mathrm{d}x}=\left.\frac{\partial\theta}{\partial z}\right|_{a^-}-\left.\frac{\partial\theta}{\partial z}\right|_{a^+},\tag{2.13a}$$

$$(\mathscr{C}-\Theta_a)\chi_{a^+}\frac{\mathrm{d}a}{\mathrm{d}x}=\varepsilon\chi_{a^+}\left.\frac{\partial\Theta}{\partial z}\right|_{a^+}.\tag{2.13b}$$

The dimensionless Prandtl number is defined as

$$Pr=\nu/\kappa.\tag{2.14}$$

When deriving conditions (2.12a,b) and (2.13a,b), we used the fact that the local dimensionless velocities of the solid material elements relative to the solid/mush and mush/liquid interfaces, respectively, satisfy $-\mathbf{i}\cdot\mathbf{n}_h\propto \mathrm{d}h/\mathrm{d}x$, $h=a,b$. The boundary conditions on the velocity, temperature and concentration fields are

$$z=0:\ \ \theta=0,\tag{2.15a}$$

$$z=a:\ \ \theta_a=\Gamma\Theta_{a^+},\tag{2.15b}$$

$$z=b:\ \ u=1,\ w=0,\ \theta_b=\Gamma\Theta_b,\tag{2.15c–e}$$

$$z\to\infty:\ \ \theta\to 1,\ \Theta\to 1,\ u\to\mathscr{U},\tag{2.15f–h}$$

where

$$\mathscr{U}=U_\infty/U_0\tag{2.16}$$

is the scaled far-field velocity.

3 Self-Similar Reduction

In this section we state the self-similar formulation of the above problem. The governing equations in the liquid phase ahead of the mushy region can be sought explicitly in the limit of small Prandtl number, which is typical of liquid metal flows. Equations (2.10a,b), together with conditions (2.15c, d, h), define a viscous boundary layer problem (cf. Löfgren 2001; Kyselica and Guba 2016).

3.1 The Velocity Field in the Liquid Phase

We describe the velocity field via the stream function ψ defined by

$$u = \partial\psi/\partial z, \quad w = -\partial\psi/\partial x, \tag{3.1a,b}$$

and find that

$$\psi(x, z) = 2x^{1/2} f(\zeta; Pr), \tag{3.2}$$

where f is a solution of the third-order boundary layer problem studied previously (Löfgren 2001; Kyselica and Guba 2016). In the limit $Pr \to 0$, f takes the form

$$f \sim \lambda_b(1 - \mathscr{U}) + \mathscr{U}\zeta + Pr\frac{1 - \mathscr{U}}{2\lambda_b}\left[1 - \exp\left(-2\lambda_b\frac{\zeta - \lambda_b}{Pr}\right)\right], \tag{3.3}$$

provided $Pr/\lambda_b \ll \lambda_b$ in order that (3.3) remains asymptotic. The components of the flow field have the following asymptotic forms

$$u \sim 1 + (1 - \mathscr{U})\left[\exp\left(-2\lambda_b\frac{\zeta - \lambda_b}{Pr}\right) - 1\right], \tag{3.4a}$$

$$w \sim -\frac{1 - \mathscr{U}}{x^{1/2}}\left\{\lambda_b + \frac{Pr}{2\lambda_b} - \left(\zeta + \frac{Pr}{2\lambda_b}\right)\exp\left(-2\lambda_b\frac{\zeta - \lambda_b}{Pr}\right)\right\}, \tag{3.4b}$$

as $Pr \to 0$. Note that $w > 0$ ($w < 0$) when $\mathscr{U} > 1$ ($\mathscr{U} < 1$), see Fig. 3 (cf. Kyselica and Guba 2016 in the absence of mushy region). For $\mathscr{U} = 1$, there is no flow relative to the solid phase, and, on replacing x with the time variable, the problem is formally equivalent to the solidification of binary alloy with planar solid/mush and mush/liquid interfaces (Worster 1986).

3.2 The Temperature Fields in the Liquid and Solid Phases

Using (3.3), we can approximate the solution of (2.9a) in the following way (cf. Kyselica and Guba 2016)

$$\theta(\zeta) \sim 1 + (\theta_b - 1)\frac{\operatorname{erfc}\left[\mathscr{U}^{1/2}(\zeta - \lambda_b) + \mathscr{U}^{-1/2}\Lambda(\lambda_b)\right]}{\operatorname{erfc}\left[\mathscr{U}^{-1/2}\Lambda(\lambda_b)\right]}, \quad \zeta > \lambda_b, \tag{3.5}$$

where

$$\operatorname{erfc}(\zeta) = 1 - \operatorname{erf}(\zeta), \quad \operatorname{erf}(\zeta) = \frac{2}{\pi^{1/2}}\int_0^\zeta \mathrm{e}^{-s^2}\,\mathrm{d}s$$

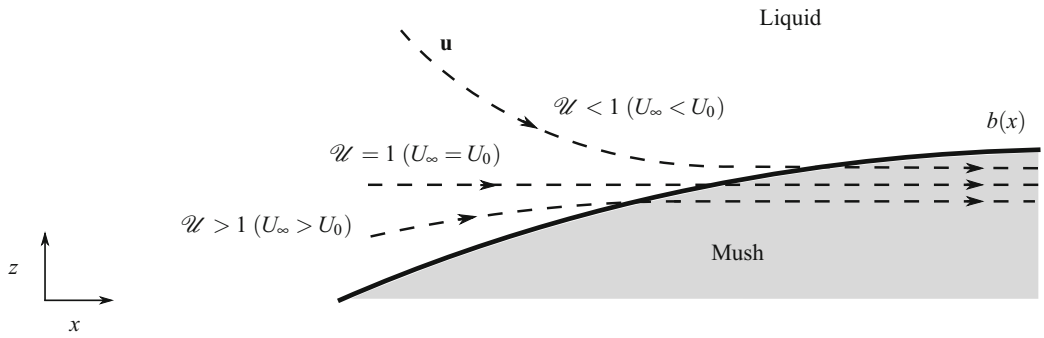

Fig. 3 Sketch of representative streamlines for qualitatively different values of $\mathscr{U}$. In the mushy region, the velocity field is equal to the velocity of the solid dendrites moving with the substrate

and

$$\Lambda(\lambda_b) \equiv \lambda_b + Pr(1 - \mathscr{U})/2\lambda_b. \tag{3.6}$$

Note that $\Lambda(\lambda_b) \sim \lambda_b + O(Pr)$ as $Pr \to 0$.

In the solid phase, Eq. (2.11) can be solved to obtain the temperature field in the following form

$$\theta = \theta_a \frac{\mathrm{erf}(\zeta)}{\mathrm{erf}\,(\lambda_a)}, \tag{3.7}$$

with θ_a yet to be determined from the conditions at the solid/mush interface. Hence, the temperature gradient on the solid side of the interface is

$$\theta'_{a^-} = \frac{2\lambda_a \theta_a}{G(\lambda_a)}, \tag{3.8}$$

with

$$G(\lambda) \equiv \pi^{1/2} \lambda\, \mathrm{e}^{\lambda^2}\, \mathrm{erf}(\lambda). \tag{3.9}$$

3.3 Concentration Field in the Liquid Phase

The solution of (2.9b) can be approximated analogously as that of (2.9a). For $Pr \to 0$ we obtain

$$\Theta(\zeta) \sim 1 + (\Theta_b - 1) \frac{\mathrm{erfc}\left[(\mathscr{U}/\varepsilon)^{1/2}(\zeta - \lambda_b) + (\mathscr{U}\varepsilon)^{-1/2}\Lambda(\lambda_b)\right]}{\mathrm{erfc}\left[(\mathscr{U}\varepsilon)^{-1/2}\Lambda(\lambda_b)\right]}, \quad \zeta > \lambda_b. \tag{3.10}$$

3.4 Liquid Fraction in the Mushy Region and the Interface Conditions

In the mushy region, the temperature and concentration fields are coupled via the liquidus relationship (2.8c). Hence, Eq. (2.8b) determines the liquid fraction and after the self-similar transformation it takes the following form

$$\frac{\chi'}{\chi} = \frac{2\zeta\Theta' + \varepsilon\Theta''}{2\zeta(\mathscr{C} - \Theta) - \varepsilon\Theta'}, \tag{3.11}$$

or, equivalently (cf. Gewecke and Schulze 2011b),

$$\chi = \chi_{b^-} \exp\left(-\int_{\zeta}^{\lambda_b} \frac{2s\Theta' + \varepsilon\Theta''}{2s(\mathscr{C} - \Theta) - \varepsilon\Theta'}\, \mathrm{d}s\right). \tag{3.12}$$

The equation for the temperature field in the mushy region can be combined with the liquidus relationship to yield

$$\Theta'' + 2\zeta\Theta' = -2\frac{\mathscr{S}}{\Gamma}\zeta\chi'. \tag{3.13}$$

The conservation of heat and solute at the solid/mush interface, given by (2.13a,b), respectively, can be expressed as

$$(2\mathscr{S}\lambda_a\chi_{a^+} + \Gamma\Theta'_{a^+})G(\lambda_a) = 2\Gamma\lambda_a\Theta_a, \tag{3.14a}$$

$$\left[2\lambda_a(\mathscr{C} - \Theta_{a^+}) - \varepsilon\Theta'_{a^+}\right]\chi_{a^+} = 0, \tag{3.14b}$$

where we have used (2.8c), to obtain (3.14b). The conservation of heat and solute at the mush/liquid interface, given by (2.12a,b), respectively, can be expressed as

$$2\mathscr{S}(1 - \chi_{b^-})\lambda_b = \Gamma\left(\Theta'_{b^-} - \Theta'_{b^+}\right), \tag{3.15a}$$

$$2(\mathscr{C}-\Theta_b)(1-\chi_{b^-})\lambda_b=\varepsilon\left(\Theta'_{b^+}-\chi_{b^-}\Theta'_{b^-}\right). \tag{3.15b}$$

To derive (3.15a), we have taken into account the condition of marginal equilibrium, introduced by Worster (1986), ensuring that none of the liquid ahead of the mush/liquid interface is constitutionally supercooled. In the self-similar terms, the marginal equilibrium reads

$$\theta'_{b^+}=\Gamma\Theta'_{b^+}. \tag{3.16}$$

Though the differential equation (3.11) can be readily integrated to obtain (3.12), it is instructive, however, to cast it into the following integral form

$$\int_{\lambda_a}^{\zeta}(\mathscr{C}-\Theta)\chi\,\mathrm{d}s=\tfrac{1}{2}\left[2\zeta(\mathscr{C}-\Theta)-\varepsilon\Theta'\right]\chi,\quad \lambda_a<\zeta<\lambda_b, \tag{3.17}$$

which turns out to be useful in further analysis. To derive (3.17), we used (3.14b). Evaluating (3.17) at the mush/liquid interface, we obtain

$$\int_{\lambda_a}^{\lambda_b}(\mathscr{C}-\Theta)\chi\,\mathrm{d}s=\tfrac{1}{2}\left[2\lambda_b(\mathscr{C}-\Theta_b)-\varepsilon\Theta'_{b^-}\right]\chi_{b^-}, \tag{3.18}$$

where the integral represents the total dimensionless amount of solute contained within the mushy region and takes only positive values.

Using (3.18), we can show that

$$\chi_{b^-}=1 \tag{3.19}$$

holds for general values of Stefan number so that the concentration gradient is continuous across the interface, i.e. $\Theta'_{b^-}=\Theta'_{b^+}$. To prove (3.19), we manipulate condition (3.15b) to show that $\chi_{b^-}=1+\varepsilon(\Theta'_{b^-}-\Theta'_{b^+})/[2\lambda_b(\mathscr{C}-\Theta_b)-\varepsilon\Theta'_{b^-}]$. The denominator of the second term in this expression is positive by (3.18), while the numerator is non-negative by (3.15a). However, since $0\le\chi_{b^-}\le 1$, it follows that the numerator must be zero.

From condition (3.14b) we know that at least one of the quantities $2\lambda_a(\mathscr{C}-\Theta_{a^+})-\varepsilon\Theta'_{a^+}$ or χ_{a^+} must vanish. However, in what follows, we neglect the effects of latent heat by setting the Stefan number to zero, noting that the limit is regular. In that case, (3.12) and (3.17) can be used to show that

$$2\lambda_a(\mathscr{C}-\Theta_{a^+})-\varepsilon\Theta'_{a^+}=0 \tag{3.20}$$

and that the liquid fraction is continuous across the solid/mush interface.

4 Results for Finite $\mathscr{U}$

The present problem involves several dimensionless numbers, which can be divided into two groups. In the first group are the numbers characterizing the boundary layer flow in the liquid phase: Prandtl number Pr and the velocity ratio $\mathscr{U}$. To the second group belong the numbers characterizing the solidification process without flow: Stefan number $\mathscr{S}$, inverse Lewis number ε, concentration ratio $\mathscr{C}$ and the dimensionless liquidus slope Γ. As stated at the end of the previous section, we will assume that the Stefan number is negligible and set $\mathscr{S}=0$ in the rest of our investigation. In this regular limit, the coupling between Eqs. (3.11) and (3.13) vanishes.

To simplify our computations, it is instructive to consider the limit $\varepsilon\to 0$. Before doing that, however, we will consider the solutions for finite values of ε. The main goal of our analysis is to study the effect of varying the velocity ratio on the mushy region dimensionless thickness, proportional to $\lambda_b-\lambda_a$. We will consider both finite and small values of $\mathscr{U}$.

4.1 Solutions with $\varepsilon = O(1)$

With Stefan number neglected, the temperature field in both the solid phase and the mushy region is given by (3.7) and the concentration field in the mushy region is

$$\Theta = \Theta_{a^+} \frac{\mathrm{erf}(\zeta)}{\mathrm{erf}(\lambda_a)}. \tag{4.1}$$

Equations (3.14a,b) yield

$$\Theta_{a^+} = \frac{\mathscr{C} G(\lambda_a)}{G(\lambda_a) + \varepsilon} \quad \text{and} \quad \Theta'_{a^+} = \frac{2\lambda_a \mathscr{C}}{G(\lambda_a) + \varepsilon}. \tag{4.2a,b}$$

Evaluating (4.1) at $\zeta = \lambda_b$, we obtain $\Theta_{a^+}/\,\mathrm{erf}(\lambda_a) = \Theta_b/\,\mathrm{erf}(\lambda_b)$, which, together with (4.2a), results in the algebraic equation for the growth constant λ_a as

$$\left[\Theta_b - \mathscr{C} \frac{\mathrm{erf}(\lambda_b)}{\mathrm{erf}(\lambda_a)}\right] G(\lambda_a) + \varepsilon \Theta_b = 0. \tag{4.3}$$

The condition of marginal equilibrium, (3.16), can be combined with the continuity of the concentration gradient across the mush/liquid interface to obtain the continuity of the temperature gradient, i.e. $\theta'_{b^-} = \theta'_{b^+}$. From (3.5), (3.10) and the continuity conditions, the growth constant λ_b is governed by

$$\varepsilon \lambda_b F\left[\frac{\Lambda(\lambda_b)}{(\varepsilon \mathscr{U})^{1/2}}\right] - \Gamma \lambda_b F\left[\frac{\Lambda(\lambda_b)}{\mathscr{U}^{1/2}}\right] + (1-\Gamma)\Lambda(\lambda_b) G(\lambda_b) = 0, \tag{4.4}$$

where

$$F(\lambda) \equiv \pi^{1/2} \lambda\, \mathrm{e}^{\lambda^2}\, \mathrm{erfc}(\lambda). \tag{4.5}$$

The temperature and concentration at the mush/liquid interface are

$$\theta_b = 1 - \frac{\lambda_b F\left[\Lambda(\lambda_b)/\mathscr{U}^{1/2}\right]}{\lambda_b F\left[\Lambda(\lambda_b)/\mathscr{U}^{1/2}\right] + \Lambda(\lambda_b) G(\lambda_b)}, \tag{4.6a}$$

$$\Theta_b = 1 - \frac{\varepsilon \lambda_b F\left[\Lambda(\lambda_b)/(\varepsilon \mathscr{U})^{1/2}\right]}{\varepsilon \lambda_b F\left[\Lambda(\lambda_b)/(\varepsilon \mathscr{U})^{1/2}\right] + \Lambda(\lambda_b) G(\lambda_b)}. \tag{4.6b}$$

Note that λ_b is independent of $\mathscr{C}$ since the concentration ratio enters the mush/liquid interface conditions only through the left-hand side of (3.15b), which is, however, equal to zero in the present case. In Fig. 4 we plot the growth constant λ_b as a function of $\mathscr{U}$, calculated from (4.4). Note that a second branch of solutions emerges at $\mathscr{U} = 1$ and that there is a special value $\mathscr{U}_{\max}$ at which the two branches merge together. No solutions exist for $\mathscr{U} > \mathscr{U}_{\max}$. Note that $\mathscr{U}_{\max} \to \infty$ as $Pr \to 0$. The present results can be compared with Fig. 4 by Kyselica and Šimkanin (2017), where finite solutions for λ_b existed for all values of $\mathscr{U}$.

In Fig. 5 we plot the growth constants λ_a, calculated from (4.3), for each branch of λ_b. Note that for the upper branch of λ_b all the values of λ_a are physically realistic, i.e. $\lambda_a < \lambda_b$. For the lower branch, however, there is a special value $\mathscr{U}_{\min} > 1$ such that the values of λ_a are physically realistic only for $\mathscr{U} > \mathscr{U}_{\min}$. The solutions for $1 < \mathscr{U} < \mathscr{U}_{\min}$ are not shown. The lower portion of the λ_b branch is technically valid only for $\mathscr{U} \gtrsim 2$ since our asymptotic results require $\lambda_b \gg Pr^{1/2}$.

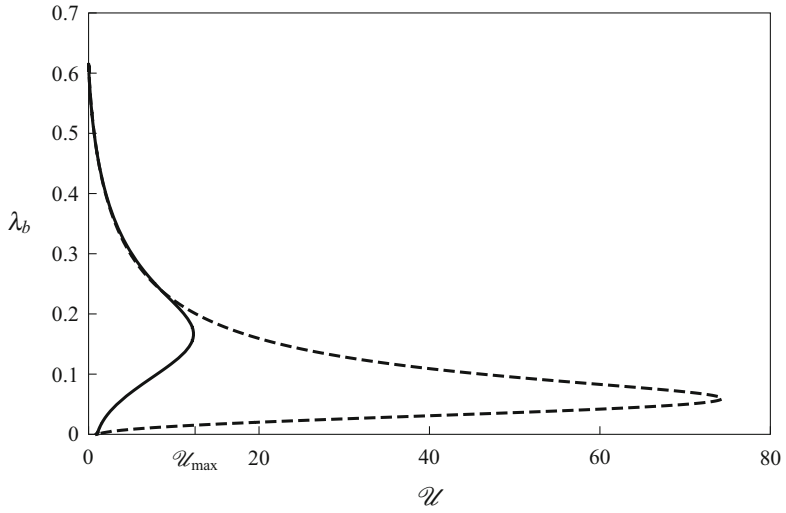

Fig. 4 Growth constant λ_b as a function of $\mathscr{U}$, calculated from (4.4) for $Pr = 10^{-2}$ (solid line) and $Pr = 10^{-3}$ (dashed line). Note that a second branch of solutions emerges at $\mathscr{U} = 1$ and that the two branches merge together at a finite value of $\mathscr{U}$, denoted as $\mathscr{U}_{\max}$. No solutions exist for $\mathscr{U} > \mathscr{U}_{\max}$. Note that $\mathscr{U}_{\max} \to \infty$ as $Pr \to 0$. The values of the other parameters are set to $\varepsilon = 10^{-2}$, $\Gamma = 0.5$ and $\mathscr{C} = 2$

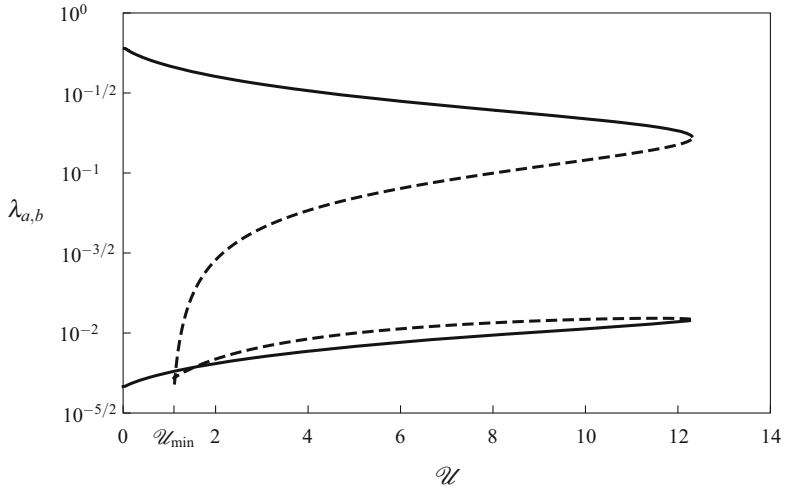

Fig. 5 Growth constants λ_a (the lower pair) and λ_b (the upper pair) as functions of $\mathscr{U}$, calculated from (4.3) and (4.4). A logarithmic scale was used on the vertical axis. The values of λ_a corresponding to both branches of λ_b (cf. Fig. 4) are shown—each branch of λ_a uses the same line type as the corresponding branch of λ_b. The values of the other parameters are set to $Pr = 10^{-3}$, $\varepsilon = 10^{-2}$, $\Gamma = 0.5$ and $\mathscr{C} = 2$

4.2 Solutions in the Limit $\varepsilon \to 0$

The inverse Lewis number, ε, is typically small owing to the fact that the solute diffusivity is usually negligible when compared to the heat diffusivity. Since the growth rate of the mushy region is determined by the heat balances at the interfaces, the mushy region exists even when the diffusion of solute away from the mush/liquid interface is negligible (cf. Worster 2000), i.e. when $\varepsilon = 0$. In such a case, no solid region forms between the cooled substrate and the mushy region (cf. Gewecke and Schulze 2011a for the case of a mushy region with planar

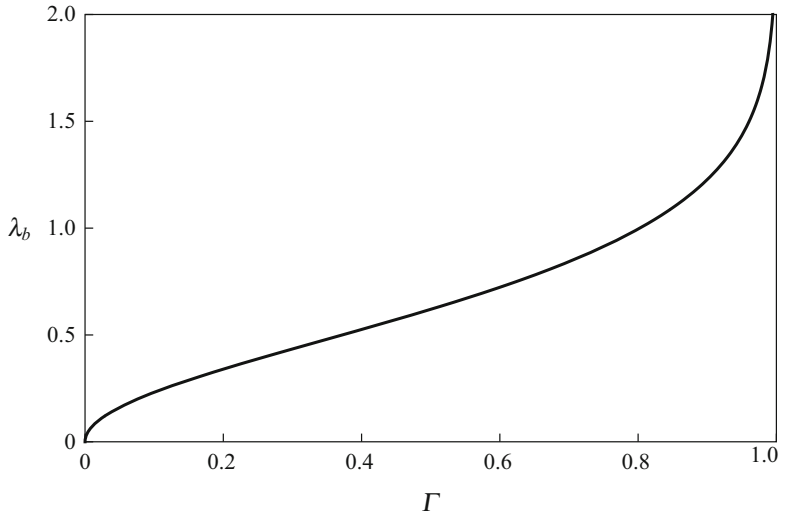

Fig. 6 Leading-order solution of (4.9), calculated from (4.10), as a function of Γ. Note that Γ measures the drop of the melting temperature across the system relative to that of the temperature, cf. (2.4d). Note the singularity in λ_b as $\Gamma \to 1^-$

interfaces). In the limit $\varepsilon \to 0$, a concentration boundary layer of thickness $O(\varepsilon^{1/2})$ forms ahead of the mush/liquid interface.

Since $F(s) \sim 1$ as $s \to \infty$, Eq. (4.4) implies that $\lambda_b = O(1)$ as $\varepsilon \to 0$ and therefore $\Theta_b \to 1$ as $\varepsilon \to 0$, see (4.6b). From (4.3) we have that $\lambda_a \to 0$ as $\varepsilon \to 0$; otherwise, we would obtain that $\lambda_a > \lambda_b$, which is not a physical solution. An approximate solution of (4.3) can be found as

$$\lambda_a = \frac{\varepsilon}{\pi^{1/2}\mathscr{C}\,\mathrm{erf}(\lambda_b)} + O(\varepsilon^2) \quad \text{as} \quad \varepsilon \to 0. \tag{4.7}$$

We see from (4.7) that the thickness of the solid phase decreases with $\mathscr{C}$. Note that increasing $\mathscr{C}$ is equivalent to decreasing ΔC, with C_0 fixed.

We can combine (4.7) with (4.2a,b) to obtain the concentration and its gradient at the mush bottom

$$\Theta_{a^+} \sim \frac{2\varepsilon\mathscr{C}}{\pi\mathscr{C}^2\,\mathrm{erf}^2(\lambda_b) + 2\varepsilon} \quad \text{and} \quad \Theta'_{a^+} \sim \frac{2\pi^{1/2}\mathscr{C}^2\,\mathrm{erf}(\lambda_b)}{\pi\mathscr{C}^2\,\mathrm{erf}^2(\lambda_b) + 2\varepsilon}. \tag{4.8a,b}$$

As the limit $Pr \to 0$ is regular for λ_b, in order to simplify (4.4), we set $Pr = 0$ so that

$$\varepsilon F\left[\frac{\lambda_b}{(\varepsilon\mathscr{U})^{1/2}}\right] - \Gamma F\left(\frac{\lambda_b}{\mathscr{U}^{1/2}}\right) + (1-\Gamma)G(\lambda_b) = 0. \tag{4.9}$$

The solution of (4.9) can be approximated by the solution of the following equation

$$G(\lambda_b) = \frac{\Gamma}{1-\Gamma} \tag{4.10}$$

to leading order in ε and $\mathscr{U}$. Since the range of G is $(0, \infty)$, there exists a unique solution of (4.10) for every $\Gamma \in (0, 1)$. Note that $\Theta_b \to 1$ and $\theta_b \to \Gamma$ as $\varepsilon \to 0$. The numerical solution of (4.10) is shown in Fig. 6. Note the singularity in λ_b as $\Gamma \to 1^-$.

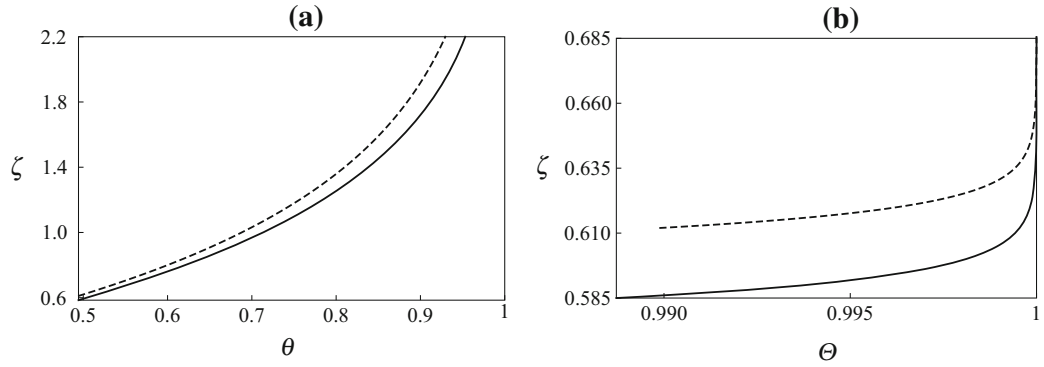

Fig. 7 Temperature (**a**) and concentration (**b**) fields in the liquid phase as functions of ζ, given by (3.5) and (3.10) for $\mathscr{U} = 10^{-1}$ (solid lines), compared with the asymptotic forms (5.2a, b) for $\mathscr{U} = 0$ (dashed lines). The values of the other parameters are set to $Pr = 10^{-2}$, $\varepsilon = 10^{-2}$ and $\Gamma = 0.5$

5 Results for $\mathscr{U} = 0$

Though the limit $\mathscr{U} \to 0$ is regular, it is instructive to look separately at the case when $\mathscr{U} = 0$. Such a situation corresponds to setting the far-field velocity, U_∞, to zero. In this parametric regime, we are able to determine the exact scalings of the dimensional positions of the interfaces with the substrate speed U_0, since the dimensional forms for these interfaces are

$$a(x) = 2\lambda_a \left(\kappa x / U_0\right)^{1/2} \quad \text{and} \quad b(x) = 2\lambda_b \left(\kappa x / U_0\right)^{1/2}, \tag{5.1a,b}$$

with both λ_a and λ_b independent of U_0 when $\mathscr{U} = 0$ since U_0 enters the governing equations only through $\mathscr{U}$. Therefore, with growing U_0, the positions of both interfaces decrease proportionally to $U_0^{-1/2}$.

The function f has the same asymptotic expansion as that given in (3.3), with $\mathscr{U} = 0$. The temperature and concentration fields in the liquid phase can be expressed as

$$\theta \sim 1 - \frac{1-\Gamma}{1-\varepsilon} \exp\left[-\frac{2\lambda_b^2 + Pr}{\lambda_b} (\zeta - \lambda_b) \right], \tag{5.2a}$$

$$\Theta \sim 1 - \frac{\varepsilon(1-\Gamma)}{\Gamma(1-\varepsilon)} \exp\left[-\frac{2\lambda_b^2 + Pr}{\varepsilon\lambda_b} (\zeta - \lambda_b) \right], \tag{5.2b}$$

as $Pr \to 0$. Note that factor ε^{-1} is present in the exponent of (5.2b), which is in contrast to the factor $\varepsilon^{-1/2}$ in (3.10). In Fig. 7 we show typical profiles of the temperature and concentration fields, given by (5.2a, b); shown are also the profiles corresponding to positive values of $\mathscr{U}$. The growth constant λ_b is a root of the algebraic equation

$$G(\lambda_b) \left(1 + \frac{Pr}{2\lambda_b^2} \right) = \frac{\Gamma - \varepsilon}{1 - \Gamma}, \tag{5.3}$$

which has positive solutions only if $\Gamma > \varepsilon$. It is straightforward to show that $\lambda_b = O(1)$ as $Pr \to 0$; hence, the condition $Pr/\lambda_b \ll \lambda_b$ is satisfied and (3.3) retains its asymptoticity. For $Pr \to 0$ and $\varepsilon \to 0$ Eq. (5.3) reduces to (4.10).

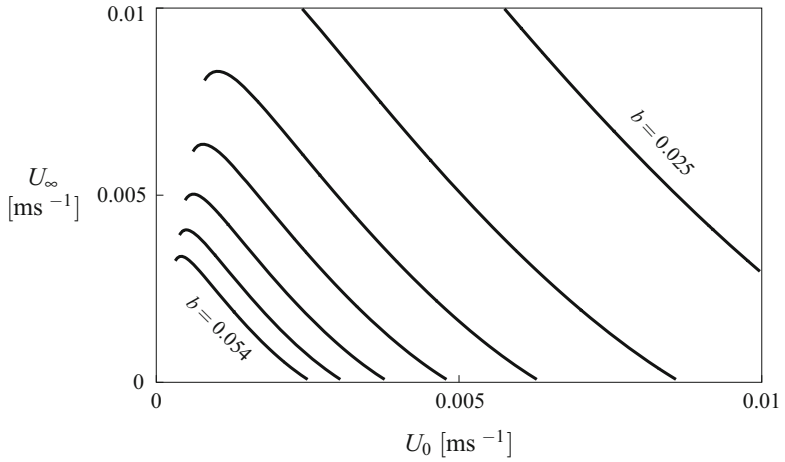

Fig. 8 Contours of equally spaced levels of the dimensional position (in m) of the mush/liquid interface, given in (5.1b), for $x = 1$ m and $\kappa = 5 \times 10^{-6}$ m^2 s^{-1} (cf. Kyselica and Guba 2016). The values of the other parameters are set to $Pr = 10^{-2}$, $\varepsilon = 10^{-2}$ and $\Gamma = 0.5$. The range of $\mathscr{U}$ shown in the plot is $0 \le \mathscr{U} \le 10$. The horizontal axis corresponds to $\mathscr{U} = 0$. Note the non-monotonicity of b as a function of U_0 in the region close to the line $\mathscr{U} = 10$

We can use (5.2b) together with (3.18) to obtain, in dimensionless terms, the total amount of solute within the mushy region as

$$\int_{\lambda_a}^{\lambda_b} (\mathscr{C} - \Theta)\chi \, \mathrm{d}s = \lambda_b(\mathscr{C} - 1) - \frac{\varepsilon Pr(1-\Gamma)}{2\lambda_b \Gamma(1-\varepsilon)}. \tag{5.4}$$

Recall that $\mathscr{C} - \Theta = C/\Delta C$. The integral in (5.4) measures the redistribution of the solute in the system. Note that the total amount of solute within the mushy region is determined dominantly by $\mathscr{C}$, with the other effects being of order $O(\varepsilon Pr)$ as ε, $Pr \to 0$. The average bulk composition in the mushy region is, to the leading order in small ε, equal to $\mathscr{C} - 1$.

6 Conclusions

In the present study, we have studied the effect of the scaled far-field velocity, $\mathscr{U}$, and the Prandtl number, Pr, on the mushy region characteristics. The analysis can be compared with the one given by Kyselica and Guba (2016) of a similar problem without a mushy region: the dimensionless thickness of the solid phase was $O(\mathscr{U}^{1/2})$, provided $Pr \ll \mathscr{U}$. Such a scaling corresponds to the dimensional thickness being proportional to $U_\infty^{1/2}/U_0$. In the present case, however, the dimensionless thickness of both the solid and mushy regions is finite as $\mathscr{U} \to 0$, which corresponds to the dimensional thickness proportional to $1/U_0^{1/2}$. In Fig. 8 we plot the contours of the dimensional position of the mush/liquid interface, given in (5.1b), for general values of $\mathscr{U}$, in terms of U_0 and U_∞. An interesting feature is the non-monotonicity of b as a function of U_0 in the region close to the line $\mathscr{U} = 10$.

In the problem without the mush, the small values of the velocity ratio force the thermal and compositional boundary layers ahead of the solid/liquid interface to grow as $O(\mathscr{U}^{-1/2})$. In the system with a mushy region the effect of small velocity ratio on the thermal and compositional boundary layers is, to leading order, negligible, as shown in Fig. 7.

From our findings, we highlight the integral relationships (3.18) and (5.4) that quantify the total amount of solute contained within the mushy region. As can be seen from (5.4),

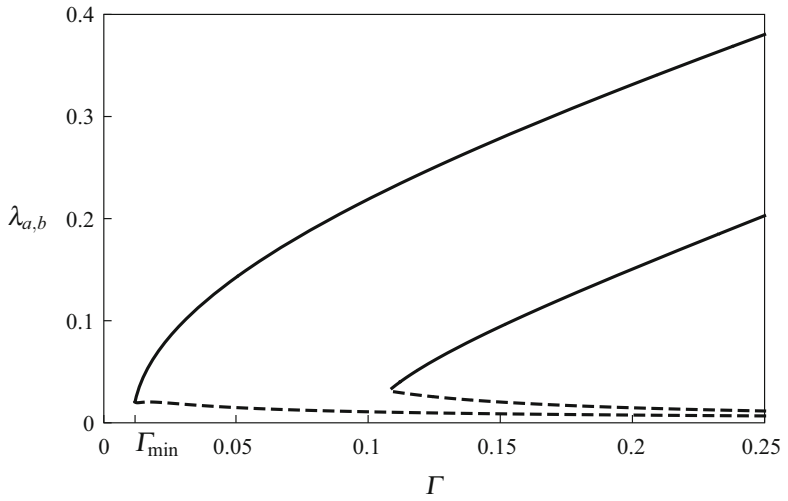

Fig. 9 Growth constants λ_a (dashed) and λ_b as functions of Γ, calculated from (4.3) and (5.3) (left pair), compared with the growth constants corresponding to the mushy region studied by Worster (1986), calculated from (4.3) and (4.4), with $\mathscr{U} = 1$. Note that there is a value $\Gamma = \Gamma_{\min}$, such that $\lambda_a = \lambda_b$. Physically realistic solutions exist only for $\Gamma > \Gamma_{\min}$. The behaviour of λ_b for higher values of Γ is qualitatively similar to Fig. 6. The values of the other parameters are set to $Pr = 10^{-3}$, $\varepsilon = 10^{-2}$ and $\mathscr{C} = 2$

when the Prandtl number is small, the total amount of solute is proportional to $\mathscr{C} - 1$, with the correction of $O(\varepsilon Pr)$. The $O(\varepsilon Pr)$ effect is weakened when the values of Γ are close to unity: the resulting small temperature and compositional gradients in the liquid make the effect of the boundary layer flow less important.

The dimensionless parameter Γ, which is proportional to the ratio of the compositional and thermal differences across the system, deserves a special comment. It is straightforward to show that $\Gamma = [T_L(C_\infty) - T_L(C_0)]/\Delta T$ and that the right-hand side of (4.10) can be expressed as a ratio of the driving temperature differences, i.e. $[T_L(C_\infty) - T_L(C_0)]/[T_\infty - T_L(C_\infty)]$.

In Fig. 9 we plot the growth constants λ_a and λ_b as functions of Γ, calculated from (4.3) and (5.3), together with those corresponding to the mushy region without horizontal pulling, calculated from (4.3) and (4.4) with $\mathscr{U} = 1$ (cf. Worster 1986; see also the comment at the end of Sect. 3.1). Note that in both cases there is a critical value $\Gamma = \Gamma_{\min}$ for which $\lambda_a = \lambda_b$. For $\Gamma < \Gamma_{\min}$ we have $\lambda_a > \lambda_b$, which is not physically realistic. In Fig. 10 we show $\Gamma_{\min}$ as a function of $\mathscr{U}$—the values of $\Gamma_{\min}$ are found to attain their maximum values at $\mathscr{U} = 1$. Thus, the horizontal pulling and the resulting flow in the liquid enhance the formation of a mushy region: when the system is pulled horizontally, the range of Γ for which the mush exists is larger than that for the system without pulling.

The fact that there is a value of Γ below which the mushy region does not exist can be used, together with (2.4d), to derive the bounds on C_∞ or T_∞. With ΔC fixed, we have an upper bound for the far-field temperature for which the mushy region exists: $T_\infty < T_L(C_0) + \hat{\Gamma}\Delta C/\Gamma_{\min}$. Similarly, with ΔT fixed, there is an upper bound for the far-field concentration: $C_\infty < C_0 - \Gamma_{\min}\Delta T/\hat{\Gamma}$. In the situation with horizontal pulling, these bounds are found to be higher than those in the case without pulling, studied by Worster (1986).

It may be of some interest to extend the present calculation to include the effects of buoyancy-driven flow in the system. In the present case, we assumed constant density and hydrostatic pressure; therefore, the flow field relative to the solid portion of the mushy region was zero. Within the framework of self-similarity, determination of the interacting fields

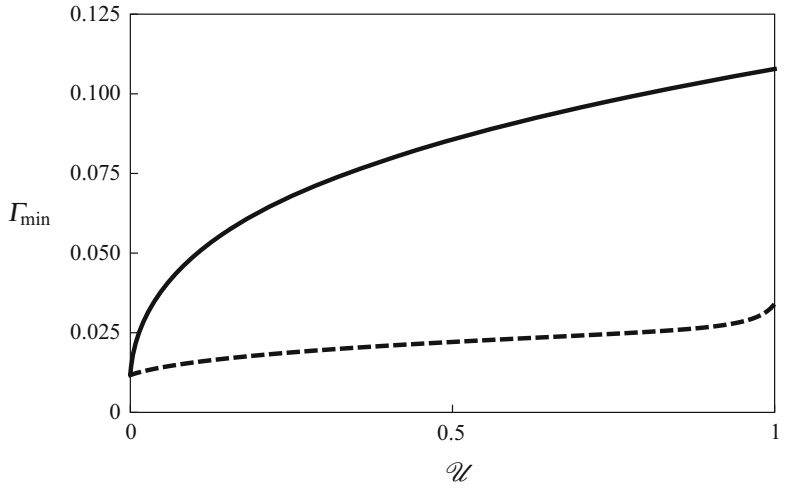

Fig. 10 Minimum value of Γ for which the mushy region exists, $\Gamma_{\min}$, as a function of $\mathscr{U}$. Two qualitatively different asymptotic regimes are shown: the solid curve corresponds to $Pr \ll \varepsilon$, with $Pr = 10^{-3}$ and $\varepsilon = 10^{-2}$; the dashed curve corresponds to $Pr \gg \varepsilon$, with $Pr = 10^{-2}$ and $\varepsilon = 10^{-3}$. Note that $\Gamma_{\min}$ attains finite values at $\mathscr{U} = 0$. In all computations we set $\mathscr{C} = 2$

would require a suitable choice of the conditions at the mush/liquid interface since the fluid velocity can be distinct from the velocity of the solid phase dictated by the substrate pulling and the fluid can eventually flow across the solidifying interface (see Schulze and Worster 2005).

References

Davis, S.H.: Theory of Solidification. Cambridge University Press, Cambridge (2001)
Deguen, R., Alboussière, T., Brito, D.: On the existence and structure of a mush at the inner core boundary of the Earth. Phys. Earth Planet. Inter. **164**, 36–49 (2007)
Fowler, A.C.: The formation of freckles in binary alloys. IMA J. Appl. Math. **35**, 159–174 (1985)
Gewecke, N.R., Schulze, T.P.: The rapid advance and slow retreat of a mushy zone. J. Fluid Mech. **674**, 227–243 (2011a)
Gewecke, N.R., Schulze, T.P.: Solid-mush interface conditions for mushy layers. J. Fluid Mech. **689**, 357–375 (2011b)
Guba, P., Worster, M.G.: Free convection in laterally solidifying mushy regions. J. Fluid Mech. **558**, 69–78 (2006)
Kyselica, J., Šimkanin, J.: Global conservation model for a mushy region over a moving substrate. Phys. Earth Planet. Inter. (2017). https://doi.org/10.1016/j.pepi.2017.07.012
Kyselica, J., Guba, P.: Forced flow and solidification over a moving substrate. Appl. Math. Model. **40**, 31–40 (2016)
Löfgren, H.B.: Ideal solidification of a liquid–metal boundary layer flow over a conveying substrate. J. Fluid Mech. **446**, 121–131 (2001)
Schulze, T.P., Worster, M.G.: Weak convection, liquid inclusions and the formation of chimneys in mushy layers. J. Fluid Mech. **388**, 197–215 (1999)
Schulze, T.P., Worster, M.G.: A time-dependent formulation of the mushy-zone free boundary problem. J. Fluid Mech. **541**, 193–202 (2005)
Steen, P.H., Karcher, C.: Fluid mechanics of spin casting of metals. Annu. Rev. Fluid Mech. **29**, 373–397 (1997)
Tangthieng, C., Cheung, F.B.: Thermosolutal transport and macrosegregation during freeze coating of a binary substance on a continuous moving object. Int. J. Heat Mass Transf. **46**, 2313–2327 (2003)
Tangthieng, C., Cheung, F.B., Shiah, S.W.: Behavior of the two-phase mushy zone during freeze coating on a continuous moving plate. J. Heat Transf. **124**, 111–119 (2002)

Worster, M.G.: Solidification of an alloy from a cooled boundary. J. Fluid Mech. **167**, 481–501 (1986)
Worster, M.G.: Solidification of fluids. In: Batchelor, G.K., Moffat, H.K., Worster, M.G. (eds.) Perspectives in Fluid Dynamics: A Collective Introduction to Current Research, pp. 393–446. Cambridge University Press, Cambridge (2000)
Worster, M.G., Jones, D.W.R.: Sea-ice thermodynamics and brine drainage. Philos. Trans. R. Soc. A **373**(20140), 166 (2015)

Acta Math. Univ. Comenianae
Vol. (submitted to AMUC), pp. 1–15

STEADY NON-CONVECTION STATES IN TERNARY ALLOY SOLIDIFICATION

M. HURBAN

Abstract. We consider a steady non-convecting state of a mushy layer during the primary solidification of a ternary alloy. A model, which includes the effects thermal and solutal diffusion, segregation effects and finite speed of background solidification is considered. Two types of boundary conditions are applied, either fixing solute flux or concentration at the bottom of the mush. In the regime of the same Lewis numbers and segregation coefficients of solutes, explicit solution using hypergeometric functions was identified. In the limit of large Lewis and the limit of near constant concentration profile of one solute asymptotic solutions were presented. The behaviour of the concentration profiles was analysed with respect to a static stability scenario, i.e. distribution of a mass within liquid.

1. Introduction

The solidification of multicomponent mixtures includes complex phenomena occurring both in natural and industrial processes. Phase change in a solidifying system proceeds on a solidification interface, which is often morphologically unstable. For dilute binary alloys criterion for predicting instability of solidification interface was presented in [**11**]. Such instability leads to formation of dendrites – treelike structures of solid crystal. A zone where liquid mixture and solid crystals coexist is called a mushy layer. In the work [**13**] the mushy layer is considered a continuum with local solid fraction as a function of distance from the cooled boundary.

We consider setup of directional solidification characterized by a liquid being forced downward with average speed V^* and temperature gradient constant in the laboratory frame of reference (e.g. [**14**], [**12**], [**3**]). For an aqueous ternary alloy, a solidifying system is composed of a liquid layer, a primary mush and a secondary mush, with mushy layers separated by planar interfaces. The primary mush is characterized by crystals composed of one solute species and presence of two independent diffusive fields. In the secondary mush crystals are composed of two solute species and only one independent diffusive field is present.

Received ....
2000 *Mathematics Subject Classification.* Primary 76M45, 35C20, 80A22.
Key words and phrases. solidification of ternary alloys, mushy layers, static stability, asymptotic approximations, hypergometric functions.
The authors gratefully acknowledge the financial support from the project VEGA 1/0347/18.

When thermal equilibrium is maintained throughout the mushy layer, liquidus constraint will cause secondary mush to behave like effectively a binary mixture. The processes ongoing in binary mixtures has been widely described in [**15**], [**7**]. To explain most distinctive behaviour of the full ternary model we will analyse only the processes within the primary mush. This approach was used in [**4**], [**8**], [**9**], with the aim was to investigate an occurrence of a direct mode of instability present in a statically stably stratified scenario i.e. when the density of fluid decreases with height.

The same setup as in [**4**] was considered in [**8**], with aim to analyse the joint limit of small speed of background solidification, small variation concentration across the primary mush and large Stefan number, with effects of solute rejection incorporated.

We consider the model from [**4**], [**8**], [**9**] for directional solidification of ternary mixtures, incorporating thermal and solutal diffusion, segregation effects and finite speed of the background solidification. Apart from the boundary conditions (BC) prescribing constant concentrations on the top and the bottom of the primary mush, we also consider a BC setup with fixed concentration gradients at the bottom. We present analytical solutions for the steady non-convecting state, building on the results from [**10**], which consider the Lewis numbers and the segregation coefficients for both solutes equal.

2. Problem formulation

We consider directional solidification of ternary mixture, which develops two distinct mushy zones as in [**3**]. To understand the most complex part of the system we will adopt the reduction from [**4**] and [**8**] to consider only a single primary mushy layer. The mushy layer is bounded by two planar interfaces, which move in time at a constant speed V^* and having a distance H^* apart. We will restrict our inquiry in a steady one dimensional solution without convection, denoted as a base state of the system of equations described in [**4**].

Equations governing the base state in coordinate system moving in z^* direction with speed V^*, where which T^*, C_1^*, C_2^* and ϕ denotes temperature, concentrations of two solutes and solid fraction respectively.

$$-V^*\bar{c}^*(\phi)\frac{\mathrm{d}T^*}{\mathrm{d}z^*} = \frac{\mathrm{d}}{\mathrm{d}z^*}\left[\bar{k}^*(\phi)\frac{\mathrm{d}T^*}{\mathrm{d}z^*}\right] - V^*L^*\frac{\mathrm{d}\phi}{\mathrm{d}z^*}, \tag{1a}$$

$$-V^*(1-\phi)\frac{\mathrm{d}C_j^*}{\mathrm{d}z^*} = \frac{\mathrm{d}}{\mathrm{d}z^*}\left[D_j^*(1-\phi)\frac{\mathrm{d}C_j^*}{\mathrm{d}z^*}\right] - V^*(1-k_j)C_j^*\frac{\mathrm{d}\phi}{\mathrm{d}z}, \text{ for } j=1,2, \tag{1b}$$

$$T^* = m_1^*C_1^* + m_2^*C_2^*, \tag{1c}$$

where $\bar{c}^*(\phi) = c_s^*\phi + (1-\phi)c_l^*$ is the effective specific heat of the mushy layer with c_s^* and c_l^* being the constant specific heat in the solid and liquid phases; $\bar{k}^*(\phi) = k_s^*\phi + (1-\phi)k_l^*$ is the effective thermal conductivity with k_l^* and k_s^* being thermal conductivity of liquid and solid phase respectively; L^* is the latent

heat; D_j^* is constant solutal diffusivity in the liquid for species j (diffusion of solute in the solid is neglected); k_j are segregation coefficients and m_j^* are liquidus slopes.

The system (1) consists of conservation of energy (1a), conservation of solutes (1b) and liquidus constraint (1c) maintaining thermodynamical equilibrium throughout the mushy layer.

We consider two types of BC, the first one is the same as used in [**4**] and [**10**], where concentrations of solutes are fixed both at the top and the bottom of the mushy layer. The second one has fixed concentrations of solutes at the bottom, and fixed solutal flux at the top. We denote the cases of fixed concentrations and fixed fluxes CC and FC respectively.

$$\begin{aligned}
&\text{CC}: \quad C_j^* = C_{jtop}^*, \phi = \phi_0 \text{ at } z^* = H^*; \quad C_j = C_{jbot}^* \text{ at } z^* = 0,\\
&\text{FC}: \quad C_j^* = C_{jtop}^*, \phi = \phi_0 \text{ at } z^* = H^*; \quad \frac{\mathrm{d}C_j^*}{\mathrm{d}z^*} = G_{jbot}^* \text{ at } z^* = 0,
\end{aligned}$$

for $j = 1, 2$, where C_{jbot}^* and C_{jtop}^* are prescribed values of solute concentrations and G_{jbot}^* are values at which solutal fluxes fixed.

It is useful to introduce the quantities T_{bot}^*, T_{top}^* and G_{bot}^*, which by liquidus constraint satisfy

$$T_{bot}^* = T_M^* + m_1^* C_{1bot}^* + m_2^* C_{2bot}^*, \tag{2a}$$

$$T_{top}^* = T_M^* + m_1^* C_{1top}^* + m_2^* C_{2top}^*, \tag{2b}$$

$$G_{bot}^* = m_1^* G_{1bot}^* + m_2^* G_{2bot}^*, \tag{2c}$$

where T_M^* is melting temperature of pure solvent.

2.1. Non-dimensionalisation

For all BC types (CC, FC) we obtain the same system of dimensionless governing equations. Difference is within definitions of dimensionless quantities. We will employ non-dimensionalisation as in [**4**] in which, lengths will be scaled by factor H^* - height of mushy layer, time by H^{*2}/κ_l^*, where $\kappa_l^* = k_l^*/c_l^*$ is thermal diffusivity and velocity by κ_l^*/H^*. We introduce dimensionless parameters valid for all BC types:

$$V = V^* H^*/\kappa_l^*, \quad Le_j = \kappa_l^*/D_j^*. \tag{3}$$

Dimensionless quantities for both BC types are summarized in table 1. Dimensionless version of BC is

$$\begin{aligned}
&\text{CC}: \quad C_j(0) = C_{jbot}, C_j(1) = C_{jbot} + 1, \phi(1) = \phi_0;\\
&\text{FC}: \quad \frac{\mathrm{d}C_j}{\mathrm{d}z}(0) = 1, C_j(1) = C_{jtop}, \phi(1) = \phi_0.
\end{aligned}$$

3. Reduced parametric cases: Analytical solutions

In [**10**] we presented a number of parametric reductions allowing analytical solution of system (1). Here we will consider the case in which both statically–stably and

Table 1. Definitions of dimensionless quantities.

Dimensionless quantity	Type CC	Type FC
T	$\left(T^{*}-T_{M}^{*}\right)/\left(T_{top}^{*}-T_{bot}^{*}\right)$	$\left(T^{*}-T_{M}^{*}\right)/\left(G_{bot}^{*}H^{*}\right)$
C_j	$C_{j}^{*}/\left(C_{jtop}^{*}-C_{jbot}^{*}\right)$	$C_{j}^{*}/\left(G_{jbot}^{*}H^{*}\right)$
S	$L^{*}/\left(c_{l}^{*}\left(T_{top}^{*}-T_{bot}^{*}\right)\right)$	$L^{*}/\left(c_{l}^{*}G_{bot}^{*}H^{*}\right)$
m_j	$m_{j}^{*}\left(C_{jtop}^{*}-C_{jbot}^{*}\right)/\left(T_{top}^{*}-T_{bot}^{*}\right)$	$\left(m_{j}^{*}G_{jbot}^{*}\right)/\left(G_{bot}^{*}\right)$
C_{jbot}	$C_{jbot}^{*}/\left(C_{jtop}^{*}-C_{jbot}^{*}\right)$	
C_{jtop}	$C_{jtop}^{*}/\left(C_{jtop}^{*}-C_{jbot}^{*}\right)$	$C_{jtop}^{*}/\left(G_{jbot}^{*}H^{*}\right)$
T_{bot}	$\left(T_{bot}^{*}-T_{M}^{*}\right)/\left(T_{top}^{*}-T_{bot}^{*}\right)$	
T_{top}		$\left(T_{top}^{*}-T_{M}^{*}\right)/\left(G_{bot}^{*}H^{*}\right)$

statically unstably stratified concentration profiles are present, allowing further study of doubly–diffusing convection in statically–stable region presented in [**4**]. We will assume the same speed of solute rejection $k_1 = k_2 \equiv k$, the same Lewis number $Le_1 = Le_2 = Le$ for both solutes and zero Stefan number $S = 0$. We will also make assumption of the same material properties of the liquid and solid phases, namely thermal conductivity $k_s^* = k_l^*$ and specific heat $c_s^* = c_l^*$.The most important features of this reduction are finite speed of macroscopic solidification ($V \neq 0$) and presence of solute rejection effects ($k \neq 1$).

Under mentioned reductions the dimensionless base state equations (1) take the form:

$$\begin{aligned} -V\frac{\mathrm{d}T}{\mathrm{d}z} &= \frac{\mathrm{d}^2T}{\mathrm{d}z^2}, \\ -V\left(1-\phi\right)\frac{\mathrm{d}C_j}{\mathrm{d}z} &= \frac{1}{Le}\frac{\mathrm{d}}{\mathrm{d}z}\left[\left(1-\phi\right)\frac{\mathrm{d}C_j}{\mathrm{d}z}\right] - V\left(1-k\right)C_j\frac{\mathrm{d}\phi}{\mathrm{d}z}, \text{ for } j=1,2, \\ T &= m_1C_1 + m_2C_2. \end{aligned}$$

The solution of T depends on the choice of BC type as follows:

$$T\left(z\right) = \begin{cases} \left(\delta - \mathrm{e}^{-Vz}\right)/\left(1-\mathrm{e}^{-V}\right) & \text{CC} \\ \left(\delta - \mathrm{e}^{-Vz}\right)/V & \text{FC}, \end{cases}$$

where the parameter $\delta = \left(\mathrm{e}^{-V}T\left(0\right) - T\left(1\right)\right)/\left(T\left(1\right) - T\left(0\right)\right)$, which depending on the type of BC is equal to:

$$\delta = \begin{cases} 1 + T_{bot}\left(1-\mathrm{e}^{-V}\right) & \text{CC} \\ \mathrm{e}^{-V} + VT_{top} & \text{FC}. \end{cases}$$

Physically admissible range of values for δ is $(-\infty;1)$ and $\left(-\infty;\mathrm{e}^{-V}\right)$ for CC and FC type of BC respectively. The solid fraction satisfies

$$\frac{\mathrm{d}}{\mathrm{d}z}\ln\left(1-\phi\right)=-\frac{1}{1-\phi}\frac{\mathrm{d}\phi}{\mathrm{d}z}=\frac{V\mathrm{e}^{-Vz}}{-Le(1-k)\delta/\left(Le-1\right)+\eta\mathrm{e}^{-Vz}}, \tag{5}$$

where the parameter $\eta=\frac{(1-k)-1/Le}{1-1/Le}$ can take both signs. Note that, as $Le\to\infty$, then $\eta\to 1-k$, which is positive.

The concentration profiles satisfy

$$\frac{\mathrm{d}^2C_j}{\mathrm{d}z^2}+\left[\frac{\mathrm{d}}{\mathrm{d}z}\ln\left(1-\phi\right)+LeV\right]\frac{\mathrm{d}C_j}{\mathrm{d}z}+\left[VLe\left(1-k\right)\frac{\mathrm{d}}{\mathrm{d}z}\ln\left(1-\phi\right)\right]C_j=0. \tag{6}$$

This equation can be transformed to a hypergeometric equation

$$\frac{\mathrm{d}^2C_j}{\mathrm{d}\xi^2}\xi\left(1-\xi\right)+\frac{\mathrm{d}C_j}{\mathrm{d}\xi}\left[c-\xi\left(1+a+b\right)\right]-abC_j=0, \tag{7}$$

where $a=-1$, $b=-Le\left(1-k\right)/\eta$, $c=-1/\eta$ and

$$\xi\left(z\right)=1-\frac{\left(Le-1\right)\eta}{Le\left(1-k\right)\delta}\mathrm{e}^{-Vz}. \tag{8}$$

Note that (7) is a linear second-order differential equation with three regular singular points[1] $\xi=0$, 1 and ∞ as defined in [**1**]. We consider the case when none of the numbers c, $c-a-b$, $a-b$ is equal to the integer. Solution of equations (5) and (6), then have the form:

$$\phi\left(z\right)=1-\left(1-\phi_0\right)\left(\xi\left(1\right)/\xi\left(z\right)\right)^{\frac{1}{\eta}}, \tag{9a}$$

$$C_j\left(z\right)=\alpha_j w_{1(x)}\left(z\right)+\beta_j w_{2(x)}\left(z\right)\ \text{ for } j=1,2, \tag{9b}$$

where $w_{i(x)}$ refers to the i-th independent solution around $\xi=x$. Their form is determined by regime of ξ, defined by the values of V, Le, k and T_{bot} (or T_{top}).

For $\xi<0$ the expansion around the regular singular point $\xi=0$ can be used[2]

$$w_{1(0)}=\ {}_2F_1\left(a,b;c;\xi\right), \tag{10a}$$

$$w_{2(0)}=\xi^{1-c}{}_2F_1\left(a-c+1,b-c+1;2-c;\xi\right). \tag{10b}$$

When $\xi\sim 1$ for all z, then the pair of independent solutions is defined as

$$w_{1(1)}=\ {}_2F_1\left(a,b;a+b+1-c;1-\xi\right), \tag{11a}$$

$$w_{2(1)}=\left(1-\xi\right)^{c-a-b}{}_2F_1\left(c-b,c-a;c-a-b+1;1-\xi\right). \tag{11b}$$

---

[1]Consider equation of the form $P\left(x\right)y''+Q\left(x\right)y'+R\left(x\right)y=0$ and suppose that P, Q and R are polynomials, and $P\left(x_0\right)=0$. Then x_0 is a regular singular point if $\lim_{x\to x_0}\left(x-x_0\right)\frac{Q(x)}{P(x)}$ and $\lim_{x\to x_0}\left(x-x_0\right)^2\frac{R(x)}{P(x)}$ are both finite.

[2]If $\xi<-1$, the hypergeometric series is not convergent and its analytical continuation along the negative real axis can be used.

In the case of large $\xi(z)$, we have

$$w_{1(\infty)} = \xi^{-a}\ {}_2F_1\left(a, a-c+1; a-b+1; \xi^{-1}\right), \tag{12a}$$

$$w_{2(\infty)} = \xi^{-b}{}_2F_1\left(b, b-c+1; b-a+1; \xi^{-1}\right). \tag{12b}$$

The main building block of independent solutions of (7) is the hypergeometric series

$${}_2F_1\left(a, b; c; \xi\right) = \sum_{n=0}^{\infty} \frac{(a)_n (b)_n}{(c)_n} \frac{\xi^n}{n!}, \tag{13}$$

as defined in [**1**, p. 563], where $(a)_n = a\,(a+1)\,(a+2)\cdots(a+n-1)$ is the rising factorial. The rising factorial can be expressed as a ratio of Gamma functions $(a)_n = \Gamma(a+n)/\Gamma(a)$. The hypergeometric series is convergent for $|\xi| < 1$.

Constants α_j, β_j (for $j = 1, 2$) can be expressed as solutions to the system of algebraic equations depending on type of BC. Note that the choice of BC influences the general solution of base state only through the parameter group δ. Applying BC of type CC, we obtain

$$\alpha_j = \frac{\frac{w_{2(x)}(1)}{w_{2(x)}(0)} C_{jbot} - (C_{jbot}+1)}{\frac{w_{2(x)}(1)}{w_{2(x)}(0)} w_{1(x)}(0) - w_{1(x)}(1)},\ \beta_j = \frac{(C_{jbot}+1) - \frac{w_{1(x)}(1)}{w_{1(x)}(0)} C_{jbot}}{w_{2(x)}(1) - \frac{w_{1(x)}(1)}{w_{1(x)}(0)} w_{2(x)}(0)}, \tag{14}$$

for $j = 1, 2$. In FC case, we obtain

$$\alpha_j = \frac{\frac{w_{2(x)}(1)}{w'_{2(x)}(0)} - C_{jtop}}{\frac{w_{2(x)}(1)}{w'_{2(x)}(0)} - w_{1(x)}(1)},\ \beta_j = \frac{C_{jtop} - \frac{w_{1(x)}(1)}{w'_{1(x)}(0)}}{w_{2(x)}(1) - \frac{w_{1(x)}(1)}{w'_{1(x)}(0)} w'_{2(x)}(0)}, \tag{15}$$

for $j = 1, 2$. The derivatives of $w_{2(x)}$ can be obtained using the formula from [**1**, p. 557]:

$$\frac{\mathrm{d}}{\mathrm{d}\xi}\xi^{c-1}{}_2F_1\left(a, b; c; \xi\right) = (c-1)\,\xi^{c-2}{}_2F_1\left(a, b; c-1; \xi\right). \tag{16}$$

[**10**] lists the solutions when the segregation coefficient k attains some special values. Namely if $k = 0$ the solution for $C_j(z)$ takes the form of exponential function; if $k = (Le-1)/Le$ the solution for $C_j(z)$ takes the form of extended confluent hypergeometric function and when $k = 1$ the solid fraction is an increasing function of z (physically non-admissible setup).

3.1. Limiting case: $Le \to \infty$

Typically, the Lewis number is much larger than unity. For example in binary case, the helium–water mixture has $Le \sim 23$, while the ethanol–water mixture has $Le \sim 170$.[3]

Expanding (8) in the limit of large Le, we obtain:

$$\xi(z) = \left(1 - \frac{\mathrm{e}^{-Vz}}{\delta}\right) + \frac{\mathrm{e}^{-Vz}}{\delta\,(1-k)}\frac{1}{Le}, \tag{17}$$

[3]The values of mass diffusivity and thermal diffusivity are from [**6**], [**5**], respectively.

where the second term cannot be omitted because the first term may became $O(1/Le)$ or smaller due to a combination of relatively small values of V, $1-k$ and $T_{bot} \sim -1$ in CC case or $T_{top} \sim 0$ in FC case.

It is sufficient to consider only two cases $\xi < 0$ and $\xi > 1$, because the case $0 < \xi < 1$ corresponds to $T_{bot} > -1$. The values of V and T_{bot} (or T_{top}) define the regime of ξ and so determine the pair of independent solutions which should be used to construct solution. The summary is in table 2. Note that regime of $\xi \sim 1$

Table 2. Regimes of ξ with different pairs of independent solutions and parameter constraints in limit of large Le.

Regime of ξ	Independent solutions	Type CC	Type FC
$\xi < 0$	$w_{1(0)}, w_{2(0)}$	$1 < -T_{bot} < 1/\left(1-\mathrm{e}^{-V}\right)$	$\mathrm{e}^{-V} < -T_{top} < \mathrm{e}^{-V}/V$
$\xi > 1$	$w_{1(\infty)}, w_{2(\infty)}$	$1/\left(1-\mathrm{e}^{-V}\right) < -T_{bot}$	$\mathrm{e}^{-V}/V < -T_{top}$

is not present within limit of large Le, only apearing in the limit $C_{1bot} \to -\infty$.

At first we will consider regime $\xi < 0$, the appropriate independent solutions are

$$w_{1(0)} = \left(1 - \frac{\mathrm{e}^{-Vz}}{\delta}\right)\left[1 - Le\,(1-k)\right], \tag{18a}$$

$$w_{2(0)} = \xi^{k/(1-k)}\,(1-\xi)^{Le}\,\frac{2-k}{(1+Le\,(1-k))^2}\left[1 + O\,(1/Le)\right]. \tag{18b}$$

The expression (18a) can be obtained from (10a) using the relation

$$ {}_2F_1\,(-m, b; c; \xi) = \sum_{n=0}^{m} \frac{(-m)_n\,(b)_n}{(c)_n}\,\frac{\xi^n}{n!}, \tag{19}$$

from [**1**, p. 561], where m is positive integer. Asymptotic expansion for (18b) can be derived using the Euler linear transformation formula from [**1**, p. 559]:

$$ {}_2F_1\,(a, b; c; \xi) = (1-\xi)^{(c-a-b)}\,{}_2F_1\,(c-a, c-b; c; \xi) \tag{20}$$

and then using the fact from [**1**, p. 565], that a real-valued hypergeometric function for fixed a, c, ξ, $(c \neq 0, -1, -2, \ldots)$, $0 < |\xi| < 1$ and large $|b|$ satisfies

$$ {}_2F_1\,(a, b; c; \xi) = \left[\frac{\Gamma\,(c)}{\Gamma\,(c-a)}\,(-b\xi)^{-a} + \frac{\Gamma\,(c)}{\Gamma\,(a)}\mathrm{e}^{b\xi}\,(b\xi)^{a-c}\right]\left[1 + O\left(|b\xi|^{-1}\right)\right]. \tag{21}$$

Now we consider $\xi > 1$, the pair of independent solutions is

$$w_{1(\infty)} = \xi - 1/Le/\,(1-k)\,, \tag{22a}$$

$$w_{2(\infty)} = \xi^{\frac{k-2}{1-k}}\,(\xi-1)^{Le} + O(1/Le). \tag{22b}$$

The form (22a) can be obtained from (12a) using (19). The asymptotic expansion of second independent solution (22b) is obtained, when transform (20) is applied to

(12b), and then is used the asymptotic expansion for large Le defined by relation from [**1**, p. 565]

$$ {}_2F_1\left(a,b;c;\xi\right)=\sum_{n=0}^{m}\frac{\left(a\right)_n\left(b\right)_n}{\left(c\right)_n}\frac{\xi^n}{n!}+O(|c|^{-m-1}), \tag{23}$$

where a, b, ξ are fixed and $|c|$ large.

In the following sections we will use the pairs (18a), (18b) and (22a), (22b) to construct asymptotic expansions for different BC types.

3.1.1. CC type of BC. The leading-order asymptotic expansion of (9) for BC (14) in the regime $\xi<0$, or equivalently $1<-T_{bot}<1/\left(1-\mathrm{e}^{-V}\right)$, takes the form

$$\phi\left(z\right)=1-\left(1-\phi_0\right)\left(\xi(z)/\xi(1)\right)^{-\frac{1}{1-k}}+O(1/Le), \tag{24a}$$

$$C_j\left(z\right)=\frac{C_{jbot}+1}{T_{bot}+1}T\left(z\right)+\frac{C_{jbot}-T_{bot}}{T_{bot}+1}\vartheta\left(z\right)+O(1/Le), \tag{24b}$$

for $j=1,2$, where

$$\vartheta\left(z\right)=\left(\xi\left(z\right)/\xi\left(0\right)\right)^{k/(1-k)}\mathrm{e}^{-VLez}.$$

The function $\vartheta\left(z\right)$ is positive and monotonically decreasing for $z\in[0;1]$, and evaluates to $\vartheta\left(0\right)=1$ and $\vartheta\left(1\right)=O(\mathrm{e}^{-Le})$. Thus $\vartheta\left(1\right)$ is exponentially small as $Le\to\infty$. Note that the importance of the term $\left(\xi\left(z\right)/\xi\left(0\right)\right)^{k/(1-k)}$ grows when the term $\left(1-\mathrm{e}^{-Vz}/\delta\right)$ in (17) is not $O\left(1\right)$, otherwise $\vartheta\left(z\right)\sim\mathrm{e}^{-VLez}$. The formulae analogous to (24b) in the regime $\xi>1$, or equivalently $-T_{bot}>1/\left(1-\mathrm{e}^{-V}\right)$, are

$$C_j\left(z\right)=C_{1bot}\frac{\xi\left(z\right)}{\xi\left(1\right)}+\vartheta\left(z\right)\left(\frac{\xi\left(z\right)}{\xi\left(0\right)}\right)^{-\frac{2}{1-k}}\left[C_{jbot}-\left(C_{jbot}+1\right)\frac{\xi\left(z\right)}{\xi\left(1\right)}\right]+O(1/Le) \tag{25}$$

for $j=1,2$. The formulae (24b) and (25) are asymptotically equivalent if

$$\left(1-\mathrm{e}^{-V}\right)\left(1-k\right)=O(1)\text{ as }Le\to\infty.$$

The second term of (24b) vanishes as $|C_{1bot}-C_{2bot}|$ is small, in that case the first term dictates concentration profiles to be proportional to T and hence monotonic. Therefore non-monotonicity of concentration profile can occur only when difference $|C_{1bot}-C_{2bot}|$ exceeds some threshold, this will be addressed in §3.4.

In figure 1 we compare the analytical solution with the leading-order solution (24), showing solid fraction, composition and temperature profiles on insets (a), (b), (c) respectively. Figure 1(d) shows solution in C_2-versus-C_1 plane. The good agreement is seen even for relatively low values of Le. Important property of (24) is that when $k=0$ it reduces to exact solution [**10**].

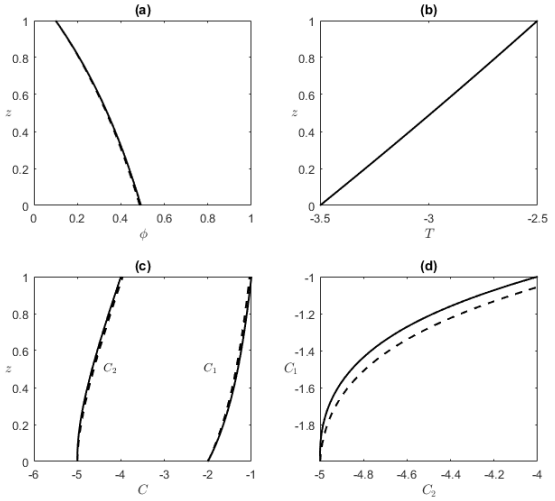

Figure 1. Comparison of the explicit solution calculated from (9) and (14) (solid) and the leading-order asymptotic solution (24) (dashed) with CC type of BC applied in the regime of $\xi < 0$. Parameter values used here are $m_1 = m_2 = 0.5$, $Le_1 = Le_2 = 25$, $k_1 = k_2 = 0.3$, $k_s/k_l = 1$, $c_s/c_l = 1$, $S = 0$, $V = 0.1$. The BC are $C_{1bot} = -2$, $C_{2bot} = -5$ and $\phi_0 = 0.1$.

3.1.2. FC type of BC. The leading-order asymptotic expansion of (9) for BC (15) valid for $\xi < 0$, or equivalently $\mathrm{e}^{-V} < -T_{top} < \mathrm{e}^{-V}/V$, has the form

$$\phi(z) = 1 - (1-\phi_0)\left(\frac{\xi(z)}{\xi(1)}\right)^{-\frac{1}{1-k}} + O(1/Le), \tag{26a}$$

$$C_j(z) = \frac{C_{1top}}{T_{top}} T(z) + \frac{C_{jtop} - T_{top}}{T_{top}} \frac{1}{V\left(Le + \frac{k}{1-k}\frac{1}{1-\delta}\right)} \vartheta(z) + O(Le^3) \tag{26b}$$

for $j = 1, 2$. For $\xi > 1$ or equivalently $-T_{top} > \mathrm{e}^{-V}/V$, the analogue of (26b) is

$$C_j(z) = \frac{\left[\frac{\tilde{\vartheta}(1)}{V} - C_{jtop} q\right] \xi(z) + \left[C_{jtop}(1 - \xi(0)) - \frac{\xi(1)}{V}\right] \tilde{\vartheta}(z)}{\tilde{\vartheta}(1)(1-\xi(0)) - \xi(1) q} + O(Le^3)$$

for $j = 1, 2$, where $q = \left(\frac{k-2}{1-k}(1-\xi(0)) - Le\xi(0)\right)/\xi(0)$ and $\tilde{\vartheta}(z) = \vartheta(z)\left(\xi(z)/\xi(0)\right)^{-\frac{2}{1-k}}$.

3.2. Limiting case: $C_{1bot} \to -\infty$

In this section, we consider the limit $C_{1bot} \to -\infty$ with $C_{2bot} = O(1)$. By swapping the solutal indices the results for the limit $C_{2bot} \to -\infty$ with $C_{1bot} = O(1)$ can be obtained.

In [**8**], the limit of small solidification speeds $V \to 0$ was considered, subject to $S = \bar{S}/V^2$ and $C_{jbot} = C_{jbot}/V^2$ with $\bar{S}$ and C_{jbot} both $O(1)$. It has been shown that in case when $Le_1 = Le_2 = Le$, single–solute–diffusive regime, the ratio of C_{1bot}/C_{2bot} plays a crucial role in determining the linear stability scenario which the system exhibits. In this limit, for relatively large Le the base state concentration profiles are qualitatively similar to our findings in this section. The main difference is in generally smaller parametric space exhibiting non-monotonic behaviour of concentration profiles.

For large values of C_{1bot}, the scaled coordinate is $\xi = 1 + O(1/C_{1bot})$, therefore we will employ two independent solutions (11a) and (11b) around regular singular point $\xi = 1$ of (7). The asymptotic expansions of (11a) and (11b) in the limit of large $|C_{1bot}|$ correct to $O(1/C_{1bot}^2)$ take the form

$$w_{1(1)}(z) = 1 - \frac{\mathrm{e}^{-Vz}}{\delta} = 1 - \frac{\mathrm{e}^{-Vz}}{m_1 C_{1bot}(1-\mathrm{e}^{-V})} + O(C_{1bot}^{-2}), \tag{27a}$$

$$w_{2(1)}(z) = \mathrm{e}^{-VLez}\left[1 - \frac{Le-1}{Le+1}\frac{k}{1-k}\frac{\mathrm{e}^{-Vz}}{1-\mathrm{e}^{-V}}\frac{1}{m_1 C_{1bot}} + O(C_{1bot}^{-2})\right]. \tag{27b}$$

where formulae (27a) and (27b) were obtained using (19) and series of hypergeometric function around zero ${}_2F_1(a,b,c,z) = 1 + abz/c + O(z^2)$ respectively. For $\phi(z)$, $C_1(z)$ and $C_2(z)$ we have

$$\phi(z) = \phi_0 + \frac{1}{m_1 C_{1bot}}\frac{(1-\phi_0)(Le-1)}{(1-k)Le}\frac{\mathrm{e}^{-V} - \mathrm{e}^{-Vz}}{1-\mathrm{e}^{-V}} + O(1/C_{1bot}^2), \tag{28a}$$

$$C_1(z) = C_{1bot} - \frac{m_2}{m_1}\frac{1-\mathrm{e}^{-LeVz}}{1-\mathrm{e}^{-LeV}} + \frac{1}{m_1}\frac{1-\mathrm{e}^{-Vz}}{1-\mathrm{e}^{-V}} + O(1/C_{1bot}), \tag{28b}$$

$$C_2(z) = C_{2bot} + \frac{1-\mathrm{e}^{-LeVz}}{1-\mathrm{e}^{-LeV}} + O(1/C_{1bot}). \tag{28c}$$

It is instructive to examine the behaviour of (28) when product $LeV = O(1)$, while $V \to 0$ and $Le \to \infty$. The leading-order reduces to

$$\begin{aligned}
\phi(z) &\sim \phi_0 + \frac{1}{m_1 C_{1bot}}\frac{(1-\phi_0)}{(1-k)}(z-1),\\
C_1(z) &\sim C_{1bot} - \frac{m_2}{m_1}\left(1-\mathrm{e}^{-LeVz}\right) + \frac{z}{m_1},\\
C_2(z) &\sim C_{2bot} + 1 - \mathrm{e}^{-LeVz}.
\end{aligned}$$

It can be observed that the solid fraction is constant at leading-order with the linear correction term at $O(1/C_{1bot})$. Concentration profile of solute j with smaller $|C_{jbot}|$ exhibits non-monotonic behaviour.

3.3. Monotonicity of solid fraction

The base-state solid fraction does not possess any local extrema. The physically admissible solution with $\mathrm{d}\phi/\mathrm{d}z < 0$ exists provided

$$\delta < \frac{(Le-1)\,\eta}{Le\,(1-k)\,\mathrm{e}^{Vz}}.$$

With CC type of BC applied, the monotonicity of the solid fraction is established when

$$m_1 C_{1bot} + m_2 C_{2bot} < -\frac{1+\max\{Le\,(1-k)\,,1\}\left(\mathrm{e}^{V}-1\right)}{Le\,(1-k)\,(\mathrm{e}^{V}-1)}. \tag{30}$$

Note that, the first two terms of expansion as $V \to 0$ reduce expression (30) to

$$m_1 C_{1bot} + m_2 C_{2bot} < \begin{cases} -1 - \frac{1}{VLe(1-k)} & Le\,(1-k) > 1 \\ -\frac{1}{VLe(1-k)} & Le\,(1-k) < 1. \end{cases}$$

3.4. Monotonicity of concentration profiles

The base state is statically stable stratified if density of fluid is decreasing function of z, therefore non-monotonic behaviour of concentration profile can induce statically unstable situation.

In CC case non-monotonic behaviour depends on the values C_{1bot} and C_{2bot}. Following calculations present extension of [**10**] allowing us to evaluate effect of non–zero segregation coefficient k. In the limit $Le \to \infty$, using asymptotic expansion formula (24) for base state solution of C_1 presented in §3.1.1 we have computed the boundaries of an area within which, both concentration profiles remains monotone. Boundaries are determined using equations $\left.\frac{\mathrm{d}C_j}{\mathrm{d}z}\right|_{z=0} = 0$ for $j = 1, 2$. This approach gives us two implicit functions of C_{1bot}, C_{2bot} defined by

$$C_{1bot} = \frac{T_{bot}\Omega - 1}{1+\Omega}, \quad C_{2bot} = \frac{T_{bot}\Omega - 1}{1+\Omega}, \tag{31}$$

where $\Omega \equiv \left(1-\mathrm{e}^{-V}\right)\left[\frac{k(Le-1/(1-k))}{Le(1-k)T_{bot}(1-\mathrm{e}^{-V})+1} - Le\right]$. By closer inspection of (31) and by noting that $T_{bot} = m_1 C_{1bot} + m_2 C_{2bot}$, it can be seen that it defines quadratic expression in variables C_{1bot} and C_{2bot}.

In figure 2, three qualitatively different scenarios are depicted: (a) profile of C_2 is non-monotonic; (b) – both concentration profiles are monotonic and (c) profile of C_1 is non-monotonic.

3.4.1. Limiting case $Le \to \infty$, $V \to 0$. We consider a limit of small pulling speeds V and large Lewis numbers defined by $Le = \bar{Le}/V$ with $\bar{Le} = O(1)$ as $V \to 0$. The assumption $1 - k = O(1)$ remains intact. Under these assumptions oblique asymptote to implicit curves (31) as $C_{2bot} \to -\infty$ we have

$$C_{1bot} = \frac{1 + m_2 \bar{Le} C_{2bot}}{m_2 \bar{Le} - 1} + \frac{k}{(1-k)\left(\bar{Le}-1\right)\left(m_2 \bar{Le}-1\right)},$$

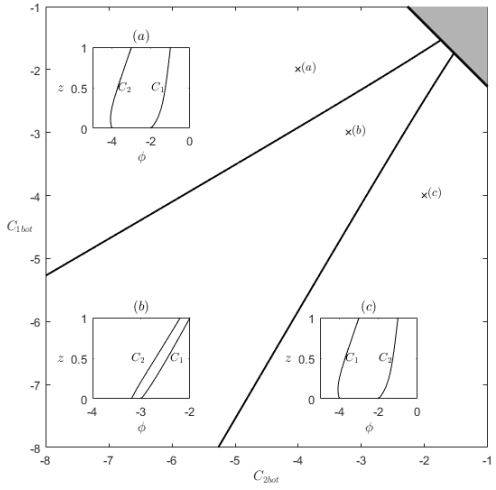

Figure 2. This plot shows classification of qualitatively different compositional profiles in dependence on concentration BC in the C_{2bot}-versus-C_{1bot} plane. Lines along which the profiles change their monotonic behaviour were determined using asymptotic result (31). In the grey region at the top right corner the model is not physically meaningful. Three qualitatively different scenarios are depicted with BC as shown. Parameters used were $Le = 50$, $k = 0.7$, $V = 0.1$, $\phi_0 = 0.1$ and $m_1 = 0.5$.

where the first term is correspond to results from [**10**], where $k = 0$ and the second term represents a correction when $k > 0$. Note that, as $k \to 1$, the region of monotonicity increasingly changes it's size. The sign of $m_2\bar{L}e - 1$ defines, whether it increases or decreases. The effect of non-zero segregation coefficients on the monotonicity of concentration profiles can be observed in figure 3. When Le is relatively low, sensitivity to change in segregation coefficient is significant. As $Le \to \infty$ effects of non-zero segregation coefficients diminish.

3.4.2. Parametric dependence of the region of static stability. When density of the liquid is depends on density of solutes, the position of local extreme of the concentration profile corresponds to a height at which the stratum of liquid with statically unexpected density is located. In the limit $Le \to \infty$, the position can be computed using (24) and (26) for CC and FC types of BC respectively

$$z_{\mathrm{CC}} = \frac{1}{V\,(Le-1)} \ln\left[\frac{C_{jbot} - T_{bot}}{C_{jbot}+1} Le\left(1-\mathrm{e}^{-V}\right)\right], \tag{32}$$

$$z_{\mathrm{FC}} = \frac{1}{V\,(Le-1)} \ln\left[\frac{C_{jtop} - T_{top}}{C_{jtop}} \frac{Le\,(1-\delta)}{Le\,(1-\delta)+k/1-k}\right]. \tag{33}$$

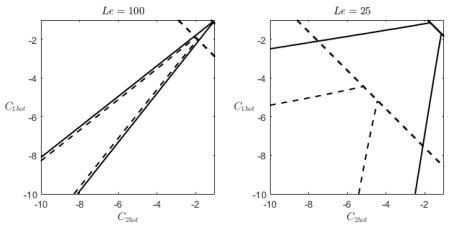

Figure 3. Plot depicting a shape of statically stable region in the C_{2bot}-versus-C_{1bot} plane for different values of Le and k. The solid line corresponds to $k = 0.1$ and dashed line corresponds to $k = 0.9$. Other parameters are fixed at $V = 0.1$, $m_1 = 0.5$, $\phi_0 = 0.1$.

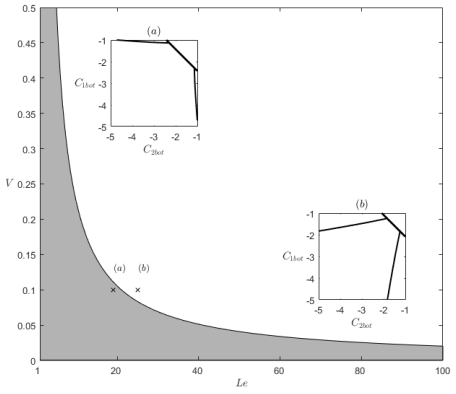

Figure 4. Plot of (35) in the plane Le-versus-V. In the grey region both concentration profiles are always monotonic, while in the white region there always exist BC set-up in which one of the concentration profiles is non–monotonic. Inset (a) shows case when set of BC allowing non–monotonic concentration profile is bounded. In inset (b) set of BC allowing non–monotonic behaviour covers alse limiting cases $C_{1bot} \to \infty$ while $C_{2bot} = O(1)$ and $C_{2bot} \to \infty$ while $C_{1bot} = O(1)$. The results are shown for $m_1 = m_2 = 0.5$.

When $C_{1bot} \to -\infty$ is considered the local extreme of the concentration profile computed from (28):

$$z_{\mathrm{CC}} = \frac{1}{V\,(Le-1)} \ln\left[m_2 Le \frac{\left(1-\mathrm{e}^{-V}\right)}{\left(1-\mathrm{e}^{-LeV}\right)} \right], \tag{34}$$

is the same as the one from limit $C_{1bot} \to -\infty$ of expression (32). This representation defines parametric combination of Le, V and m_2 for which both concentration

profiles are monotonic independent of the choice of BC

$$m_2 Le \left(1 - \mathrm{e}^{-V}\right) \lesssim 1, \tag{35}$$

which holds for all values of k satisfying $1 - k = O(1)$. Figure 4 shows grey and white region in the Le-versus-V plane divided by the line $m_2 Le \left(1 - \mathrm{e}^{-V}\right) = 1$. Insets in this figure show representative shapes of BC sets allowing non-monotonic concentration profiles. In the grey region the case (a) shows a bounded set of BC which allows non-monotonic concentration profile. Therefore when $C_{1bot} \to -\infty$ monotonic behaviour of concentration profiles is expected.

In the white region the case (b) shows that BC are divided by a linear relation, as was observed by numerical resuts in [**4**]. Therefore when $C_{1bot} \to -\infty$ non-monotonic behaviour of attributable concentration profile is expected.

4. Conclusion

We analysed the model of solidification of primary mushy layer described in [**4**], while considering two different types of BC. The CC type was used in [**4**] and FC type introduced to expand range of possible scenarios.

We considered finite macroscopic speed of solidification V. Explicit solution using hypergeometric function was obtained. In §3.1 we construct the asymptotic expansion in the limit of large Lewis number Le. Presented leading-order asymptotic expansions show very good accuracy even for a low values of Le.

In §3.2 we considered the limit of large $|C_{1bot}|$ causing asymmetry in BC resulting in non-monotonic C_1 profile. This result can be compared with [**8**] where limit of jointly large $|C_{1bot}|$ and $|C_{2bot}|$ is considered. Notable feature of obtained expansions is that they preserve non-monotonic behaviour of concentration profiles. Non-monotonic behaviour of concentration profiles may lead to statically unstable stratification of fluid, therefore play important role in onset of convection originating in mushy layer. When appropriate solutal expansion coefficients considered, the results from §3.4 identify the critical lines of static stability. We show that the critical lines are in general non-linear and that in this case approach the oblique asymptote as $Le \to \infty$.

References

1. Abramowitz, M., & Stegun, I. A., *Handbook of mathematical functions: with formulas, graphs, and mathematical tables*, vol. 55. (1964).
2. Anderson, D. M., *A model for diffusion-controlled solidification of ternary alloys in mushy layers*, J Fluid Mech, **483** (2003), 165–197.
3. Anderson, D. M., & Schulze, T. P., *Linear and nonlinear convection in solidifying ternary alloys*, J Fluid Mech, **545** (2005), 213–243.
4. Anderson, D. M., McFadden, G. B., Coriell, S. R., & Murray, B. T., *Convective instabilities during the solidification of an ideal ternary alloy in a mushy layer*, J Fluid Mech, **647** (2010), 309–333.
5. Blumm, J., & Lindemann A., *Characterization of the thermophysical properties of molten polymers and liquids using the flash technique*, High Temp High Press, **35**(36) (2003), 627–632.

6. Cussler, E. L., *Diffusion: mass transfer in fluid systems* , (2009) Cambridge University Press.
7. Davis, S. H., *Theory of solidification*, (2001), Cambridge University Press.
8. Guba, P., & Anderson, D. M., *Diffusive and phase change instabilities in a ternary mushy layer*, J Fluid Mech, **760** (2014), 634–669.
9. ———, *Pattern selection in ternary mushy layers*, J Fluid Mech, **825** (2017), 853–886.
10. Hurban, M., *Static stability of three-component systems*, Master's thesis (2015), Comenius University, Bratislava, Slovakia.
11. Mullins, William W., & R. F. Sekerka, *Stability of a planar interface during solidification of a dilute binary alloy*, J Appl Phys, **35**(2) (1964), 444–451.
12. Schulze, T. P., and M. G. Worster, *Weak convection, liquid inclusions and the formation of chimneys in mushy layers*, J Fluid Mech, **388** (1999), 197–215.
13. Worster, M. G., *Solidification of an alloy from a cooled boundary,* J Fluid Mech, **167** (1986), 481–501.
14. ———, *Instabilities of the liquid and mushy regions during solidification of alloys*, J Fluid Mech, **237** (1992), 649–669.
15. ———, *Convection in mushy layers*, Annu Rev Fluid Mech, **29**(1) (1997), 91–122.

M. Hurban, Faculty of Mathematics, Physics and Informatics, Comenius University, 842 48 Bratislava, Slovak Republic, *e-mail*: `hurban3@uniba.sk`